Physiological aspects on intracardiac blood flow

Arvidsson, Per

2017

Physiological aspects on intracardiac blood flow

Physiological aspects on intracardiac blood flow

Per Arvidsson

LUND
UNIVERSITY

Thesis for the degree of Doctor of Philosophy
Thesis advisors: Prof. Håkan Arheden, Assoc. Prof. Marcus Carlsson
Faculty opponent: Dr. Philip J Kilner

To be presented for public criticism in Föreläsningssal 1, Blocket, Skånes universitetssjukhus i Lund on Saturday, June 3 2017 at 09:00.

DOKUMENTDATABLAD enl SIS 61 41 21

Organization
LUND UNIVERSITY

Author(s)
Per Arvidsson

Document name
DOCTORAL DISSERTATION

Date of issue

Sponsoring organization

Title and subtitle

Physiological aspects on intracardiac blood flow

Abstract

Magnetic resonance imaging enables detailed in vivo study of complex blood flow through 3-D, time-resolved phase contrast imaging (4D flow). 4D flow may reveal previously unknown aspects of the physiology of intracardiac blood flow patterns, and possibly elucidate pathophysiological processes that have yet to manifest themselves outside the heart. The purpose of this thesis is to examine the physiological role of intracardiac flow phenomena using 4D flow, with a specific focus on kinetic energy, vortex ring formation, and hemodynamic forces, in order to better understand the normal function of the heart and to provide a backdrop against which future studies into disease processes can be compared.

Study I revealed significant differences between left and right atrial kinetic energy (KE). Systolic KE was determined to a large extent by atrial volume and the systolic atrioventricular plane velocity, which differ between the left and right sides of the heart. Diastolic KE increased more in the left atrium, likely reflecting suction-initiated filling driven by left ventricular filling. Rotational blood flow KE decay was slower than non-rotational KE decay, indicating a potential enhancement of cardiac function through energy-preserving macroscopic flow structures.

Study II demonstrated a strong spatiotemporal coupling between the vortex ring boundary and the endocardial boundary, suggesting that the normal development of the left ventricle is guided by the shear layer generated by the vortex ring. The coupling may act as a dynamic optimization mechanism to facilitate fluid transport at varying levels of cardiac output. In contrast, failing ventricles show no connection between the vortex ring and endocardium, suggesting that the adaptive coupling of the myocardium to the shear layer is disrupted.

Studies III and IV demonstrated that biventricular hemodynamic forces are similar between healthy hearts regardless of size, and reflect fundamental aspects of flow redirection; this homogenous appearance is significantly altered in heart failure. The findings elucidate a previously unknown 'slingshot' force that appears to result from contraction of the septum and right ventricular free wall. In left ventriclar dyssynchrony, several different force patterns were seen, which potentially indicate different degrees of detrimental effects on myocardial function and hence may predispose to varying treatment response.

Key words: magnetic resonance imaging, 4D flow, physiology, cardiac development, kinetic energy, hemodynamic force, vortex ring formation

Classification system and/or index termes (if any):

Supplementary bibliographical information:

Language
English

ISSN and key title:
1652-8220

ISBN
978-91-7619-484-3

Recipient's notes

Number of pages

Price

Security classification

Physiological aspects on intracardiac blood flow

Per Arvidsson

LUND
UNIVERSITY

Faculty Opponent

Dr. Philip J Kilner
Imperial College
London, Great Britain

Evaluation Committee

Assoc Prof. Trygve Sjöberg
Lund University
Lund, Sweden

Prof. Jan Engvall
Linköping University
Linköping, Sweden

Assoc Prof. Petter Dyverfeldt
Linköping University
Linköping, Sweden

Cover: Visualization of vortex ring formation in the left ventricle of a patient with heart failure.

Typeset in LaTeX using a template by Berry Holl with modifications from Daniel Carrera

Faculty of Medicine, Department of Clinical Physiology
ISBN: 978-91-7619-484-3 (print), 978-91-7623-979-7 (pdf)
1652-8220
Printed in Sweden by Media-Tryck, Lund University, Lund 2017

The wisdom of the heart
having no concern with the erection or demolition of theories
any more than with the defence of prejudices,
has no random words at its command.

Joseph Conrad, *Nostromo*

The heart is deceitful above all things, and desperately wicked: who can know it?

Jeremiah 17:9, KJV

Contents

II Research papers

List of publications

This thesis is based on the following publications:

I **Quantification of left and right atrial kinetic energy using four-dimensional intracardiac magnetic resonance imaging flow measurements**

P. M. Arvidsson, J. Töger, E. Heiberg, M. Carlsson, H. Arheden
Journal of Applied Physiology, vol. 114, 1472-81 (2013).

II **Vortex ring behavior provides the epigenetic blueprint for the human heart**

P. M. Arvidsson, S. J. Kovács, J. Töger, R. Borgquist, E. Heiberg, M. Carlsson, H. Arheden
Scientific Reports, 6:22021 (2016).

III **Left and right ventricular hemodynamic forces in healthy volunteers and elite athletes assessed with 4D flow magnetic resonance imaging**

P. M. Arvidsson, J. Töger, M. Carlsson, K. Steding-Ehrenborg, G. Pedrizzetti, E. Heiberg, H. Arheden
American Journal of Physiology: Heart and Circulatory Physiology, 312:H314-28 (2016).

IV **Hemodynamic forces using 4D flow MRI: a potential biomarker of left ventricular dyssynchrony in heart failure**

P. M. Arvidsson, J. Töger, G. Pedrizzetti, R. Borgquist, M. Carlsson, E. Heiberg, H. Arheden
Journal of Cardiovascular Magnetic Resonance (submitted manuscript).

Abstract

Magnetic resonance imaging enables detailed *in vivo* study of complex flow through 3D, time-resolved phase contrast imaging (4D flow). 4D flow may reveal previously unknown aspects of the physiology of intracardiac blood flow, and possibly elucidate pathophysiological processes that have yet to manifest themselves outside the heart.

The purpose of this thesis is to examine the physiological role of intracardiac flow phenomena, in order to better understand the normal function of the heart and provide a backdrop against which future studies into disease processes can be compared. The thesis consists of four studies with the following aims:
I) to quantify atrial blood kinetic energy (KE),
II) to evaluate the relationship between left ventricular vortex ring formation and myocardial motion,
III) to quantify the hemodynamic force exchange between blood and myocardium in both ventricles, and
IV) to compare hemodynamic forces in dyssynchronous, failing left ventricles with normal findings.

Study I revealed significant differences between left and right atrial KE. Systolic KE was determined to a large extent by atrial volume and the systolic velocity of the atrioventricular plane, which differs between the left and right sides of the heart. Diastolic KE increased more in the left atrium, likely reflecting suction-initiated filling driven by left ventricular recoil. Rotational blood flow KE decay was slower than non-rotational KE decay, indicating a potential enhancement of cardiac function through energy preserving macroscopic flow structures.

Study II demonstrated a strong spatiotemporal coupling between the vortex ring boundary and the endocardial boundary, suggesting that the normal development of the left ventricle is guided by the shear layer generated by the vortex ring. The coupling may act as a dynamic optimization mechanism to facilitate fluid transport at varying levels of cardiac output. In contrast, failing ventricles show no connection between the vortex ring and endocardium, suggesting that the adaptive coupling of the myocardium to the shear layer is disrupted.

Studies III and IV demonstrated that biventricular hemodynamic forces are similar between healthy hearts regardless of size, and reflect fundamental aspects of flow redirection;

this homogenous appearance is significantly altered in heart failure. The findings elucidate a previously unknown 'slingshot' force that appears to result from contraction of the septum and RV free wall. In left ventricular dyssynchrony, several different hemodynamic force patterns were seen, which could indicate different degrees of detrimental effects on myocardial function and hence predispose to varying treatment response.

Together, the findings in the thesis have advanced the knowledge on intracardiac flow at rest. To further validate their physiological importance, it is necessary to evaluate intracardiac flow during physical exercise.

Populärvetenskaplig sammanfattning

Hjärtat är en muskelpump vars huvudsakliga syfte är att skapa blodflöde. En stor del av hjärtforskningen har fokuserat på dess förmåga att alstra tryck, eftersom blodtryck är lätt att mäta. Förhållandet mellan blodflödet inuti hjärtat och hjärtats funktion är därför mindre känd. Den tekniska utvecklingen inom magnetresonanstomografi (MR, magnetkamera) medger nu detaljerade mätningar av tredimensionella blodflödesmönster inuti hjärtat. Tekniken kallas fyrdimensionellt flöde (tre dimensioner i rummet + tid) och kan användas för att beräkna tidigare okända aspekter av hjärtats funktion, till exempel blodets rörelseenergi, virvelbildning inuti hjärtats kammare, och kraftutbytet mellan blodet och hjärtmuskeln. Dessa variabler kan potentiellt bidra till hjärtats funktion, och skulle kunna användas för att förbättra diagnos och prognos för hjärtsjukdomar, men är i nuläget så gott som sett okända. För att förstå deras roll för hjärtfunktionen är det nödvändigt att kartlägga dem i friska hjärtan och jämföra med sjuka hjärtan.

I **delarbete I** visades hur rörelseenergin i hjärtats förmak varierar över tid, och att mängden energi återspeglar hjärtats pumpfunktion. Energin bevarades i större utsträckning i roterande flödesmönster jämfört med rakt flöde. Arbetet är den första heltäckande mätningen av rörelseenergi i hjärtats förmak och möjliggör framtida studier på avvikande blodflödesmönster, till exempel vid förmaksflimmer vilket är en folksjukdom med stora konsekvenser för såväl den enskilda patienten som för samhället.

I **delarbete II** användes en världsunik mätmetod för att visa hur hjärtats dimensioner är anpassade för att rymma den virvelring som uppstår när hjärtat fylls med blod. Förhållandet mellan virvelringen och kammarens dimensioner skulle kunna användas som ett kliniskt mått på hjärtfunktionen och är sannolikt viktigt för hjärtats funktion under fysiskt arbete. Fynden har också potential att förbättra utformningen av syntetiska hjärtklaffar.

Delarbete III är den första studie som undersökt kraftutväxlingen mellan blodet och hjärtmuskeln i båda kamrarna med en tredimensionell metod. Fynden kastar nytt ljus över hur hjärtats fyllnad går till, och visade också på en aldrig tidigare beskriven funktion hos hjärtskiljeväggen. I **delarbete IV** studerades samma fenomen i patienter med hjärtsvikt och osynkroniserad kammarkontraktion. Jämförelsen visade att sviktande hjärtan slösar energi i olika utsträckning, vilket dels kan bidra till sjukdomsutvecklingen, och dels skulle kunna förutspå vilka patienter som har bäst nytta av en viss behandling.

Abbreviations

2ch	two-chamber view
3ch	three-chamber view
4D flow	three-dimensional, time-resolved phase contrast flow measurements
ATP	adenosine triphosphate
AV plane	atrioventricular plane
AVPD	atrioventricular plane displacement
bSSFP	balanced steady-state free precession
CRT	cardiac resynchronization therapy
ECG	electrocardiogram
EDPVR	end-diastolic pressure-volume relationship
ESPVR	end-systolic pressure-volume relationship
FID	free-induction decay
FTLE	finite-time Lyapunov exponent
GRE	gradient echo
IVPG	intraventricular pressure gradient
KE	kinetic energy
LA	left atrium/left atrial
LBBB	left bundle branch block
LCS	Lagrangian coherent structures
LV	left ventricle/left ventricular
MRI	magnetic resonance imaging
NRKE	non-rotational kinetic energy
RA	right atrium/right atrial
RKE	rotational kinetic energy
RMS	root mean square
RV	right ventricle/right ventricular
RVOT	right ventricular outflow tract
THVV	total heart volume variation
VFR	vortex formation ratio

Acknowledgements

This thesis would not exist without the help, feedback, support, intervention, and prayers of a lot of people. I wish to express my appreciation to everyone who has contributed, and my special gratitude to the following:

Håkan, for teaching me to think — and to do. I am not proud of what I am, but I am grateful for what I have been given. Thank you for your perseverance in preparing me for the future, even when it hurts. **Marcus**, for leading by example and speaking your mind. **Einar**, for your technical expertise and down-to-earth approach to things in general. **Johannes**, for being blunt when necessary, elaborate when possible, and honest always. **Katarina**, for reality checks, support, and encouragement. **Mikael**, for the most fun I've ever had while delineating ventricles — *my heart will go on.* **David**, for fruitful discussions on physiology and other subjects, for many laughs, and for sharing the joys and burdens of teaching. **Sebastian**, for your willingness to help. **Felicia**, for your enthusiasm and straightforwardness. **Pia**, for your untroubled demeanor. **Shahnaz**, for showing superhuman courage in the face of adversity. **Sascha**, for providing fresh perspectives and interesting car rides. **Nisse**, for friendship and added philosophical weight to discussions. **Bo**, for good laughs, excellent teaching, and for giving help when asked for — I'm sorry, did I break your concentration? The **techs** at the MR department, especially **Ann-Helen**, for showing me how it's done. **Jonas** and the **colleagues in the clinic**, for creating a welcoming workplace and taking the time to teach me whenever I ask.

Sándor, for providing an intellectual force that helped me overcome the inertial barriers of science; your joyful approach to physiology helped set things in motion back in 2010. **Gianni**, for your can-do attitude, brilliant engineering skills, and patience. **Study participants**, without you there would be no new discoveries. **Reviewers** of the papers in the thesis, for anonymous yet immeasurably valuable feedback and suggestions that vastly improved the quality of the science presented here. **Funding bodies**, especially Svensk Förening för Klinisk Fysiologi, Maggie Stephens Stiftelse, Hjärt-Lungfonden, and Region Skåne, for helping fund my research and travels. **Medical students** I've taught, and learned from.

Eva, Gun and Paul, for your prayers. **Rickard**, for making my years in Lund immensely

more enjoyable. I would have gone mad without you. **Alexander**, for sharing my joys and burdens, for holding me accountable, and for being a friend even when I'm not. **Johannes**, for being a constant source of knowledge and inspiration in matters both sacred and mundane. **Markus**, for lasting friendship with deep roots. **Emma**, for being dependable.

Margareta and Bengt, for showing me how blessed life can be when you put God first. **Karin**, for reminding me that the best things in life are free. **Teje**, for leading the way — all the way. **Erik**, for your unwavering support. **Dad**, for sparking my interest in how the world is put together. When I was 7, you told me that fluid dynamics is a complex subject matter. You were right. **Mom**, for teaching me the importance of listening. I'm still learning. **Mirjam**, for enduring these past months... and years, for supporting me, for challenging me, for making me want to become better, and for loving me.

God, I have trusted in Your loving kindness; my heart shall rejoice in Your salvation.

Lund, 26 April 2017

Part I

Research context

Chapter 1

Introduction

If I have seen further it is by standing on the shoulders of Giants.

Isaac Newton, letter to Robert Hooke, Feb 15, 1676

A thesis that seeks to contribute something new to the field of cardiac physiology must begin at the appropriate place. Since the heart has been the focus of intense study throughout medical history, a few historical stops are warranted before diving into the subject matter.

Beginning around 1490, Leonardo da Vinci studied the anatomy and function of the human circulatory system through postmortem examinations, drawings, and models of the heart and vessels [1]. da Vinci was present at a pig slaughter where the animal was killed by impaling its heart with a sharp tool [2]. He noticed that the tool would move in a pendular fashion while still stuck in the ribcage, and concluded that the pivoting indicated a predominantly longitudinal motion of the heart, which is now considered a fundament of normal cardiac function [3]. Other observations include the sequential contraction of the atria and ventricles, and the interaction between vortex flow and valvular structures, e.g. eddy flow into the sinuses of the aortic valve, verified over 400 years later [4]. da Vinci's line of enquiry was mainly observational and descriptive, not interventional, and he emphasized the importance of accurate pictorial renditions of the studied anatomy [1, 5].

In 1628, William Harvey published his landmark book *De Motu Cordis* in which he described the pumping action of the heart and the circulatory system. This contribution was the first notion of the circulatory system as a closed loop – although Harvey could not visualize the capillary beds and thus was unable to bridge the gap from the arteries to the veins. Harvey recognized that while the left and right ventricles are both muscular pumps, they serve different purposes. His most important contribution, however, was likely his approach to translational cardiovascular research, which combined hypotheses, experiments, observations and interpretation to arrive at a mechanism-based model of the circulatory system [6].

In his seminal 1669 work *Tractatus de Corde*, Richard Lower described the motion of

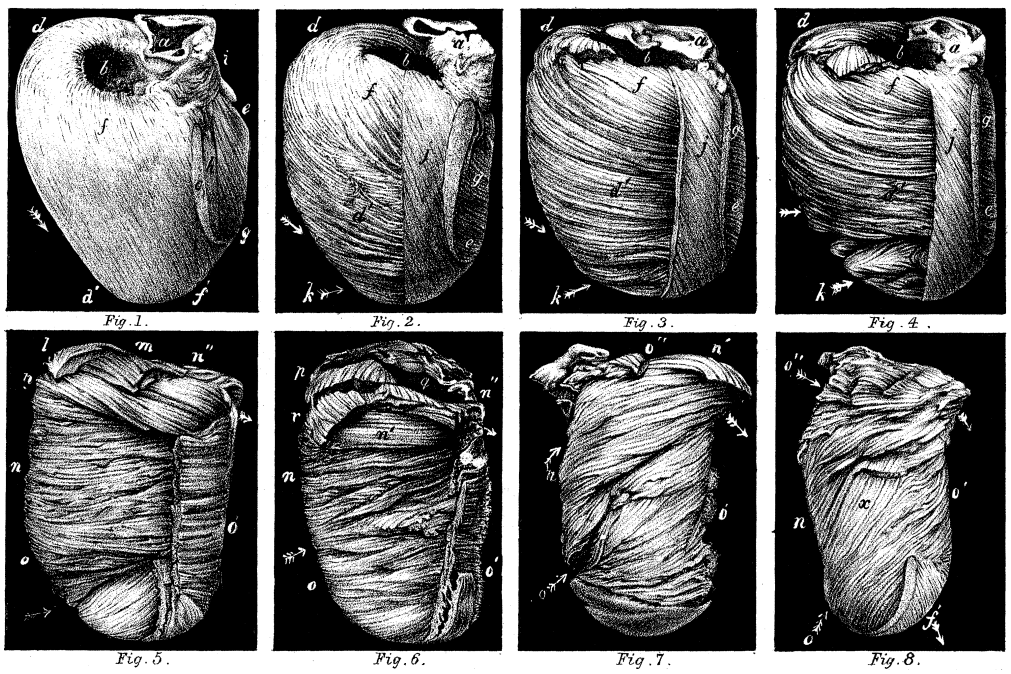

Figure 1.1: Posterior view of sheep heart dissected by Pettigrew [8]. Note the transition in the alignment of cardiac muscle 'fibers' from the left-handed epicardial layer (top left), via the circumferential middle layer, to the right-handed endocardial layer (bottom right). Courtesy of JSTOR.

blood through the pulmonary circulation, its color change when subjected to air, and the first known blood perfusion. By excising intact hearts from animals, he demonstrated that the contractile effect of cardiac tissue remained even in the absence of blood [7]. He also noted that the muscular cells of the heart were arranged in a spiral-like pattern whose direction varied with its location in the ventricular wall. Building on this finding, James Bell Pettigrew studied the structural arrangement of the heart in fish, birds, mammals (including baleen whale, armadillo, and giraffe), and humans. Through a series of meticulous dissections carried out in 1858, he described a gradual change of directional alignment of muscle fibers in the ventricular myocardium, from the endocardial to the epicardial aspect [8]. An example of his findings is shown in Fig. 1.1. The helical and progressive arrangement of cardiomyocytes would later turn out to be crucial both for generation of the blood pressure needed in the systemic circulation [5], and for efficient emptying of the ventricles despite limited shortening of the individual myocytes [9].

The world changed in 1859 when Charles Darwin released *On the Origin of Species*. Natural selection would emerge as the explanatory paradigm of the variance seen in biological systems, but the mechanism of heredity remained shrouded in mystery. Although deoxyribonucleic acid (DNA) was first described in 1869 by Friedrich Miescher (who named it "nuclein"), its purpose and even existence was controversial for years [10]. When Wat-

son & Crick were able to characterize the molecular structure of DNA in 1953 it opened the field of genetics and helped spark the biomedical revolution that is still ongoing. More recent additions to evolutionary theory include the concept of **epigenetics** [11]. An epigenetic trait is defined as "a stably heritable phenotype resulting from changes in a chromosome without alterations in the DNA sequence" [12]. Epigenetic phenotypes appear guided by changes in the environment of the cell, e.g. altered flow conditions along the endothelial lining of the heart [13].

It is clear that discoveries of vast importance have been made with limited means – observation, and depiction of cardiovascular anatomy have provided immense insights into the function of the heart. Some of these insights have seen a translation into clinically useful knowledge that benefits patients on a daily basis. Conversely, the lack of research tools has set equally significant limitations to what could be inferred; for example, if William Harvey would have had access to a microscope, he could have visualized the capillary bed, connected the arterial and venous systems, and produced the first comprehensive model of a closed circulatory system.

While we no longer hesitate to say that the heart has two ventricles (Avicenna was adamant there was three), our mechanistic understanding of cardiac pumping remains limited. Today's population is increasingly likely to suffer and die from cardiovascular disease [14]. The increase is partially explained by improvements in living standards – after all, the cumulative mortality of each human being approaches 1, regardless of reason – and while modern treatments of cardiac disease have in many cases decreased its immediate lethality, surviving patients face an increased incidence of heart failure.

Heart failure has been defined as inability of the heart to pump blood to adequately meet the body's metabolic demands under normal filling pressures [15, 16]. Most commonly, it is manifested as a syndrome with sustained matching between cardiac output and metabolic demands, but at the cost of dysregulated fluid balance, increased filling pressures, increased myocardial energy consumption, and chronical overstimulation of the renin-angiotensin-aldosterone system, effects secondary to increased sympathetic tone. As the name suggests, heart failure is a lethal condition which represents a significant fraction of total health care costs and causes tremendous suffering for individual patients – more than 50% of patients die within five years of diagnosis [17]. Breakthroughs in treatments have been scarce [18–20], and most treatments are indicated only for heart failure with reduced ejection fraction. Approximately half of all patients with symptomatic heart failure have normal or near-normal ejection fraction, which means treatment options are even more lacking. It would be preferable to detect heart failure at a much earlier stage, to stall its progression and improve the quality of life for patients [15].

Fundamentally, the purpose of the heart is to pump blood. Even slight disturbances in this function could therefore herald disease, and could potentially be used as a tool for early diagnosis. However, our ability to do so is hampered by our lack of understanding of the heart as a dynamic organ of flow. Such an understanding requires an integration of cardiac anatomy, regulatory physiology, and cellular and subcellular functions under vary-

ing metabolic states. In order to be mechanistic and generalizable, it must also intuitively fit into the framework of Newtonian physics, and thus be characterizable in terms of blood and tissue motion, pressure gradients and other physical quanta.

The emergence of new instruments and modalities has consistently opened up new areas for scientific enquiry. One of the most recent imaging modalities to do so is that of **magnetic resonance imaging**. The overarching purpose of this thesis is to make use of recent advances in magnetic resonance imaging, to extend our knowledge of the function of the heart as a pump. Focus will be placed on quantification of intracardiac flow patterns, with the purpose of integrating them in a physiologically and physically meaningful framework that can be translated from healthy to diseased hearts.

1.1 Cardiac physiology: form and function

This section serves to introduce the reader to an integrative understanding of the heart's physiology, from the cellular level to the pumping function and regulation of the entire heart, in order to contextualize the contributions of this thesis.

1.1.1 Cardiac anatomy

The human heart, shown in Fig. 1.2, is located in the mediastinum inside the thoracic cavity, on top of the diaphragm and enclosed in the pericardial sac. The pericardium is a soft but essentially non-distensible serous membrane that contains a small amount of pericardial fluid, which acts as a lubricant and permits the heart to contract freely. The visceral side of the pericardium adheres to the left ventricle, left atrium, right ventricle, and right atrium, as well as the aortic root. The sum of these parts (the contents of the pericardial sac) constitutes the **total heart volume** [21].

The left ventricle supplies the systemic circulation with oxygenated and pressurized blood, and the right ventricle feeds oxygen-depleted blood through the pulmonary circulation to enable gas exchange with the surrounding air. Under normal conditions, the resistance in the pulmonary circulation is approximately one-fifth of that in the systemic circulation. Flow results when a pressure gradient overcomes a resistance,

$$Q = \frac{\Delta P}{R}, \tag{1.1}$$

where Q is the flow, ΔP is the pressure difference over the resistance, and R is the resistance. In order for the two ventricles to pump the same amount of blood (a prerequisite over time), the left ventricle therefore has to apply a force (pressure) that is five times greater than that of the right ventricle. To cope with the higher workload, and associated increase in wall tension, the left ventricle has a significantly thicker myocardium. Cardiac pumping is an energy-demanding process, and oxygenated blood is supplied to both ventricles and atria from the coronary arteries, which branch off from the aortic sinuses in the aortic valve.

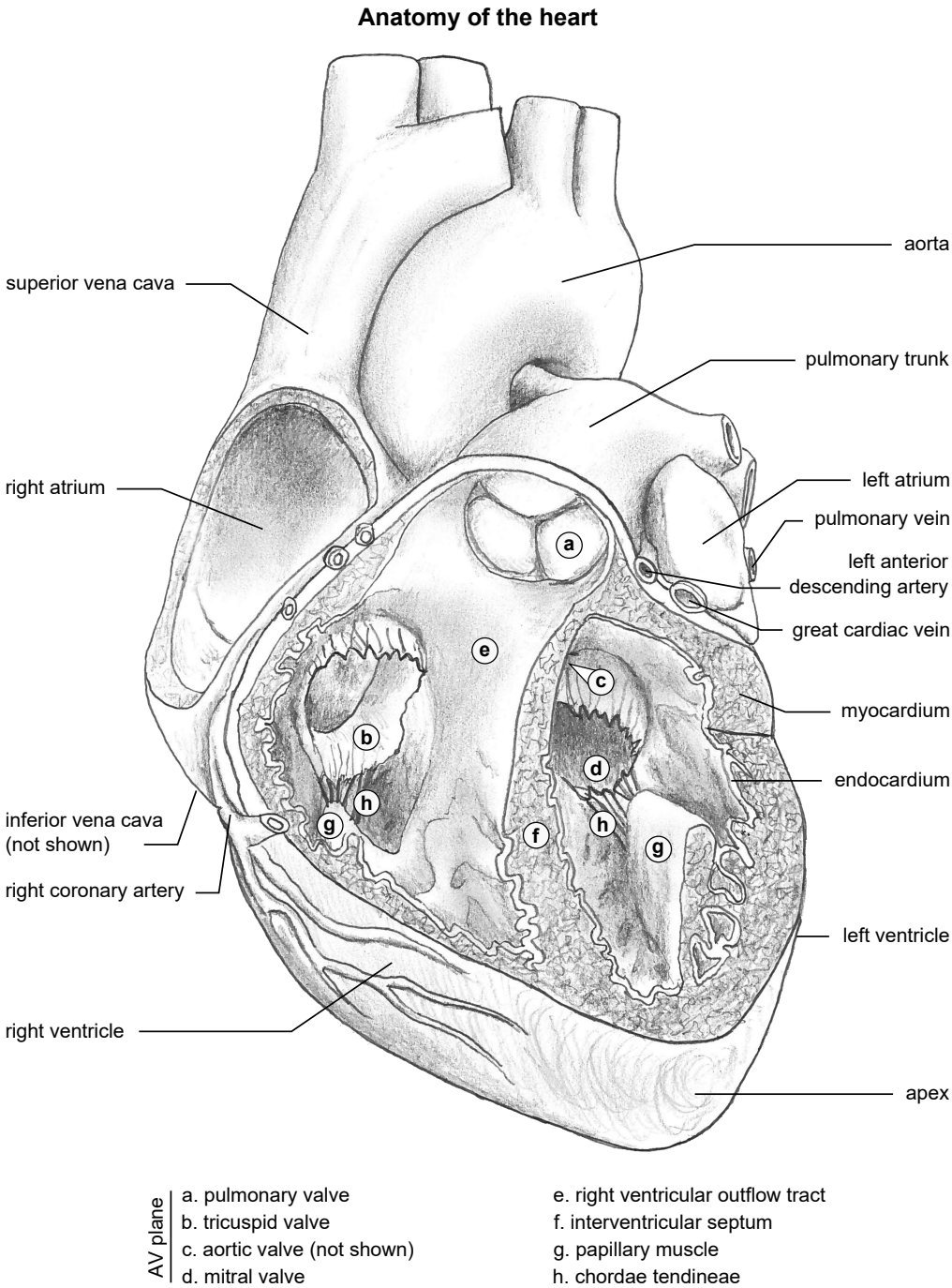

Figure 1.2: Anatomy of the heart, drawn from anatomical model. The pericardium and anterior parts of the ventricles have been removed, including the anterior papillary muscles and their associated chordae tendineae.

Forward flow is ensured by the valve apparatus, i.e. the aortic and pulmonary valves (also called semilunar valves), and the mitral and tricuspid valves (**atrioventricular valves**) that separate the ventricles from the atria.

The atria receive blood from the pulmonary and caval veins, which also serves as anchor points for the posterior (basal) aspect of the heart. The left and right sides of the heart are separated by the interventricular septum (shared by the ventricles) and the atrial septum. Furthermore, the ventricles are separated from the atria by a fibrous structure known as the **atrioventricular plane** (AV plane).

The AV plane serves as the anchoring point for the AV valves as well as the aortic root and aortic valve. The AV valves are also connected to the ventricular myocardium via the chordae tendineae, which together with the papillary muscles prevent the valve leaflets from prolapsing into the atria during ventricular contraction. The atrioventricular valves have to resist the systolic blood pressure without allowing any backward flow, and they must be compliant enough to permit fast and unobstructed inflow during cardiac filling, which normally occurs at low blood pressure.

Both the ventricles and the atria are made up of specialized muscle cells called cardiomyocytes. Together, these cells form the **myocardium**, the muscular tissue that performs the contractile work of the cardiac chambers. The innermost layer of myocardium is covered by endothelial cells, called the **endocardium**.

1.1.2 The electrical conduction system

The superior part of the right atrium houses an area of specialized myocytes called the sinus node. Cardiomyocytes are electrically active cells which depolarize and repolarize spontaneously at regular intervals. The sinus node has the most rapid self-depolarization cycle in the heart which effectively sets the pace for the surrounding cells. Cardiomyocytes are connected to one another via gap junctions, which turns them into an all-or-nothing electrical unit – a **functional syncytium**. If one cell depolarizes, so will the others, unless something is stopping them. The sequential depolarization of atria and ventricles is the initiating mechanism behind cardiac pumping, through a phenomenon known as **excitation-contraction coupling**. Muscular contraction is preceded by electrical excitation (depolarization) of the cells.

Electrical conduction via cell-cell transmission is slow. Normally, depolarization is instead propagated by specialized cardiomyocytes known as Purkinje fibers, which constitute the electrical **conduction system** of the heart. The conduction system rapidly conveys the electrical depolarization from its origin in the sinus node, via the **atrioventricular node** (connecting the atria to the top of the interventricular septum) into the ventricles. After passing the AV node, the conduction system splits into left and right branches, one for each ventricle; the left branch is then further split into anterior and posterior parts. The conduction system enables near-instantaneous depolarization of the entire ventricle, which results in synchronized and efficient contraction.

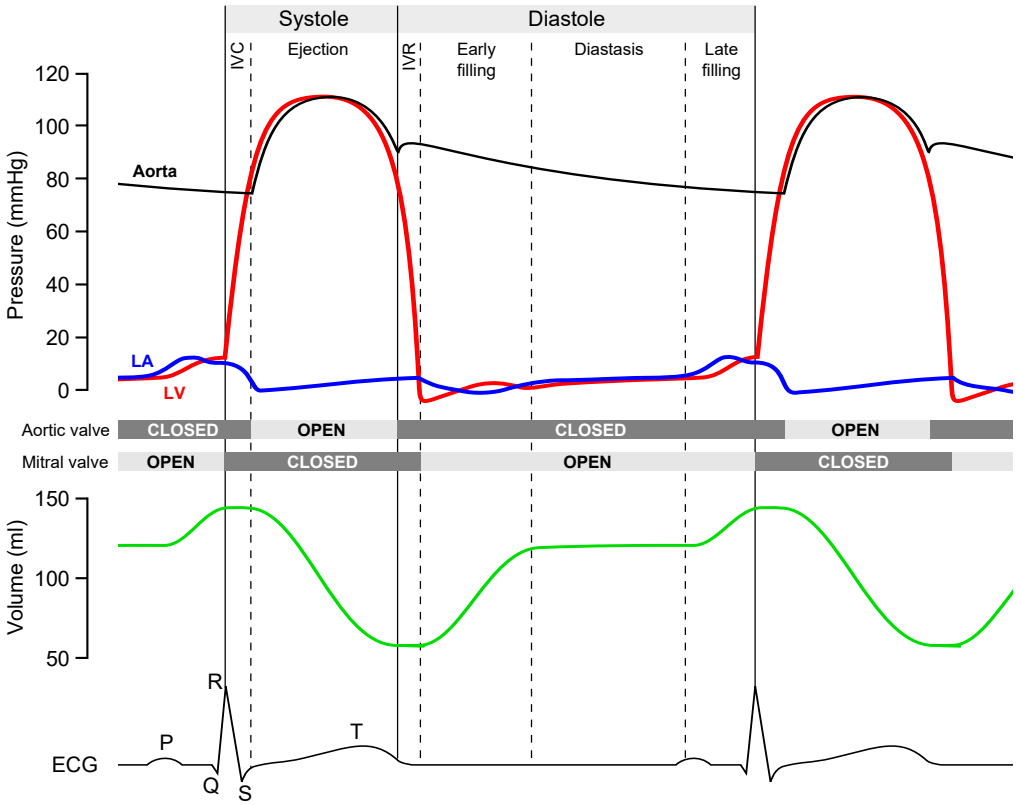

Figure 1.3: Wiggers diagram showcasing pressures and LV volume over the course of two cardiac cycles. LA, left atrium; LV, left ventricle; IVC, isovolumic contraction; IVR, isovolumic relaxation.

1.1.3 The cardiac cycle

The cardiac cycle can be effectively visualized using a Wiggers diagram (Fig. 1.3), named after its inventor Carl J Wiggers. For simplicity, only the left heart is depicted in the figure.

The cardiac cycle begins with the spontaneous depolarization of the sinus node (P wave in the ECG). This causes the atrium to contract, increases atrial blood pressure, and causes blood to flow into the ventricle. By contracting, the atria also exert a pull on the ventricles, which 'primes' the ventricles for more efficient subsequent ejection through the Frank-Starling mechanism.

After atrial depolarization, the atrioventricular node introduces a slight delay (P-Q interval in the ECG) before the depolarization wavefront reaches the ventricles. Once the ventricle starts to depolarize (QRS complex in the ECG), its contraction causes ventricular pressure to increase sharply. The increase in pressure forces blood towards the base of the ventricle, causing the mitral valve to close. Due to the closed valves, ventricular volume remains constant – this period is referred to as the **isovolumic contraction** (IVC). Once the

ventricular pressure exceeds the aortic pressure, the aortic valve is forced open and blood is accelerated into the aorta – the **ejection** phase begins. Ventricular blood pressure increase is slowing down, and approximately halfway through ejection, it starts to decrease. The ventricle has now started its repolarization process (T wave on ECG). Aortic pressure now exceeds ventricular pressure; however, the outflow continues for awhile due to the inertia of the outflowing blood [22]. The pressure difference ΔP between aorta and ventricle now serves to accelerate aortic blood back towards the ventricle, which quickly closes the aortic valve, ending the ejection. The period from closure of the mitral valve to closure of the aortic valve is one definition of **systole**, the ejection phase.

As the ventricle repolarizes, its pressure continues to decrease through the process of **isovolumic relaxation**, to a point where it undershoots the atrial pressure [23]. This undershoot effectively turns the ventricle into a suction pump [24] that aspirates blood from the atrium [25–29]; as a result, the mitral valve opens, which commences the **early filling phase**.

Once the pressure difference between atrium and ventricle is equalized and the inflowing blood is impeded by the myocardial wall, the relaxed heart enters a temporary state of equilibrium called the **diastasis** [26, 30]. Diastasis disappears when heart rate becomes elevated, for example during exercise [31], as the early and late filling phases gradually merge together [32].

Diastasis is concluded when the sinus node depolarizes anew, which subsequently leads to atrial contraction and marks the beginning of a new cardiac cycle. The time spent by the relaxing and filling ventricle, from the isovolumic relaxation until the end of the late filling phase, is collectively called **diastole**.

1.1.4 Atrioventricular plane displacement in cardiac pumping

Let us now revisit the anatomy of the heart from a functional perspective. During systole, myocyte shortening will lead to ejection of ventricular blood and subsequent shortening and narrowing of the ventricles. Due to the predominantly longitudinal arrangement of the myocardium, shortening will dominate over narrowing (recall Leonardo da Vinci's notes from the pig slaughter) [2, 5]. The apex of the heart remains relatively stationary, since the pericardium is attached to the thoracic wall. Therefore, ventricular shortening acts to pull myocardium away from the base of the heart, thereby exerting a pull on the atria via the AV plane. The effect of pulling the AV plane towards the apex can be likened to drawing the plunger on a syringe; the resulting expansion of the atrium causes atrial pressure to drop, which creates a pressure gradient that aspirates blood flow into the atria [34]. In this view, the four-chamber heart acts primarily as a piston pump that ejects blood through **atrioventricular plane displacement** (AVPD), in other words a primarily longitudinal mode of pumping (apical-basal shortening) (Fig. 1.4). The contribution of AVPD to stroke volume can be calculated as the product of the epicardial short-axis area and the distance traveled by the AV plane [35]. The reason for using the epicardial rather than

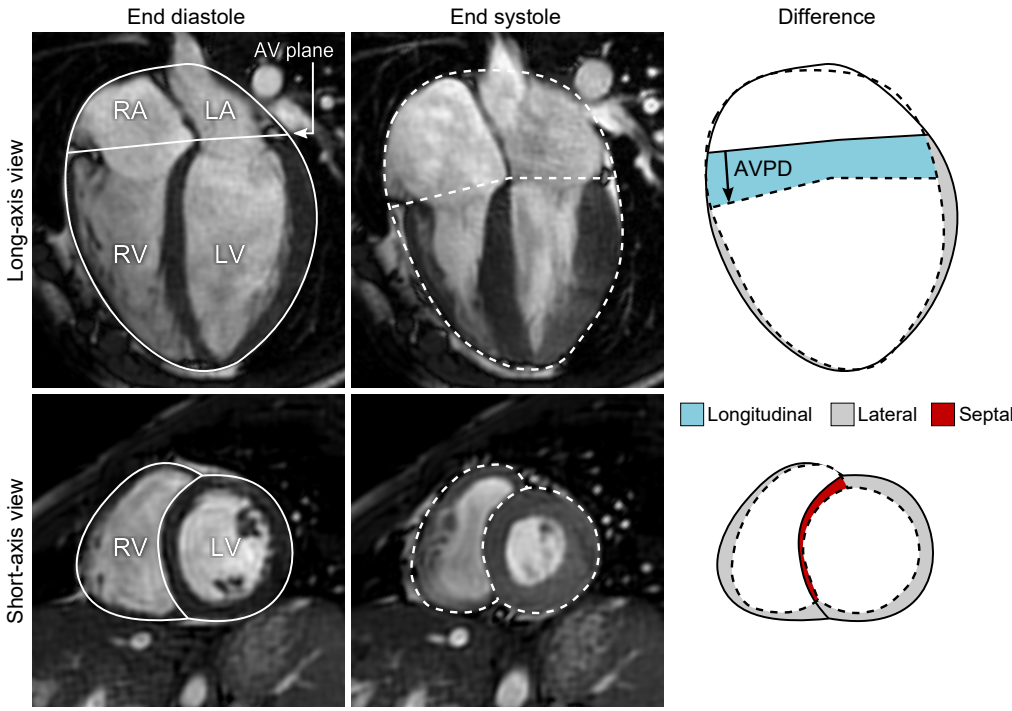

Figure 1.4: Principles of cardiac pumping. Left: MR images of a normal heart at end diastole shown in long-axis and short-axis views. The atrioventricular plane and epicardial boundaries have been delineated. Middle: end-systolic phase. Note that the AV plane has been pulled downwards towards the apex. Right: superposition of end-diastolic and end-systolic epicardial contours reveals the three principal modes of pumping. The longitudinal contribution to ventricular stroke volume is shown in blue. Note that RV AVPD is longer than LV AVPD. The lateral component is shown in gray. Note that this area corresponds to the outer volume changes of the heart. The septal component is shown in red. Normally, septal contraction contributes to LV pumping, and detracts slightly from RV pumping [33]. The radial contribution to pumping is calculated as the sum of lateral and septal pumping.

the endocardial boundaries is that the myocardium and its individual cells are considered an incompressible fluid. As it shortens, it therefore follows that individual cells also thicken in order to preserve its cellular membrane intact. Wall thickening is therefore a secondary phenomenon, not a mechanism of pumping, and so must be removed from the calculations [36].

The reciprocal coupling between ventricular emptying and atrial filling was initially thought to be balanced, meaning that the contents of the pericardial sac would remain constant over the cardiac cycle [37]. The concept of **constant-volume pumping** would be an energetically efficient solution, as no work is wasted on moving extracardiac tissue. Initial studies lent some support to the idea. For example, Hoffman and Ritman [38] demonstrated a **total heart volume variation** (THVV) of 2.7% in dogs. With increasingly fine measurement techniques, the number has been found closer to 5-10% [39, 40], and the cardiac center of volume shifts only 2-3 millimeters over the cardiac cycle [21]. Total heart volume decreases during systolic ejection and recovers during the early rapid filling phase [41–43].

During ventricular ejection, the atria receive and store incoming venous blood, thus acting as reservoirs. The reservoir volume, however, is not matched to the ventricular stroke volumes. Typically, the atrial reservoir volume makes up 40-60% of the ventricular stroke volume, while the majority of the remainder is made up by the conduit volume, i.e. blood that flows through the atrium during early diastolic filling [44, 45]. This explains the THVV [25]. If the heart would pump only by longitudinal shortening, the total heart volume variation would be caused solely by a volume deficiency on the atrial level. There is, however, also a significant radial narrowing of the ventricles during systole; indeed, most of the THVV arises from the basal parts of the ventricles [40], as shown in Fig. 1.4. The left ventricle produces approximately 60% of its stroke volume by AVPD [36] while the rest stems from narrowing of the ventricle, both the lateral wall and the septum [33, 36] . The right ventricle generates approximately 80% of its stroke volume from AVPD, and the rest from radial pumping [46]. The septum normally moves towards the LV during ejection, which detracts slightly from RV ejection [33]. The position of the septum is affected by ventricular diastolic pressure and therefore shifts position depending on the respiration. Inspiration causes intrathoracic pressure to decrease, which increases the venous return to the right heart and shifts the septum towards the LV.

Total heart volume variation thus arises from a temporal mismatch in cardiac ejection and inflow, and manifests as systolic inward motion of the lateral walls of the ventricles [33]. The diastolic volume recovery, as measured by the sum of inflows to the heart (pulmonary and caval veins), corresponds to the conduit volume [25] and is generated by the radial 'rebound' driven by diastolic recoil [43]. Similarly, the AVPD-driven filling of the atria is volumetrically coupled to the longitudinal pumping of the ventricles [35, 37, 38, 47].

1.1.5 Cardiac muscle cells

The contractile function in the individual cells arises from an arrangement of intracellular filaments, briefly summarized in Fig. 1.5. The theory detailing the contractile elements of striated muscle cells is called the **sliding filament theory** and was first described in two seminal 1954 papers [48, 49]. In short, the intracellular proteins **actin** and **myosin** participate in a cycle of crosslink formation, conformational changes, and release of crosslinks.

When a cardiomyocyte is depolarized, it will respond with a transmembranous influx of Ca^{2+}. This triggers calcium-dependent calcium release from the sarcoplasmatic reticulum, leading to a rapid increase in $[Ca^{2+}]$. Some of this Ca^{2+} binds to troponin, a protein coupled to the actin filaments. Troponin normally maintains tropomyosin in a state which blocks actin's attachment site for myosin, but the added Ca^{2+} brings about shape changes which expose the active sites on the actin filaments. This enables myosin to attach to the actin filaments, an event called **crossbridge formation**. Myosin carries adenosine triphosphate (ATP), which is rapidly hydrolyzed upon crossbridge formation. This results in conformational changes to the myosin head, which effects a 'pull' on the actin filament. As a result, the filaments slide past each other, and the sarcomere shortens. Now in a shape-changed state, myosin requires additional energy to release from the actin filament. As ATP is added, the myosin head springs back to its original shape and prepares for a new cycle. Cycles continue as long as intracellular Ca^{2+} remains elevated and there is sufficient energy (ATP) to enable crossbridge formation and release. When the cardiomyocyte repolarizes (ECG T wave), Ca^{2+} will be pumped back into the sarcoplasmatic reticulum and out of the cell, ending contraction.

The relaxation of the contractile element allows the cardiomyocyte to elongate to its slack length, a process driven by the scaffolding protein **titin**. Titin, a protein of titanic size (hence the name), acts as a structural scaffold for the contractile elements of muscle cells [50, 51]. Titin is understood as a bidirectional molecular spring which modulates the tensile properties of the sarcomere. It contains several spring-like domains that are gradually compressed during systolic ejection [52]. Once the relaxation process starts and the actin-myosin complex decouples, the titin springs can release their stored energy and restore the cardiomyocyte to its slack length. Apart from restoring the cell length after contraction, titin also prevents overstretching of the sarcomere.

1.1.6 The Frank-Starling mechanism and pressure-volume loops

Cardiomyocytes will generate different amounts of contractile force depending on their starting position. If cells are stretched, the contractile elements become more sensitive to increased intracellular $[Ca^{2+}]$. The mechanisms are unclear [53], but the result is a stronger contractile force at increased sarcomere lengths. On the organ level, this has the effect of providing an instantaneous compensatory mechanism for handling different ventricular filling volumes. Increased inflow to the heart is balanced by a stronger contraction, i.e. *the heart pumps what it receives*. This is called the **Frank-Starling law of the heart**. The potential

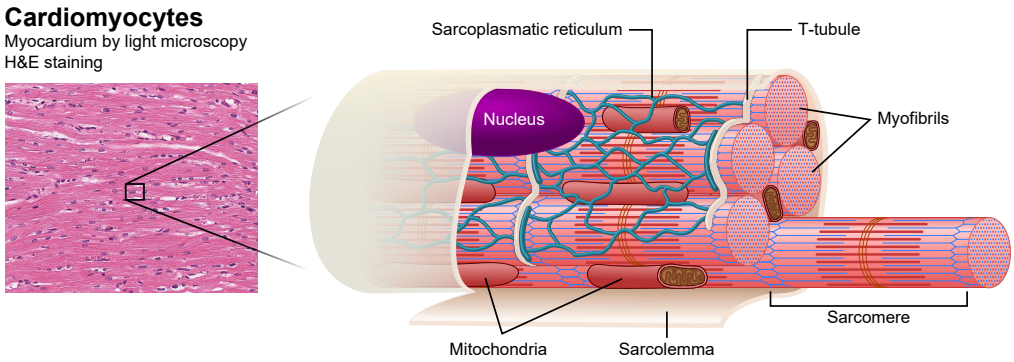

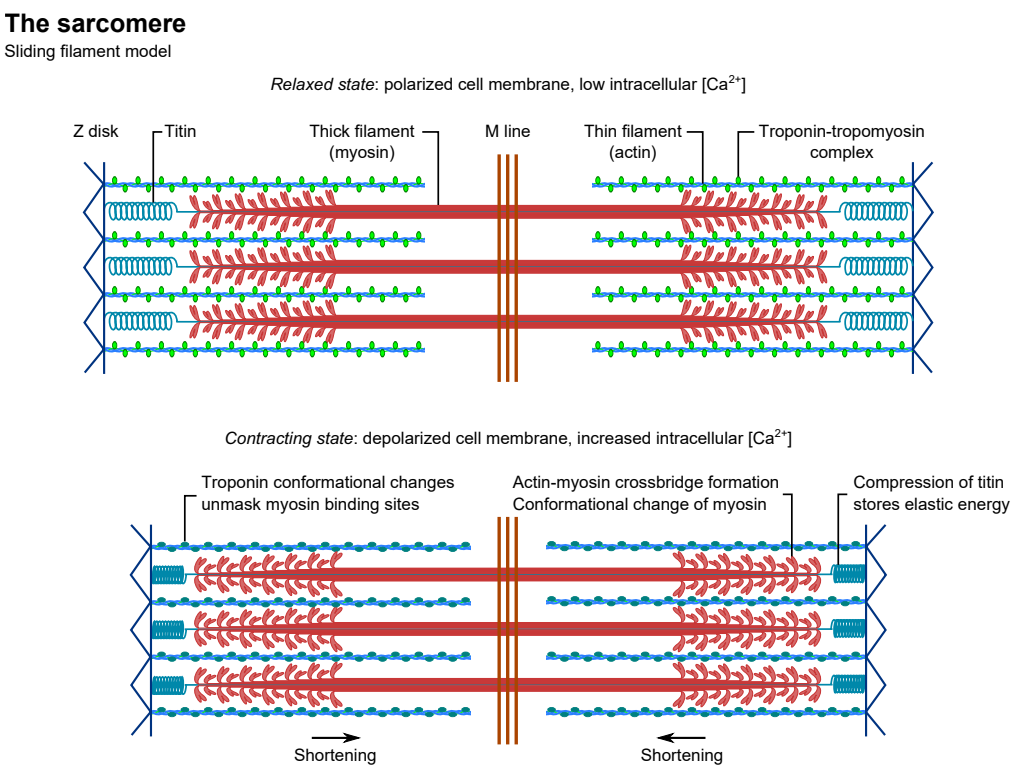

Figure 1.5: Structural layout of a cardiomyocyte and its contractile subunit, the sarcomere. Top: light microscopy of porcine myocardium (Cardiac MR Group, Lund University), and principal components of the individual cell. Cardiomyocytes are dominated by the contractile elements which are arranged in myofibrils. Myofibrils are surrounded by mitochondria and the sarcoplasmatic reticulum, which is coupled to the exterior of the cell through the T-tubules. Bottom: the sarcomere is understood as a system of sliding filaments, which alternate between relaxed and contracting states depending on the presence of Ca^{2+}. Titin is anchored to the Z-disk and M line and is compressed by the contraction; it subsequently provides a restoring force upon cessation of contraction.

to generate force is maximized at sarcomere lengths around 2.2 micrometers. At even higher lengths, the filaments start to slide apart, and fewer active sites are available for crossbridge formation.

The cardiac cycle can be visualized using **pressure-volume loops** (Fig. 1.6). Relaxed cardiomyocytes have a certain amount of elasticity, which can be plotted on a length-tension curve. The relationship between cell lengthening and tension is nonlinear; the compliance (the degree of length change as a function of applied amount of force) decreases gradually as length increases. This is caused by intracellular elements that are gradually stretched. If the cell is overstretched, these elements will break and cellular integrity is compromised. The compliance relationship can be expressed as

$$\text{Compliance} = \frac{\Delta L}{\Delta F}, \tag{1.2}$$

where L is cellular length and F is the applied force. The inverse of this function is the "stiffness" of the individual cell, i.e. how much the tension increases for a given amount of lengthening. Translating these concepts to the organ level, the ventricle, allows us to plot similar quanta. We replace cellular length with ventricular volume and force with pressure, as these units are similar. Plotting the length-tension curve of the relaxed ventricle produces the **end-diastolic pressure-volume relationship** (EDPVR), shown in Fig. 1.6. It is seen in the slope of the curve that increased filling is opposed by increasing resistance from the distended myocardium. If the slope should become steeper (indicating increased ventricular passive stiffness), e.g. due to some pathological process, the ventricle will become more difficult to fill.

As noted above, the contractile function of the individual cardiomyocyte is affected by its level of passive stretch, or sarcomere length. For a given resting state, each cell can generate a maximum (isotonic) contractile force. At the organ level, this relationship is given by the **end-systolic pressure-volume relationship** (ESPVR), the upper blue line in Fig. 1.6. The relationship is largely dependent on the degree of overlap between the actin and myosin filaments and is highly nonlinear. At short myocyte lengths, little travel is allowed in the sliding filament model and calcium sensitivity is decreased; and at very long cellular lengths, the filaments become separated, losing their overlap – passive tension then dominates. The ability of the ventricle to contract effectively follows from the vertical distance between the EDPVR and ESPVR.

An example of this is given in the right panel of Fig. 1.6, showing changes associated with exercise. Venous return increases, leading to increased filling. This causes the end-diastolic volume to increase, but the end-diastolic pressure only increases slightly since the EDPVR slope is still low. Meanwhile, the increased distension of the ventricle means that the sliding filaments are better positioned to generate force - the ESPVR is higher. In the case of exercise, the ESPVR is also shifted upwards due to the positive inotropic effects of circulating β-agonistic amines (primarily adrenaline) and sympathetic nerve stimulation of the myocardium (mediated through noradrenaline). This translates into a greater capacity

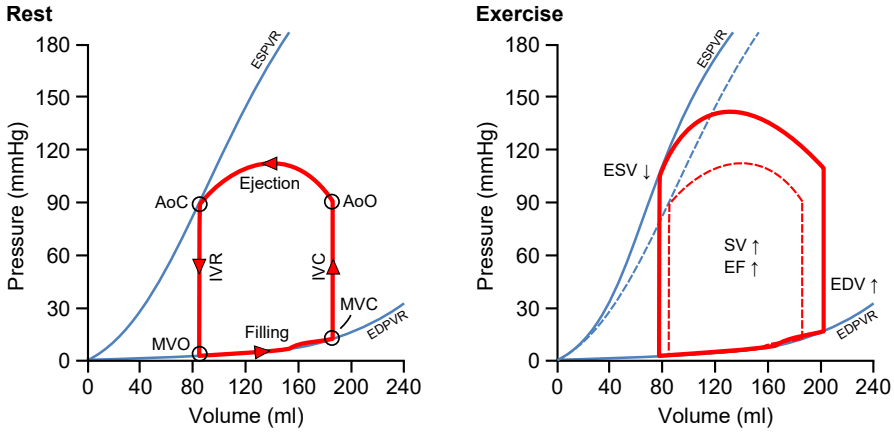

Figure 1.6: Pressure-volume loop of the left ventricle. Left: example of a normal P-V loop at rest. MVC, mitral valve closure; IVC, isovolumic contraction; AoO, aortic valve opening; AoC, aortic valve closure; IVR, isovolumic relaxation; MVO, mitral valve opening; ESPVR, end-systolic pressure-volume relationship; EDPVR, end-diastolic pressure-volume relationship. Right: changes associated with exercise. The broken line indicates the resting state for comparison. The increased blood pressure follows from increased heart rate; shorter preceding diastole means that aortic end-diastolic pressure will be higher than at rest.

to generate blood pressure; systolic pressure rises and allows more forceful ejection, causing a lower end-systolic volume. As a result, both stroke volume and ejection fraction increase.

The majority of myocardial energy consumption is directed at generating the pressures necessary to generate systolic flow. The external work W of the heart can be calculated as the area inscribed by the P-V loop, since

$$W = F \cdot s, \tag{1.3}$$

hence

$$W = \frac{F}{A} \cdot s \cdot A = P \cdot \Delta V. \tag{1.4}$$

The oxygen consumption of the myocardium is linearly related to the sum of the P-V area (the external work) and the area to the left of the loop, limited by the ESPVR and EDPVR lines. The latter area is related to the potential energy stored in the system [54, 55].

1.1.7 Diastolic function and its importance for exercise performance

So far we have considered the heart and its cycle with a focus on its systolic function, i.e. the role of the ventricle as a longitudinally contracting pump. Diastole, however, presents a more complex challenge for the heart, especially during physical exertion. At rest, approximately 1/3 of the cardiac cycle is spent ejecting blood, a process which accounts for the vast majority of the heart's energy expenditures. The remaining time is spent filling the heart, which at rest occurs in two separate inflow waves; the E-wave (early filling) and A-wave

(atrial kick, late filling), separated by the diastasis. The human heart is capable of increasing its output more than five-fold during exercise, and can attain heart rates of over 200 beats per minute.[1] As heart rate increases, both systolic and diastolic phases are shortened [56]. Shortening of diastole dominates, where the early and late filling waves retain most of their duration but diastasis is gradually reduced and disappears at moderately elevated heart rates [31]. At even higher heart rates, the E and A waves fuse together to form a single filling phase whose velocity slightly surpasses the sum of its E and A components before fusion [31]. Maintaining a relatively low inflow velocity even with completely fused E and A waves is made possible by enlarging the effective mitral valve orifice [57], possibly caused by the increased preload and sphericity seen during exercise [42, 58].

In this state, the ventricle and atrium operate together in a sinusoidal pattern, with reciprocal filling and emptying [32]. Given that a left ventricle can generate pressures exceeding 300 mmHg to eject blood, the limiting factor for cardiac performance lies in its diastolic properties. At maximal exertion, elite athletes can produce a cardiac output of 35 l/min with stroke volumes of approximately 200 ml [59] – figures should be doubled to account for both ventricles. Thus, under some conditions almost half a litre of blood enters the ventricles in less time than it takes to eject the same amount. The sheer mass transferred during diastolic filling indicates that the process involves more than 'simple' passive relaxation of the myocardium. Recent studies have now elucidated that diastolic filling is a complex mechanism which requires carefully balanced active relaxation (involving intracellular $\left[Ca^{2+}\right]$ decline, thin filament deactivation, and cross-bridge cycling kinetics) [60] diastolic suction by release of elastic energy [52, 61, 62], and atrial contraction.

As mentioned above, myocardial relaxation (breaking of actin-myosin crossbridges) brings about the release of potential energy stored during contraction. This energy release causes the ventricle to expand rapidly, which contributes to the rapid pressure decline observed in the isovolumic relaxation phase and continues in the initial phase of early filling. As long as ventricular relaxation occurs faster than the ventricle can fill, the ventricle acts as a diastolic suction pump. This fulfills the criterion

$$\frac{dP}{dV} < 0, \tag{1.5}$$

regardless of absolute pressure level, as defined by Katz [24]. The definition is valid regardless of heart rate; when E and A waves fuse, filling can still be accomplished by ventricular suction even with a simultaneously contracting atrium. The basally directed 'pull' of the atrial contraction on the AV plane amplifies the relaxation and expansion of the ventricle, and helps position the sliding filaments in an optimal position for subsequent contraction.

Diastolic suction is driven by a process known as **elastic recoil**, which causes the sarcomeres to return to their slack length upon relaxation. Diastolic suction is an active process which arises from the recovery of elastic energy stored by titin and other elastic elements of

[1] Maximum heart rate can be approximated by the commonly used formula $220 - \text{age}$, with considerable biological variation around the mean.

the extracellular matrix [52, 63]. The amount of energy stored depends on the contractile function of the myocardium [64]. Elastic recoil is made possibly by rapid relaxation of the ventricle. Suction is impaired if ventricular relaxation is impeded, and is enhanced by a strong preceding ventricular contraction as this stores more elastic energy [65].

In functional terms, diastolic recoil drives ventricular filling primarily by means of radial expansion of the ventricle [41, 43]. The effects of the relaxing myocardium on inflow patterns have been formulated in a mathematical framework that is normally used to describe damped harmonic oscillations, further underscoring its spring-like characteristics [66].

In summary, optimal diastolic function is of paramount importance for normal cardiac function. Since the process depends upon proper relaxation of the myocardium, it is also sensitive to disturbances in O_2 delivery, formation of extracellular fibrosis, and other pathological processes. Impaired diastolic function is a typical finding in heart failure and is commonly present in heart failure patients with preserved ejection fraction [67–71]. Assessment of diastolic function aims to determine whether a relaxation abnormality or increased stiffness is present [61], and whether filling pressures have become elevated as a result [72, 73].

1.1.8 Integrative views on flow-function coupling and cardiac anatomy

While simpler animals such as fish and mollusks have linearly arranged hearts, the human heart is characterized by a chiral[2] asymmetry between the ventricles [74, 75]. This spatially complex arrangement is established during early embryonic development. The developmental process of *cardiac looping* is believed to be influenced by cardiac loading conditions [76–79] as well as fluid-wall shear stress [13], and has been suggested to convey functional advantages compared to linearly arranged hearts. The left heart can be described in relatively simple geometrical terms as a prolate spheroid. In contrast, the right heart looks like a bit of a late addition to the side of the LV, and has a complex three-dimensional shape that wraps around the septum and gradually narrows via the infundibulum into the pulmonary trunk. This shape seems to encourage a slingshot-like rerouting of blood from the right atrium to the pulmonary valve. In the right atrium, inflowing blood is prevented from colliding head-on by the staggered configuration of the caval vein orifices. Inflow from the superior vena cava enters the anterior part of the atrium, and inferior vena cava blood flows into the posterior part. This layout causes right atrial blood to spin around in a clockwise rotational pattern [74]. The left atrium also creates rotational flow due to the arrangement of the pulmonary vein inlets [80]. If the energy of this rotational flow could be conserved, it would serve as a potential mechanism for increasing cardiac efficiency, the

[2] *Chirality* is a property relating to the asymmetry of an object. Chiral objects are distinguishable from their mirror image, which cannot brought to coincide perfectly by superposition on the original. Consider a pair of shoes; the left and right shoe share external traits and some levels of symmetry, but remain different from one another.

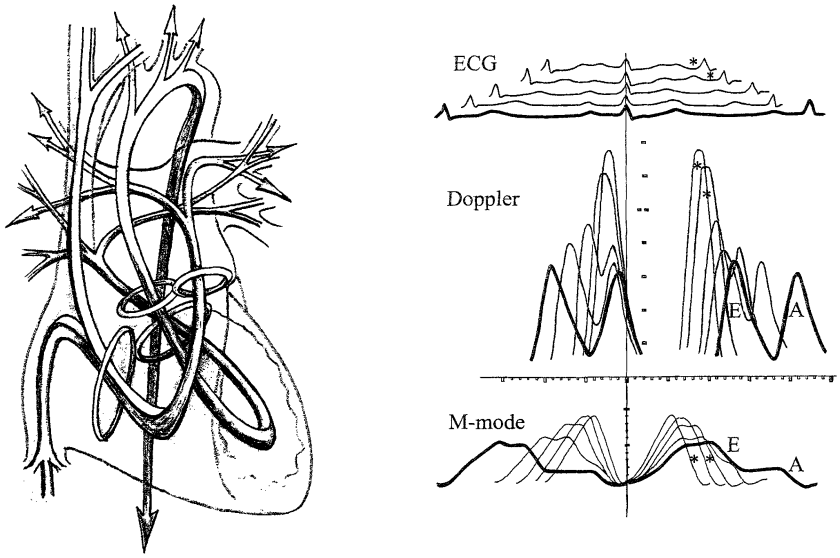

Figure 1.7: Paths of flow through the heart and dynamic changes associated with exercise. Left panel: blood flow through the heart represented by continuous bands, showing gradual redirection of blood and intertwined flow paths. Right: superimposed outlines of Doppler and M-mode traces in one subject progressing from rest to strenuous exercise. Note the gradual shift from biphasic to monophasic filling patterns (fusion of E- and A-waves) and the associated increase in inflow velocity. Images from Kilner et al. [32], reprinted with permission from Springer.

effect of which would be most palpable during vigorous physical exertion. It follows, then, that energy-efficient flow should avoid the formation of turbulence and instead preserve macroscopically ordered flow patterns for as long as possible.

Kilner et al. proposed that inflowing blood could be smoothly redirected towards the outflow tracts, while making effective use of the recoil motion of the contracting ventricles [32, 74]. As we have seen, the main challenge for the heart is to maintain efficient filling at low pressures. Being able to transition from one mode of action (resting heart beat) to another (vigorous exercise) while preserving stability by efficient utilization of flow separation and inertial balances could be an important optimization mechanism of the human heart [81] (Fig. 1.7), likely most beneficial for adequate diastolic filling.

Such optimization mechanisms can be expected to manifest themselves in several different physical quantities related to the motion of the blood. They could possibly be detected through analysis of the **kinetic energy** of intracavitary blood, since maintaining efficient forward motion of blood through rerouting or 'slinging' of blood implies preservation of its kinetic energy. The process of rerouting blood is mediated by time-varying application of **hemodynamic forces**, which are exchanged between the blood and the myocardium. These forces could therefore reveal new information regarding cardiac function. Finally, **vortex ring formation** is a preeminent phenomenon observed in ventricular filling, and its

characteristics are likely to contain unique information regarding the developmental biology and physiological state of the heart. These measures were the focus of the thesis and are discussed below.

1.1.9 Kinetic energy

Kinetic energy, according to Newton's second law of motion, is the energy carried by an object due to its velocity:

$$\mathrm{KE} = \frac{mv^2}{2}, \tag{1.6}$$

where m is the mass of said object and v its velocity. Kinetic energy is also a measure of the amount of energy spent on accelerating said object to its current velocity. Preservation of the kinetic energy of intracardiac blood could therefore be a goal in itself. When this thesis project was initiated, the kinetic energy content of intracardiac blood had scarcely been investigated in the human heart. The first study of kinetic energy in the left and right ventricles was carried out by Prec et al. in 1949 using invasive measures [82]. The authors found that KE constituted 0.4-3.1% of total LV work, and 2.4-12.5% of RV work at rest. Later work by Carlsson et al. using state-of-the-art MRI measurements found that ventricular KE averaged 1-4 mJ over the cardiac cycle, with peaks of 5-10 mJ [83]. This corresponded to <1% of the total work of the heart at rest. In the same study, simulations indicated that kinetic energy may assume a progressively greater importance during exercise – an approximately 10-fold increase for both ventricles. If rotational blood flow could 'store' kinetic energy, similar to a flywheel, it would reveal this function by having a slower rate of energy decay compared to non-rotational blood flow.

Left atrial kinetic energy during atrial contraction was investigated using echocardiography by Stefanadis et al. [84], and was found between 0.25-1.8 mJ. The KE content of right atrial blood remained completely unexplored, and left atrial blood had not been investigated using a three-dimensional method. The possibility of storing kinetic energy in the atrial blood reservoir therefore remained essentially unknown. **Study I** was conceived to address this lack of knowledge.

1.1.10 Vortex ring formation

Vortex rings can be understood as a contiguous mass of rotating fluid, and arise when sufficient flow passes through an orifice (Fig. 1.8) [85–87]. The formation of a vortex ring is caused by the appearance of a shear layer along the boundary of the inflowing fluid. Vortex ring formation has been observed in the left ventricle during early rapid filling, both in models of the heart [4, 88] and *in vivo* using a variety of imaging approaches [89–91]. Vortex ring formation in the LV has been suggested to play numerous parts in cardiac function, including facilitation of valve closure [88, 92], maintenance of low diastolic filling pressure [93], and energy-efficient fluid transport from atrium to ventricle [94].

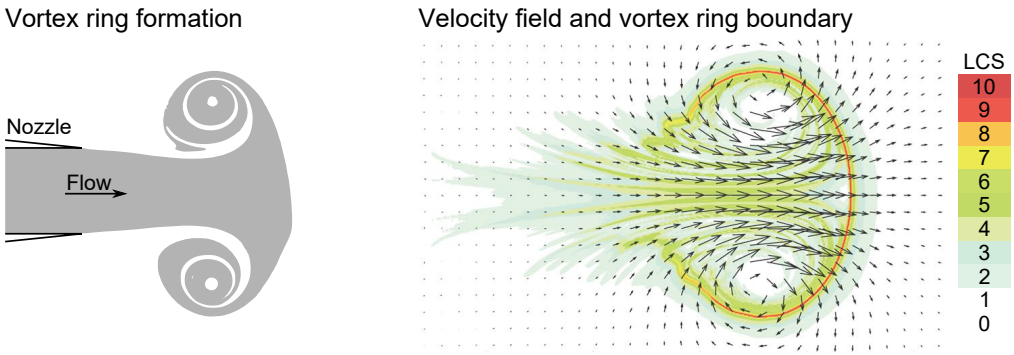

Figure 1.8: Perspectives on vortex ring dynamics. Left: Visualization of vortex ring formation in a water tank using planar laser-induced fluorescence. Dye is injected from a circular nozzle on the left, and curls up into a vortex ring. The vortex ring will detach and move to the right. Right: Velocity field and boundaries of a vortex ring. The arrows show the instantaneous velocity. The red line shows the leading-edge outer boundary of the vortex ring in the form of a strong Lagrangian coherent structure (LCS). Adapted from Shadden et al. [87], with permission from AIP Publishing.

Vortex flow has also been suggested to benefit ventricular function through preservation of kinetic energy; however, vortex cores act as energy 'sinks'. Once a particle (e.g. a red blood cell) enters a vortex, it will stay there until the vortex breaks down into small-scale eddies that lose their energy due to viscous interaction [85]. The gradual transfer from kinetic energy, via turbulence, into heat is process is known as the *vortical cascade mechanism* [93] or *turbulence cascade* [95, Chap. 4] and is a central aspect of flow. Indeed, the rotational kinetic energy captured in small-scale eddies cannot be reconverted into kinetic energy with a uniform, macroscopic flow direction [95, p. 219]. This aspect of vortical flow implies that vortex rings also contribute to mixing of the ventricular blood, which may prevent blood clot formation [96, 97]. Mixing is increased when the inflow velocity follows a trapezoidal pattern over time [98], not unlike the E-wave in the human heart.

The temporal and spatial development of vortex rings is a highly stable and predictable process that is governed by the starting conditions [85, 86]. The most important factor in determining vortex ring dynamics is the dimensionless **vortex formation ratio** (VFR), which is the ratio of the amount of inflowing fluid L and the diameter of the orifice D [97, 99–101]:

$$\mathrm{VFR} = \frac{L}{D} \tag{1.7}$$

This ratio limits the amount of fluid that can be incorporated into the vortex ring; under conditions with VFR $\gtrapprox 4$, the vortex ring is trailed by a turbulent jet which contains the surplus volume of fluid (see Fig. 1.9) [102]. The limiting VFR arises from the inability of the vortex ring to further increase its circulation after reaching a critical point [94]. Vortex formation is also slightly influenced by variations in orifice geometry and flow velocity profiles.

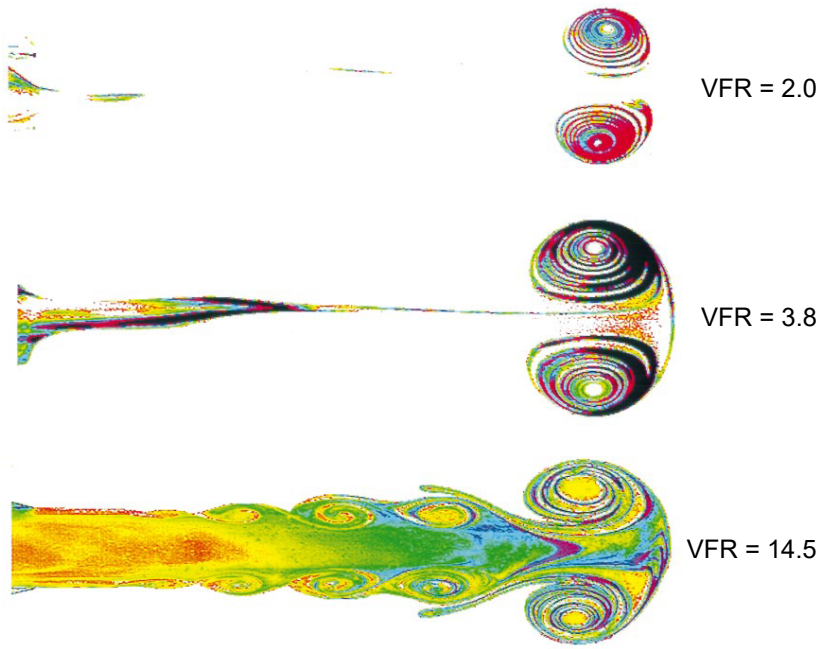

Figure 1.9: Visualization of vortex rings generated by fluid injection from a nozzle to the left, at different vortex formation ratios (VFR). When VFR $\gtrapprox 4$, the vortex ring cannot increase its circulation any further and is trailed by a turbulent jet. Reprinted from Gharib et al. [94] with permission from Cambridge University Press.

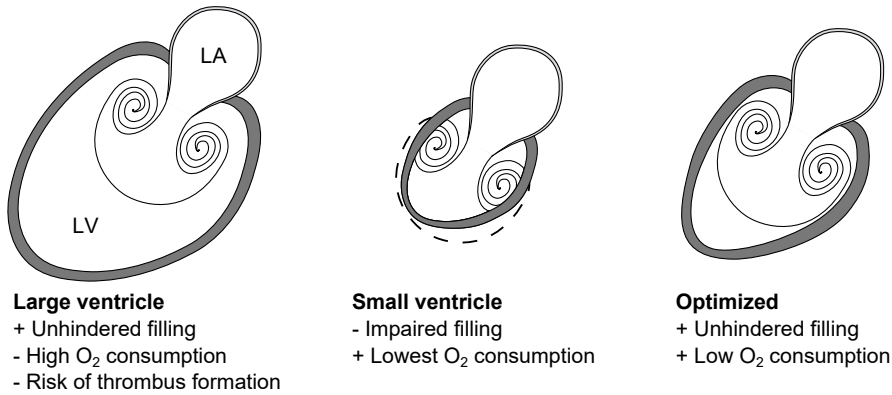

Figure 1.10: Different anatomical conditions and their effects on vortex ring formation. Left: A large ventricle will allow unhindered expansion of the vortex ring, but will waste energy due to high wall tension, and will increase the risk of thrombus formation. Center: A very small ventricle will limit vortex ring formation, possibly resulting in impaired filling. While O_2 consumption will be low, stroke volumes will also be low, requiring increased heart rate to sustain an adequate cardiac output. Right: Optimizing the relationship between vortex ring and ventricular dynamics enables unhindered filling while maintaining low wall tension, and avoids thrombus formation by continuous rinsing of the endocardium.

The outer edges of the vortex ring can be understood as a shear layer, that recurs with very similar properties as long as L and D remain unchanged. Since shear forces are known to interact with endothelial cells and induce remodeling, vortex ring formation could potentially be a factor in determining the dimensions of the ventricle. As a starting point, consider a ventricle that is large enough so as to allow uninterrupted vortex ring formation. While a large ventricle will be able to accommodate the formation of a vortex ring and hence allow for efficient filling, large ventricles have high wall tension and high oxygen consumption.[3] This arrangement is not optimal since it puts unnecessarily high demands on the myocardium. Decreasing the ventricular dimensions approaches a situation where the endocardial borders start to impinge on the vortex ring, risking impaired filling. Since the dimension of the vortex ring is given by the required amount of filling L (in turn determined by the metabolic state of the body, as filling is secondary to sustaining the appropriate cardiac output) and its relationship to the mitral valve D, the optimal dimensions for a given ventricle could therefore be the smallest that allow unhindered formation of the vortex (Fig. 1.10).

Refining the model, it is conceivable that the optimal ventricle could be slightly too small for full vortex formation at rest, since exercise causes ventricular dimensions to increase (Fig. 1.6) and the savings in O_2 consumption could outweigh a slightly decreased filling efficiency at rest. This would imply a vortex formation 'reserve' that could be recruited to optimize filling during exercise. Such an optimization would be manifested in a

[3]This follows from the law of Laplace, which states that oxygen consumption is proportional to the product of intraventricular pressure and radius.

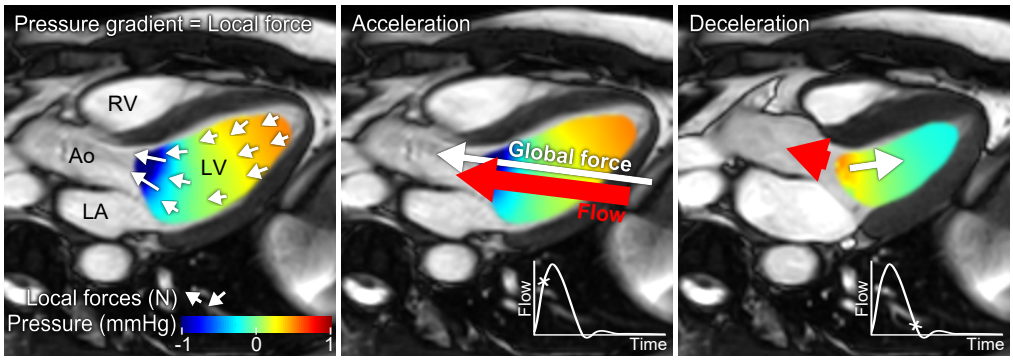

Figure 1.11: Relationship between relative pressure differences, the global hemodynamic force vector, and flow. Relative pressure differences are local gradients, equivalent to forces between neighboring points (small arrows). Adding together the local forces produces the global hemodynamic force for the ventricular blood pool. Depending on the direction of the force in relation to the motion of the blood, it can accelerate (middle) or decelerate blood (right panel).

small average distance between the outer boundary of the vortex ring and the endocardium, and should be expected to be present in all healthy hearts regarding of absolute dimensions. The purpose of **Study II** was therefore to investigate the proposed relationship between the vortex ring dimensions and the endocardial border.

1.1.11 Hemodynamic forces

As discussed above, the transit of blood through the heart entails several directional changes over the course of the cardiac cycle, each of which is caused by forces that are exchanged between the blood and myocardium. These forces can be measured as point-to-point variations in pressure, i.e. **intraventricular pressure gradients** (IVPGs) [23, 103, 104]. While it is possible to calculate IVPGs by noninvasive imaging methods such as computed tomography, ultrasound, or phase-contrast MRI [105–111], the complexity of the resulting measurements presents a significant obstacle for interpretation.

Alternatively, the intraventricular pressure field can be integrated over the ventricular volume to produce the instantaneous **hemodynamic force** vector [112] (Fig. 1.11). As this vector represents the global net exchange of forces between the blood and myocardium, it is likely to reflect the functional status of the heart. Since the left and right ventricles differ significantly in their mode of action [33], hemodynamic forces and their evolution over time can be expected to reveal new aspects on the physiology of ventricular pumping. While a number of studies have implicated hemodynamic forces as possible driving forces for cardiogenesis and cardiac remodeling [113], investigations of *in vivo* forces in the human heart have been limited to the left ventricle and/or two-dimensional measurements [111, 112, 114, 115]. **Study III** was therefore designed to explore biventricular hemodynamic forces in a wide range of cardiac dimensions.

Hemodynamic forces in left ventricular dyssynchrony

If the electrical conduction system should become damaged (e.g. due to myocardial infarction), propagation of the depolarization front will occur via the gap junctions between ordinary myocytes, which is a much slower process. If the left branch is impaired, a **left bundle branch block** (LBBB) will result, and the ability of the ventricle to contract synchronously may become impaired. In patients with heart failure, LBBB with resulting LV dyssynchrony will potentially derange left ventricular function further, and contribute to disease progression. These patients can potentially benefit from **cardiac resynchronization therapy** (CRT) [116, 117], which entails implantation of a dual-lead pacemaker device. One lead is typically placed in the apical part of the RV, where it can sense the early part of ventricular depolarization, and the other lead is positioned in the part of the LV myocardium that depolarizes last. While the idea seems simple, and mechanistically sound, almost 1/3 of patients show no improvement after CRT commencement, meaning that many devices are implanted in vain [118, 119].

Studies have shown that treatment is somewhat more likely to succeed in female patients with no prior myocardial infarction, no obesity, QRS duration $\geq$150 ms, and LBBB (odds ratio 1.47-2.05 for the mentioned factors [120]). Treatment response is also improved when using stricter criteria for LBBB [121]. In the individual patient, however, these factors are not specific enough to guide therapy considerations. It is clear that the main effect of CRT comes from reverse remodeling [122], indicating that mechanisms involved in remodeling processes are of potential value for improving treatment response.

Recent research advances in the field of epigenetics have established blood flow as a likely player in determining the shape and configuration of the developing heart [13, 123, 124]. In a study by Pedrizzetti et al., hemodynamic forces were suggested to influence cardiac remodeling in disease conditions such as dyssynchrony [114]. In a follow-up study, it was shown that patients that respond well to CRT treatment also change the alignment of their hemodynamic forces when pacing is activated [115]. This suggests that hemodynamic forces may single out patients that are most likely to respond well to CRT intervention. The studies used particle-imaging velocimetry by echocardiography, and only considered forces in one plane. A three-dimensional approach could possibly provide additional information on the mechanics of the failing ventricle, and improve the predictive power of hemodynamic force patterns for treatment response. **Study IV** was therefore designed to study left ventricular hemodynamic forces in a cohort of patients with heart failure and LV dyssynchrony.

1.2 Magnetic resonance imaging

This section serves to introduce the reader to the general principles of **magnetic resonance imaging** (MRI) and its application for *in vivo* flow measurements. The anatomy of a modern MR scanner is shown in Fig. 1.12.

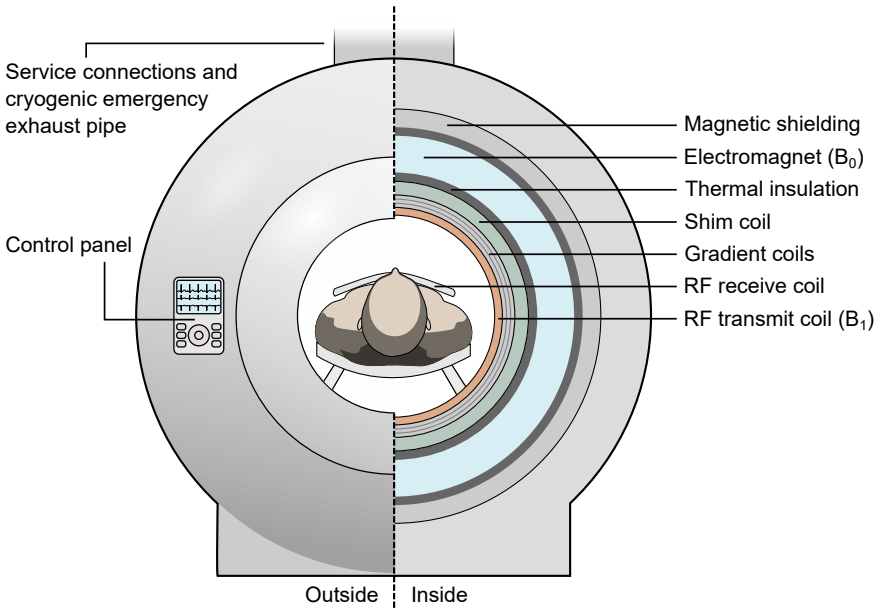

Figure 1.12: Cross-section of MR scanner. The main magnetic field B_0 is provided by a helium-cooled superconducting electromagnet. The field is manipulated using the three gradient coils, which apply additional, weaker magnetic fields in the x, y, and z directions. The shim coil is used to homogenize the magnetic field in the area of interest. Energy is added to the patient by applying a radiofrequency (RF) field called B_1, which resonates with the spins in the patient if the correct frequency is used (Larmor frequency). The application of gradients and RF fields is controlled by an array of computers located in a neighboring room. The MR signal is collected by receiver coils positioned on or near the patient.

Figure 1.13: The first proton nuclear magnetic resonance zeugmatogram, i.e. MRI picture by Lauterbur [128], depicting a transversal slice through two test tubes containing water. Reproduced with permission from Nature Publishing Group.

The phenomenon known as **nuclear magnetic resonance** (NMR) was first described in 1938 by Isidor Rabi, who studied the radiofrequency absorption spectrum of lithium chloride in a vacuum [125]. In 1945, independent of each other, Felix Bloch and Edward Purcell demonstrated the NMR phenomenon in solid matter [126, 127]. Rabi, Purcell, and Bloch would later be awarded the Nobel Prize for their discoveries. Nuclear magnetic resonance became a means for analysis of chemical constituents in solutions (nuclear magnetic spectroscopy). Paul Lauterbur modified the technique by adding spatial encoding gradients in order to generate images of the sample [see 128, also Fig. 1.13], and further refinements were made by Peter Mansfield in the form of slice selection gradients and rapid imaging. The two would share the Nobel Prize in 2003 for their discoveries. Magnetic resonance imaging (initially called *magnetic resonance zeugmatography*) developed into an invaluable tool for clinicians and researchers. Magnetic resonance image contrast comes from careful manipulation of the inherent magnetic properties of proton nuclei. In medical imaging, the most common nucleus used for imaging is that of hydrogen (protons).

1.2.1 Generation of MR signal

Hydrogen nuclei possess a property called **spin**. Spin gives the protons a magnetic moment, and we can therefore think of protons as tiny magnets. These magnets, somewhat confusingly, are also referred to as 'spins' (Fig. 1.14). When spins are introduced to an external magnetic field B_0, two things will happen.

First, the magnetic moment of all spins interact with the B_0, which generates torque. Spins will therefore begin to **precess** about the axis of the B_0. Precession is a gyroscopic

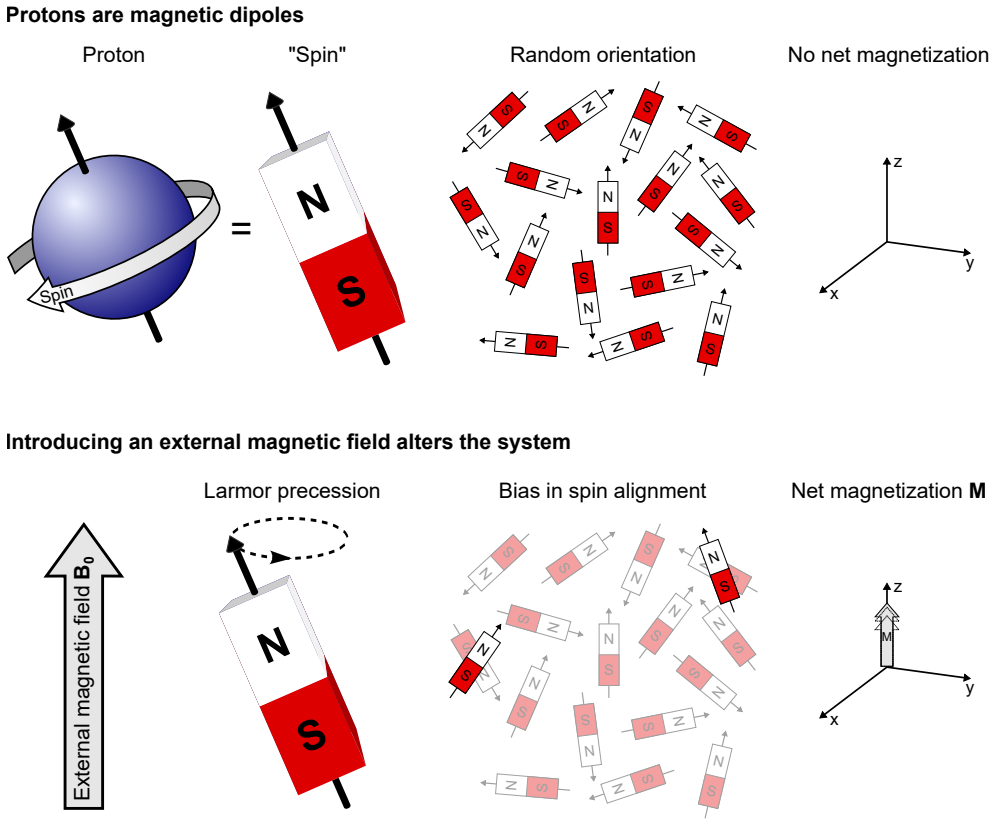

Figure 1.14: In the absence of an external field, spins will be randomly arranged, cancel out, and the resulting net magnetization vector is zero. If we introduce an external magnetic field, called B_0, two things will happen. First, the individual spins will start to precess about the external field. The spins will also gradually develop a tendency to align themselves parallel to the external field, shown here as a shift in the orientation of two spins. The parallel alignment is a low-energy state and is slightly favored over other alignments, resulting in a net magnetization called M. This net magnetization vector can be manipulated using RF pulses to produce image contrast. For illustration purposes, M has been exaggerated. The relationship between M and the total number of spins depends on both B_0 strength and sample temperature; at 1.5T it is approximately $1/10^6$.

type of motion, like that of a spinning top. Precession occurs at the Larmor frequency ω,

$$\omega = \gamma \cdot B, \tag{1.8}$$

where B is the local magnetic field strength and γ is the gyromagnetic ratio. The gyromagnetic ratio for hydrogen is approximately 42.6 MHz/T, meaning that precession occurs at a frequency of about 64 MHz in a common 1.5T MR scanner. At this point, the direction of the individual spin is randomly distributed in space, and the phase of the precession is also different between spins.

Secondly, spins will interact with the B_0 field and gradually settle into a new thermal equilibrium with a bias towards alignment with the field. Being aligned with the field is a low-energy state that causes a net magnetization vector M to take form. The existence of M is a prerequisite for MR imaging and its magnitude is dependent on field strength; increased M provides more signal, which is the main reason for using high field strength.

At this point, M is the net surplus of magnetization along B_0. It is made up of the sum of precessing spins, and as such can be understood as an average of their instantaneous directions in space. The precessional phase is still random, and the oscillatory phase ϕ of the spins will therefore cancel out. As long as this is true, M will have no xy component. Even though the individual spins will randomly exchange energy with one another, and alter their phase and alignment, M remains stable until the system is further disturbed. Since M is much smaller than B_0, it is not measurable while it remains aligned with the z axis. If the spins could somehow be forced to leave the z axis, M would gain an xy component and thus create an oscillating magnetic field with the same frequency as the individual spins. Oscillating magnetic fields can induce currents in coils, enabling collection of signal from M.

We can solve the problem by invoking magnetic resonance. Recall that spins have a tendency to precess about all external magnetic fields. By applying a radiofrequency pulse (RF, essentially an electromagnetic field called B_1) that is orthogonal to B_0 and is oscillating at the Larmor frequency, the spins will 'see' B_1 as an added static magnetic field and hence precess about both fields at the same time. Since B_1 is typically much weaker than B_0, the Larmor frequency about B_1 is much smaller, and the effect of B_1 on spins is difficult to tease out from the much faster precession about B_0. In order for us to visualize the behavior of the spins due to the influence of the newly added RF field, we will therefore change perspective. Until now, we have regarded the spins in the **laboratory frame of reference**, where B_0 is visible and the spins precess about that field with the frequency ω_0, i.e. 64 MHz at 1.5T. Now, we will observe the spins from within the **rotating frame of reference** instead, meaning that we 'hop on' to one of the spins that is precessing at the Larmor frequency. We no longer see B_0, which allows us to look at the relationship between individual spins, and see the effect of the added B_1 field.

As B_1 is added along the x axis, M will start to precess about B_1 with the frequency ω_1 for as long as it is active (while RF transmission is ongoing). As a result, M gradually diverts from its original longitudinal alignment along B_0 as it 'flips' from the z axis down to

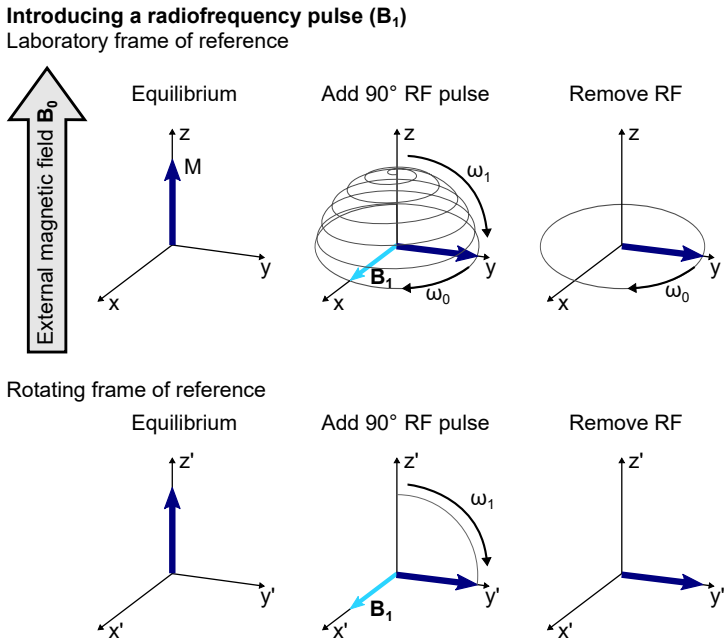

Figure 1.15: At thermal equilibrium, the xy component of M is not visible because spins are out of phase. When an RF pulse is applied perpendicular to the B_0, spins will precess about both fields at the same time, with frequency ω_0 for B_0 and ω_1 for B_1. When viewed in the laboratory frame of reference, we see both effects at once – while the RF is active, M follows a 'beehive' trajectory towards the xy plane. Note that the spins acquire the same phase when the RF plays out. If we turn off the RF transmitter when M reaches the transverse plane, M will revert to precessing about only the B_0 (z axis), now with an xy component since spins are in phase. In the rotating frame of reference, B_0 and its effects are no longer visible to us, so when B_1 is active we see its effect ω_1 on M as a rotation in the yz plane.

the xy (also called transverse) plane. The amount of flipping depends on the amount of RF energy delivered, and is called the **flip angle** (often abbreviated α). Since we can only see M while it is aligned with the transvere plane, using larger α will generate a larger signal later on. A flip angle $\alpha = 90°$ means that M is completely flipped onto the transverse plane so that no z component remains. This is called a **saturation pulse** and provides the most signal; however, using high α requires more RF energy deposition and takes longer time. In some circumstances, for example in fast imaging, it can therefore be preferable to use a lower flip angle.

If the spins would be on the xy plane but remain out of phase with each other, the signal would still cancel out. However, an added effect of B_1 is that it forces the spins into the same phase. Since the phases within the spin population no longer cancel out, M now gains an xy component. The effects of adding the RF pulse B_1 is shown in Fig. 1.15, in both frames of reference.

After termination of the RF pulse, the spins will slowly tend to revert to their low-energy

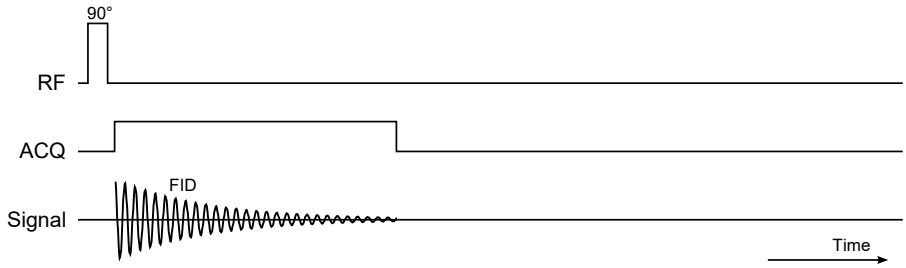

Figure 1.16: The one-pulse MR experiment is initiated by applying an RF pulse with sufficient amplitude and duration to flip the magnetization vector M by 90°, onto the transversal plane. This is immediately followed by turning on the signal acquisition (ACQ), which picks up an exponentially decaying alternating current which oscillates at the Larmor frequency. This signal loss occurs due to T2* dephasing of the spins and is called the free induction decay (FID).

state. They do so by means of two independent processes : **T1** (*spin-lattice*) relaxation, and **T2** (*spin-spin*) relaxation. T1 relaxation describes the recovery of M along the z axis. It results from the transfer of thermal energy from the spins to the lattice, the molecular surroundings of the spins. T2 relaxation is the loss of signal in the transverse plane due to interactions between neighboring spins. This 'crosstalk' leads to dephasing, loss of transverse magnetization, which is the effect of T2. In reality, dephasing occurs faster than T2 would suggest, as it is further compounded by inhomogeneities in the B_0 field strength, so that transverse signal decay occurs faster than it would under perfectly homogenous conditions. This is called **T2*** relaxation and is always faster than T2.

1.2.2 The one-pulse MR experiment

The most basic experiment in magnetic resonance is probably the one-pulse experiment and is visualized in Fig. 1.16. At the beginning of the experiment, an RF pulse is played out using the RF transmit coil. The RF pulse is tuned to the Larmor frequency and adds energy to the system of spins. This causes M to flip onto the transversal plane. It immediately starts to dephase due to T2* relaxation, and the surplus energy added by the RF pulse is dispersed to the surrounding spins. If we position a sensitive receiver coil nearby, and tune it to the Larmor frequency, it will pick up a brief signal emanating from the sample. This signal is called the **free induction decay** (FID) and can be understood as a faint **echo** of the RF energy that was originally transferred to the system. We have created an energy echo from the entire population of spins inside the scanner.

Unfortunately, it is not possible at this point to deduce any information regarding the spatial origins of the signal. As all spins are precessing at the same frequency regardless of their location in the body, the RF pulse will excite every spin and the resulting signal will similarly originate from everywhere at once. In order to create an image, it is therefore necessary to encode spatial information into the spins.

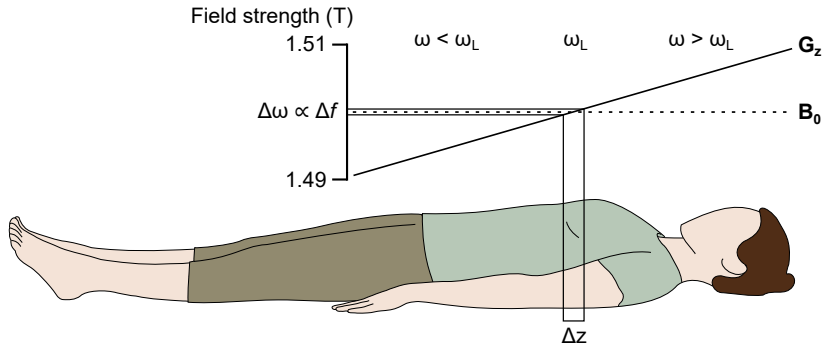

Figure 1.17: Slice selection is carried out by playing out a gradient G_z during RF excitation. This alters the strength of the magnetic field, causing changes in the precessional frequency ω of individual spins. By limiting the bandwidth of the RF pulse to a narrow range Δf corresponding to the range of precessional frequencies $\Delta\omega$ in the area of interest (Δz, e.g. the heart), only spins within that range will be excited. Slice selection can be performed in any orientation by using all three gradients simultaneously.

1.2.3 Spatial encoding

In MR imaging, spatial encoding is performed in three directions x, y, z, making it a true 3D imaging method. Typically, encoding is performed in three discrete steps: slice selection (selective RF excitation), frequency encoding, and phase encoding.

Slice selection

Spatial encoding can be achieved by using combinations of magnetic field gradients, both during RF excitation, and while recording the echo. Since RF excites all spins that are on-resonance, the first step is to add a gradient along the z axis while playing out the RF pulse. This will cause the B_0 magnetic field to vary in strength as a function of distance along the z axis. The result is an increase the precessional frequency of all spins that are found towards one end of the scanner, and a similar decrease in frequency for spins on the other end. In the middle is an area of unaltered field strength, that retains the B_0 Larmor frequency. Playing out the RF pulse while the gradient is active will only excite spins that are found within a range of frequencies. The process of selectively exciting a slab of spins using gradient is called **slice selection** and the corresponding gradient is here called G_z, since it is applied in the z direction. The slice thickness Δz is affected by two factors: the strength of the G_z gradient, and the bandwidth of the RF pulse Δf,

$$\Delta z = \frac{\Delta f}{\gamma G_z}. \tag{1.9}$$

Slice selection is summarized in Fig. 1.17.[4]

[4]For completeness, it should be noted that slice selection can be carried out in any three-dimensional orientation using x, y and z gradients at the same time.

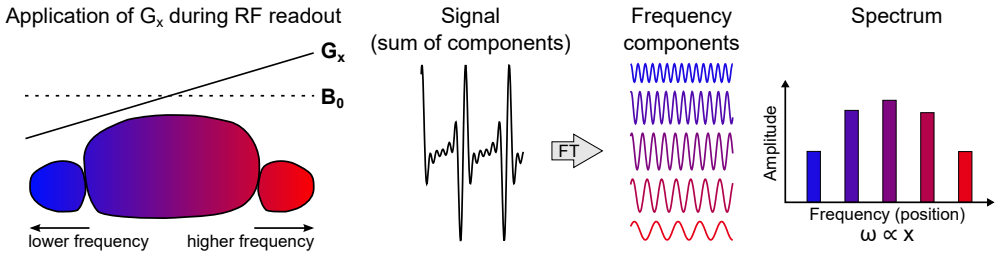

Figure 1.18: Frequency encoding is performed by applying a gradient G_x during RF readout. This has the effect of separating spins within the excited slice, thus creating a complex echo that is made up of many different frequency components that correspond to different positions along the x axis. Using the Fourier transform, the complex echo can be separated into its frequency components, thus rendering a spectrum of the signal intensities.

Frequency encoding

While we have now limited the origin of the MR signal in one dimension by slice-selective RF excitation, we have yet to differentiate the signal within that slice. The next step is to apply a gradient G_x perpendicular to the slice selection while reading out the signal. The process is called frequency encoding and is summarized in Fig. 1.18. Similar to G_z, which was applied during RF excitation, G_x will change the local field strength and so alter the Larmor frequency of individual spins as a function of their location along the x axis. Recording the echo while the G_x is active now produces a complex waveform which is the result of multiple frequencies in superposition. The individual components of this complex signal are possible to extract using the Fourier transform, which computes a spectrum of frequencies from the signal. Since ω is proportional to the local field strength, the frequency spectrum shows the signal intensity arising from different locations along the x axis. Note that while G_x actually creates a smooth gradient with an infinite number of possible frequencies, the MR scanner digitizes this signal into spatial steps. The resolution with which this process happens is therefore limited by the sampling rate of the analog-to-digital converter that is used to record the echo, and defines the spatial resolution of the resulting image.

Phase encoding

We have now located the spins along the x axis (due to frequency encoding while performing the readout), and along the z axis (by slice-selective RF excitation). The remaining challenge is to locate the spins along the y axis, which can be achieved by phase encoding using another gradient, G_y. The introduction of G_y familiarly causes spins to change ω. At higher field, ω is higher, so a spin that spends a certain amount of time in that field will accumulate a phase difference compared to spins that are in a lower field. Therefore, the accumulated phase difference $\Delta\phi$ is a function of the local field strength and the time spent at that strength. After G_y is turned off, the frequency of the spins will revert to ω_0, but the

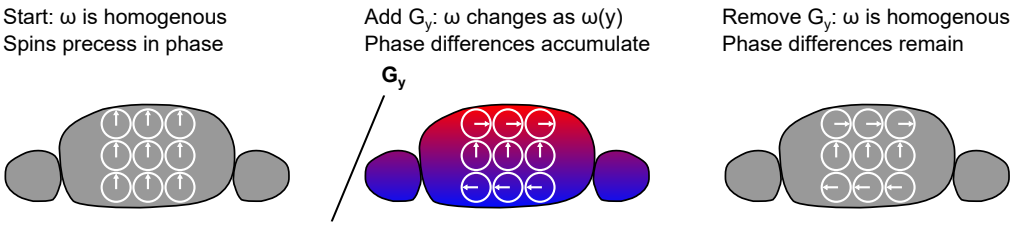

Figure 1.19: Phase encoding is used to localize spins in the y direction. The brief addition of a gradient G_y causes an accumulation of phase differences. G_y is turned off before signal readout to avoid interfering with frequency encoding, but the accumulated phase differences remain. The phase information can be extracted using a quadrature coil.

accumulated phase will be carried forward. To generate an image, the imaging experiment is repeated several times, using different strength of the phase encoding gradient for each iteration. Phase encoding is summarized in Fig. 1.19. We have now generated a complex signal that contains both frequency and phase information. Both parts of the signal can be sampled using specially designed **quadrature coils**, and analyzed separately, which allows us to use the frequency information to localize the spins in the x axis and the phase for the y axis. If the experiment is repeated multiple times, the resulting data can be structured in an array and treated using a 2-dimensional Fourier transform to generate an image.

The combination of a single slice-selective RF excitation and gradient-driven creation of an echo is called **gradient echo** (GRE) imaging. Gradient echo imaging is fast but technically challenging. The GRE signal arises from the FID which decays rapidly due to T2* relaxation. The sequence is therefore sensitive to factors which disturb the B_0, and it is important to keep the time from RF excitation to signal readout (the **echo time**) to a minimum. Some additional details that are required to make a good GRE image are shown in Fig. 1.20. Gradient echo imaging forms the basis for the flow measurements used in Papers I-IV.

1.2.4 Cardiac MRI

Performing MRI of the cardiovascular system, or more specifically, of the beating heart, poses a set of specific challenges that need to be addressed in order to generate acceptable image quality. The most important challenge is that of motion, which is caused by the pumping action of the heart as well as the breathing motion of the diaphragm and thoracic wall.

Image gating

MR imaging of the heart is made possible by synchronizing the image acquisition process to a simultaneously collected ECG [129]. The ECG R-waves are used to define the start of each new cardiac cycle. Sorting of images can be carried out either prospectively,

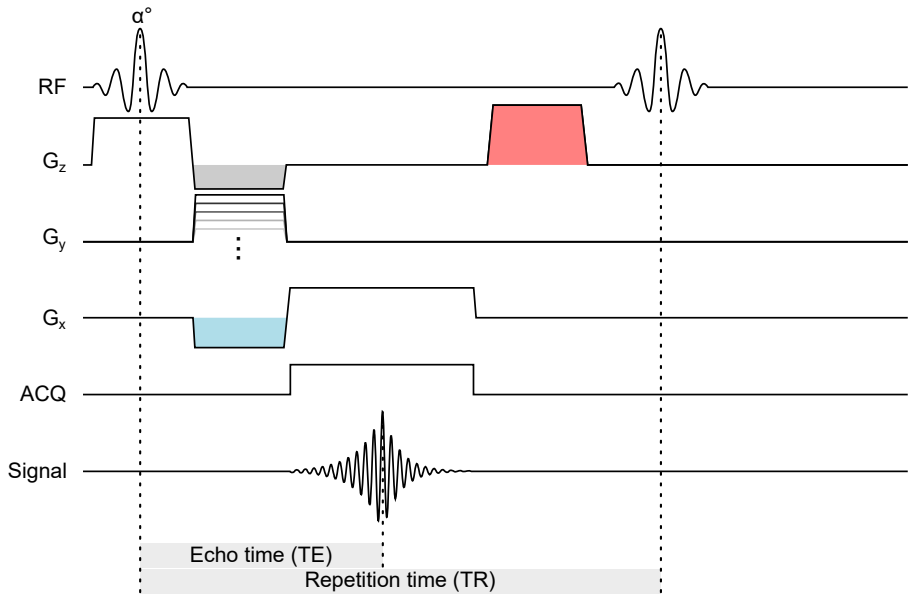

Figure 1.20: Pulse sequence diagram showing a typical gradient echo sequence. The gradient echo is created by refocusing the MR signal by application of gradients. For each repetition of the pulse sequence, the phase encoding G_y is altered. Notably, the slice selection gradient has an added lobe (gray) to cancel out the accumulation of phase differences within the slice which arises from the initial positive G_z lobe. Furthermore, the frequency encoding gradient has an initial lobe (blue) designed to overcome some technical limitations related to signal acquisition. The time from RF excitation to the peak of the echo is called the echo time (TE). To produce an image, the GRE experiment must be repeated multiple times with different phase encoding; the time between RF excitations is called the repetition time (TR). Preceding the next RF pulse is a spoiler gradient (red) that is designed to destroy residual magnetization in the transverse plane, which enables faster imaging. The sequence is therefore called a *spoiled* gradient echo.

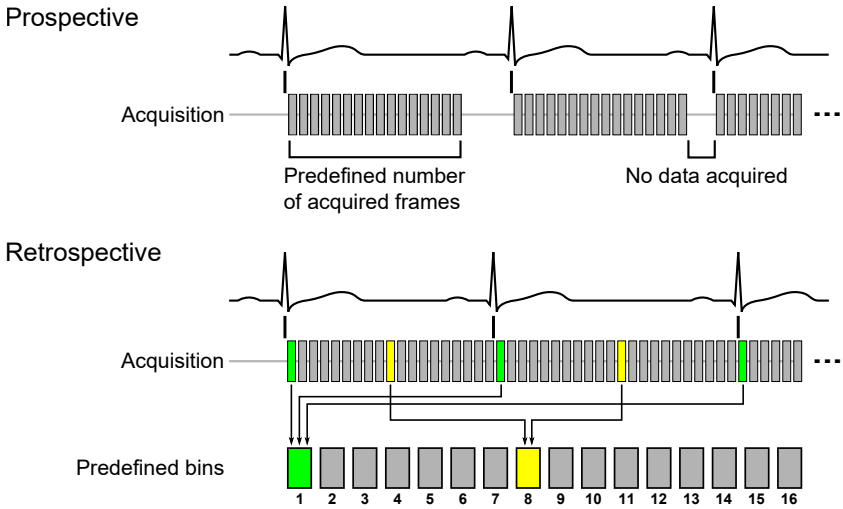

Figure 1.21: Methods for ECG gating. Prospective gating is used in when full coverage of the cardiac cycle is not needed, or when imaging should only performed during a specific time (e.g. diastasis). Retrospective gating is performed when the entire cardiac cycle should be visualized. Image acquisition is continuous and sampled images are sorted into predefined bins.

meaning that the acquisition process is restarted each time an R-wave is detected, or retrospectively, where images are continuously sampled and sorted afterwards according to their relative position in the cardiac cycle (Fig. 1.21). Retrospective gating is commonly used for time-resolved imaging where coverage of the entire cardiac cycle is desirable. Respiratory motion is an important issue when using lengthy sequences. For short imaging sequences (<20 seconds), it is often possible to carry out imaging during breath-hold. Respiration causes the diaphragm to move within the thoracic space, which potentially shifts the heart several centimeters, primarily along the z axis. This information can be used to sort images according to their position in the respiratory cycle [130], either to maximize image quality by minimizing motion blur, or to investigate respiration-dependent changes in physiology [131]. One common approach is to use a bellows placed on the upper part of the abdomen to measure changes in pressure, which corresponds to the respiratory motion. It is also possible to use information from the images, for example by taking intermittent snapshots of the position of the diaphragm, and then accepting or discarding images based on their place in the respiratory cycle (Fig. 1.22). The importance of using respiratory compensation during long acquisitions has been called into question. For certain applications, and under certain conditions respiratory gating seems to make little difference [132]. While these conclusions have been criticized based on theoretical considerations of the effect of respiratory compensation [133], it seems possible that the modest added value of respiratory compensation in some real-world applications is due to limitations arising from other factors (e.g. gross body motion, introduction of artifacts due to disturbance of imaging

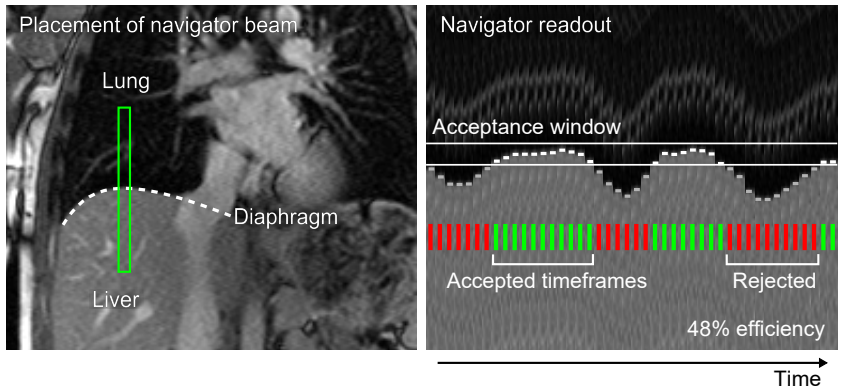

Figure 1.22: Respiratory gating using navigator echoes. A specialized navigator pulse is played out with regular intervals, which provides a one-dimensional readout of the liver-diaphragm border. By automatically tracking the border, images that are acquired within a pre-specified acceptance window are saved; the rest are discarded.

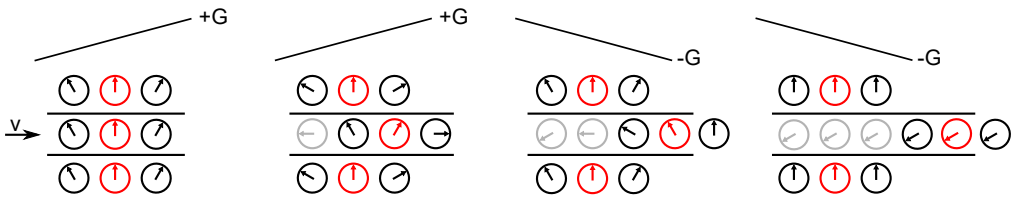

Figure 1.23: The principle of phase-contrast imaging. Spins in the middle row are moving towards the right with velocity v. Spins starting in the middle column are shown in red. A gradient $+G$ is applied, which causes spins to accumulate phase ϕ as a function of the field G they experience and the time spent at that field. After a time t, the gradient is reversed and $-G$ is activated, also with duration t. Moving spins will accumulate phase differently than stationary spins (top and bottom rows). An additional readout is performed without the bipolar gradient pair to compensate for the phase background that results from B_0 inhomogeneieties.

steady state). Using respiratory gating also prolongs image acquisition, which means that data will be sampled at more diverse physiological states.

1.2.5 Flow measurements using phase contrast

Until now, we have only discussed images formed by quantifying the net magnetization M at different points in space and time, and the phase ϕ has been used only for spatial localization of the MR signal. The most commonly used principle of measuring blood flow using MRI is that of **phase contrast**. The concept of using phase information to measure motion was proposed by Hahn in 1960 [134], and its implementation for quantitative *in vivo* flow measurements was developed by Moran in 1982 [135]. The principle is illustrated in Fig. 1.23. By introducing an additional pair of **bipolar** gradient lobes in one direction, it is possible to encode velocity information as accumulated phase along the axis of that gradient. The bipolar gradient encodes velocity information in the accumulation of phase

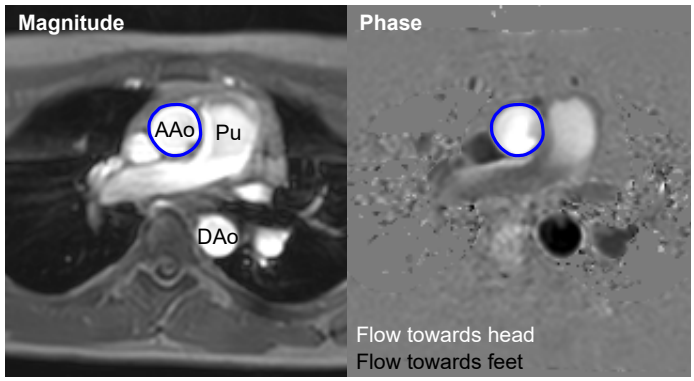

Figure 1.24: Throughplane flow measurement. The slice is transversally oriented and positioned in the thorax just above the aortic root. The magnitude image (left) shows the ascending aorta (AAo, delineated in blue), pulmonary trunk (Pu) and descending aorta (DAo). The right panel shows the corresponding phase-contrast image. Here, the pixel intensity value is linearly coupled to the speed through the plane. The instantaneous flow rate is calculated as the product of the delineated vessel area and the average speed.

ϕ [136]:

$$\phi = \int \gamma G(t) x(t) dt, \tag{1.10}$$

where ϕ is the accumulated phase shift, $G(t)$ the gradient amplitude at time t, and $x(t)$ the position of the excited spin at time t. Phase will also accumulate from B_0 inhomogeneieties [134]. To avoid introducing these spurious phase offsets, a **reference** image is also sampled with the same spatial location but without the bipolar gradient. A background compensated phase contrast image is then calculated from the difference between the two images.

The most commonly used phase contrast imaging strategy is single-directional. Velocity information can be encoded in any direction (slice, phase, or frequency encoding direction). Velocity is often encoded in the slice direction as it enables shorter echo times (velocity encoding can be played out simultaneously as the slice select pulse) and also enables quantification of volume flow [137]. This approach is called **throughplane flow** and is shown in Fig. 1.24.

1.2.6 Four-dimensional flow measurement

If the flow-sensitive experiment is carried out with velocity encoding in all three orthogonal directions, it is possible to calculate the speed and direction anywhere within the sampled volume. As the method combines three-dimensional velocity information with temporal information, it is commonly called **four-dimensional phase contrast imaging** or 4D flow. The method was first proposed by Pelc et al. in 1991 [138] as a new way of obtaining angiographic images. Wigström et al. implemented a retrospectively gated 4D flow approach that is still the most commonly used approach today [139]. 4D flow has seen a remarkable

growth in applications and the technique has been used to quantify diverse phenomena in the cardiovascular system. Examples include intracardiac flow patterns [80, 140–144], aortic flow patterns and relative pressure differences [107, 108, 110, 145], turbulence intensity [146, 147], kinetic energy [83, 132, 141, 148], and vortex ring formation [99, 149].

The main strength of 4D flow imaging is that it allows relatively comprehensive quantification of three-dimensional and complex blood flow patterns. The main drawback of the technique is the inherently long acquisition times, which arise from the large amount of data gathered. To keep acquisiton times within reasonable limits, compromises are often made in spatial and temporal resolution, which imposes some limits on the technique's ability to depict fast and/or small events [101]. Imaging can be performed faster by utilizing different acceleration techniques and enhanced readout strategies, although such compromises tend to decrease the accuracy of the measurements (see for example [150]) or introduce artifacts. When interpreting results from 4D flow studies, it is important to bear in mind that the data has been acquired over a relatively long time (for whole-heart 4D flow, typically well over 10 minutes) and as such it represents an average measure of the blood flow. Beat-to-beat variations in flow are cancelled out and only large-scale flow features are properly represented in the data.

Chapter 2

Aims

The overarching purpose of this thesis was to utilize 4D flow magnetic resonance imaging to quantify intracardiac flow patterns. The specific aims of the different papers were as follows:

Paper I

To quantify the kinetic energy of the blood within the atria of the human heart and investigate its potential role for energy conservation in cardiac pumping.

Paper II

To quantify the dynamic relationship between the vortex ring boundary and left ventricular endocardium throughout diastole, to investigate the proposed adaptation of the left ventricle to vortex ring dimensions.

Paper III

To quantify biventricular hemodynamic forces over the entire cardiac cycle in a wide size range of healthy hearts, to uncover their mechanistic role in biventricular cardiac pumping.

Paper IV

To quantify left ventricular hemodynamic forces in a cohort of heart failure patients with varying degrees of LV dyssynchrony, in order to investigate how the physiology and mechanics of intraventricular flow in dyssynchronous ventricles differ from normal.

Chapter 3

Materials and methods

He gazed about him, and the very intensity of his desire to take in the new world at a glance defeated itself. He saw nothing but colours — colours that refused to form themselves into things. Moreover, he knew nothing yet well enough to see it: you cannot see things till you know roughly what they are.

C S Lewis, *Out of the Silent Planet*

3.1 Study population

All studies in this thesis were subjected to review by the local Ethical Review Committee at Lund University. Written informed consent was obtained from all study participants. Studies were designed to comply with the Helsinki declaration.

There was a considerable overlap in populations between the different studies, summarized in Tables 3.1 and 3.2. More detailed population data is available in the different papers, attached at the end. Studies were performed on three groups of volunteers: healthy controls, elite athletes, and patients with heart failure.

3.1.1 Controls and athletes

Controls were enrolled in the study after meeting the following criteria: no history of cardiovascular or systemic disease, free from medication, normal ECG, and resting blood pressure $\leq$ 140/90 mmHg. Elite endurance athletes were also included; apart from meeting the same criteria for health as the controls, they also underwent exercise testing with respiratory gas analysis to confirm their fitness status [151].

3.1.2 Heart failure patients

Heart failure patients were recruited from the CRT-CLINIC study (30 patients) or were offered to participate after clinical referral due to worsening heart failure symptoms (2 pa-

ID	Study I	Study II	Study III	Study IV
C01	+	+	+	+
C02	+	+	+	+
C03	+	+	+	+
C04	+	+	+	+
C05	+	+	+	+
C06	+	+	+	+
C07	+	+	+	+
C08	+	+	+	+
C09	+	+	+	+
C10	+	+	+	+
C11	+		+	+
C12	+		+	+
C13	+		+	+
C14	+		+	+
C15	+		+	+
C16		+	+	+
C17		+	+	+
C18		+	+	+
C19			+	+
C20			+	+
C21			+	+
C22			+	+
C23			+	+
C24			+	+
C25			+	+
A01		+	+	+
A02		+	+	+
A03		+	+	+
A04			+	+
A05			+	+
A06			+	+
A07			+	+
A08			+	+
A09			+	+
A10			+	+
A11			+	+
A12			+	+
A13			+	+
A14			+	+

Table 3.1: Overlap in study participation among controls (Cxx) and athletes (Axx).

ID	Study I	Study II	Study III	Study IV
P01		+	+	+
P02		+	+	+
P03		+		+
P04		+		+
P05		+		+
P06		+		+
P07		+		+
P08		+		+
P09		+		+
P10		+		+
P11		+		+
P12		+		+
P13		+		+
P14		+		+
P15		+		+
P16		+		+
P17		+		+
P18		+		+
P19		+		+
P20		+		+
P21		+		+
P22		+		+
P23		+		+
P24				+
P25				+
P26				+
P27				+
P28				+
P29				+
P30				+
P31				+

Table 3.2: Overlap in study participation among patients.

tients). All patients were scheduled for CRT implantation based on having NYHA class II-IV heart failure despite optimal medical therapy, ejection fraction $\leq$35% on echocardiography, and LBBB with QRS duration $\geq$ 130 ms. MR imaging was performed before surgery. In a few cases, imaging resulted in patients being struck off the CRT waiting list as the ejection fraction was found to exceed 35%.

3.2 Magnetic resonance imaging

3.2.1 Imaging protocol

All subjects underwent MR imaging at 1.5T or 3T in Philips Achieva scanners (Philips Medical Systems, Best, The Netherlands). The imaging protocol for all subjects consisted of time-resolved balanced steady-state free precession (bSSFP) images in the two-chamber, three-chamber, four-chamber and short-axis views, as well as 4D flow which was sampled from a box covering the entire heart, and through-plane flow measurements of the great vessels for verification purposes. Balanced SSFP and 4D flow imaging was performed using retrospective image gating; bSSFP was performed during end-exspiratory breath-holds and 4D flow was acquired during free breathing.

Additionally, heart failure patients underwent late gadolinium enhancement imaging to evaluate the presence and extent of myocardial scar tissue, indicative of past ischemic injury. Late gadolinium enhancement imaging was performed using a 3D inversion recovery gradient echo sequence approximately 20 minutes after intravenous administration of 0.2 mmol/kg gadolinium-based contrast agent (Dotarem, Guerbet, Roissy, France)[152].

3.2.2 4D flow

4D flow was acquired using a retrospectively gated turbo field echo sequence which sampled a box covering the entire heart using segmentation factor of 2 and parallel imaging factor 2. The spatial resolution was 3 mm isotropic with a typical matrix size of $80 \times 80 \times 40$. The echo time was 3.7 ms and repetition time was 6.3 ms, resulting in a net temporal resolution of approximately 50 ms. 4D flow was reconstructed to 40 frames per cardiac cycle using linear interpolation. Respiratory gating was performed on the healthy controls, but not on the athletes and patients. This decision was based on experiments that demonstrated limited added value of respiratory gating for the applications described here [153]. In addition, the added scan time when using respiratory gating would severely limit the applicability of the technique for heart failure patients, who were often suffering from orthopnea and were uncomfortable lying down in the scanner bore.

Post-processing of 4D flow data was carried out using in-house developed plugins for Segment (Medviso, Lund, Sweden) [154]. Concomitant gradient terms were compensated by the scanner software, and residual phase background was corrected offline using a time-resolved first-order polynomial fit to stationary tissue. While phase background errors can be assumed to be nonlinear, the relatively sparse amount of stationary tissue avail-

able for background correction limits the usefulness of higher-order correction strategies [155]. VENC was set to 100 cm/s to provide good velocity-to-noise ratio for intracardiac flow quantification; this often resulted in some velocity aliasing in the proximal aorta, and occasionally in the left ventricular outflow tract. Phase wraps were unwrapped using a semiautomated approach [150].

4D flow images were manually co-registered with bSSFP images to facilitate visualization and quantification. The bSSFP images were manually delineated to provide time-resolved boundaries for subsequent 4D flow analyses.

3.2.3 Kinetic energy

Kinetic energy within the atrial delineations was calculated for each timeframe as follows. First, the three-dimensional velocity magnitude v was computed in each voxel:

$$v = \sqrt{v_x^2 + v_y^2 + v_z^2}. \tag{3.1}$$

The kinetic energy for each voxel was then computed as $KE = \frac{mv^2}{2}$, where m is the voxel volume multiplied with the density of blood, set to $\rho = 1.05$ kg/l [156]. The total KE within the atrial endocardial boundary was computed for each timeframe by summation of all voxels inside the delineations.

The fraction of kinetic energy involved in rotational flow structures was quantified as follows. First, the instantaneous atrial center of mass was detected automatically from the atrial delineations. Second, the angular momentum of each voxel within the atrium about the atrial center of mass was calculated using the velocity and position vectors for each voxel. Total angular momentum about the atrial center of mass was obtained by summation of all atrial voxels for each timeframe separately, and the rotational axis was determined from the center of mass and the direction of the angular momentum around it. Last, the rotational kinetic energy (RKE) about that axis was calculated as

$$\text{RKE} = \frac{mv_\alpha^2}{2}, \tag{3.2}$$

where v_α is the angular velocity component of each individual voxel. The non-rotational kinetic energy was calculated as NRKE = KE − RKE for each point in time.

The atrioventricular plane displacement (AVPD) and average AV plane velocity was measured using previously described methods [3, 35, 46].

The amount of KE added to the atrial blood by the early rapid filling was approximated as the difference between the early diastolic KE peak and a KE baseline. The baseline was calculated by fitting an exponential curve whose asymptote was zero to the downslope of the early diastolic KE peak. The resulting curve was then shifted in time so that it intersected the late systolic KE. This model thus approximates the energy decay in the system in the absence of further cardiac movement, as it originally reflects the energy decay during diastasis.

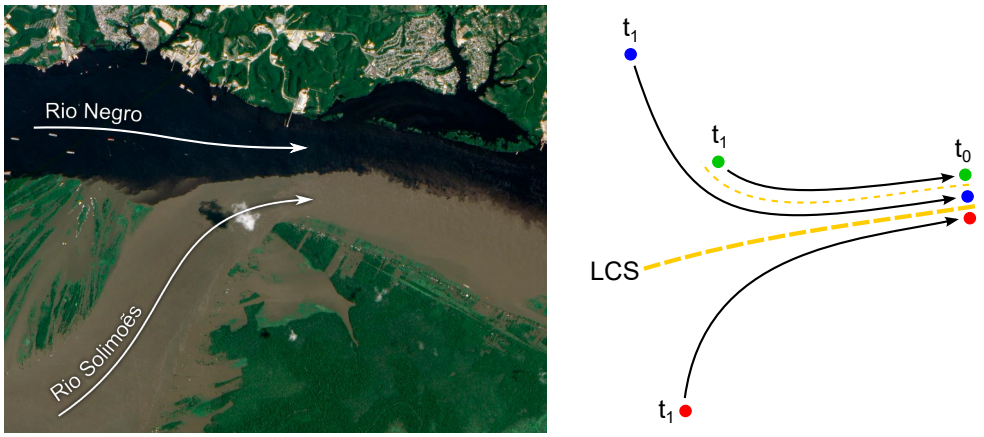

Figure 3.1: Lagrangian coherent structures (LCS) are virtual surfaces that describe the interface between particles with different history. Left: The confluence of Rio Negro (Black River) and Rio Solimoes (Muddy River) forms the Amazon River outside Manaus, Brazil. The waters flow in parallel for several kilometers as eddies gradually begin to mix the black and brown water. The boundary between the flows is an LCS. Image courtesy of Jesse Allen and Robert Simmon, NASA Earth Observatory. Right: A more technical definition, the likelihood of an LCS between particles at starting time t_0 is related to the degree of separation between them at a previous point in time t_1.

3.2.4 Vortex rings

There are at least three methods available to determine the outer boundaries of vortex rings: streamlines [157], dye injection with planar laser-induced fluorescence imaging [98], and Lagrangian coherent structures (LCS) [87], all of which agree in water tank experiments [87, 98, 99]. The applicability of the streamline method for *in vivo* flow is limited by the formative phase of the vortex ring, and dye injection is not feasible in humans due to their tendency to obstruct laser light.

The feasibility of using LCS to visualize and quantify vortex ring formation in the human heart was first demonstrated by Töger et al. [99]. An LCS can be understood as a surface (or line when viewed in a two-dimensional plane) that separates particles of different spatiotemporal origins (Fig. 3.1). The presence of an LCS between two particles can be calculated by computing the finite-time Lyapunov exponent (FTLE), which compares the positions of a group of particles at the starting time t_0 with an earlier point in time t_1 [99]. FTLE values were computed from the 4D flow field with t_0 set to end-diastole and t_1 set to a timeframe before opening of the mitral valve. FTLE values were subsequently normalized to the 95^{th} percentile of FTLE values for each timeframe separately. Lines with FTLE values above 50% of the normalized value were considered as LCS. Vortex ring volume was determined for each point in time during diastole by manual delineation of the outermost LCS, as seen in the short-axis view (Fig. 3.2). Long-axis views were also generated and used for guidance.

A vortex ring generator apparatus was used to create symmetrical vortex rings for com-

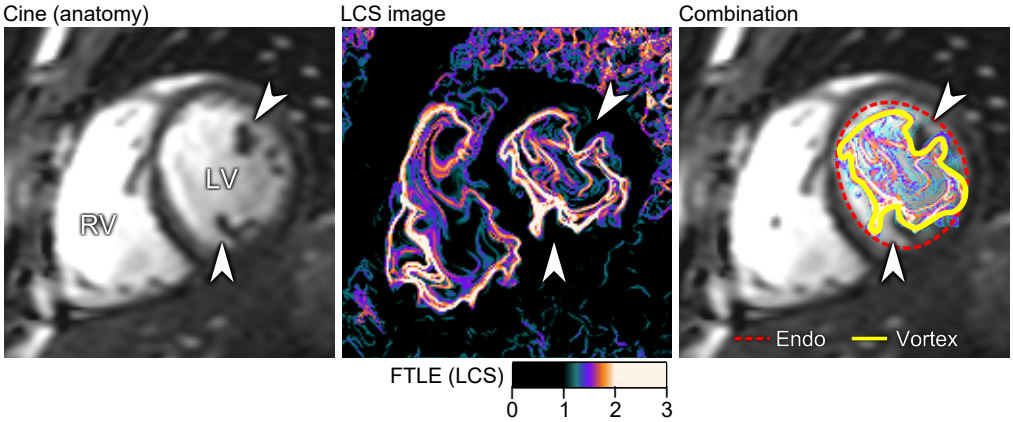

Figure 3.2: Midventricular short-axis view of the heart, showing anatomy (left panel), vortex ring boundaries by LCS visualization (middle), and a hybrid image combining the two (right). The vortex ring was delineated in the short-axis view (yellow line). Note the adaptation of the vortex ring to the papillary muscles (white arrowheads).

parison with *in vivo* conditions. The apparatus has been used in validation experiments to investigate the accuracy, precision, and stability of 4D flow measurements [158].

To evaluate the average distance between the vortex ring boundary and endocardial wall, the following steps were taken. First, find the radius of a sphere with volume equal to the LV volume; second, find the radius of a sphere with volume equal to the vortex ring volume; third, subtract the vortex ring radius from the LV radius. The average mitral annular diameter was computed by first determining the maximum effective mitral valve area using a previously described method [57], and then finding the diameter of a circle whose area equals the mitral valve area. The same approach was used to compute the largest LCS cross-sectional diameter, to enable calculation of the ratio between the largest vortex ring measure and the mitral valve area.

3.2.5 Hemodynamic forces

Computation of hemodynamic forces was performed by first using the Navier-Stokes equation to find the pressure gradient $\mathbf{g}$,

$$\mathbf{g} = -\rho\frac{\delta v}{\delta t} - \rho(v \cdot \nabla v) + \mu\nabla^2 v, \tag{3.3}$$

where v is the velocity from the 4D flow data. Blood viscosity was set to $\mu = 4{\cdot}10^{-3}$ Ns/m^2. The hemodynamic force was then calculated by integrating $\mathbf{g}$ over the entire ventricular volume, for each ventricle separately. Forces were decomposed into three orthogonal components (Fig. 3.3).

As suggested by Pedrizzetti et al. [114], the healthy ventricle is expected to exhibit forces that are primarily aligned with its long axis. To evaluate the degree of longitudinal

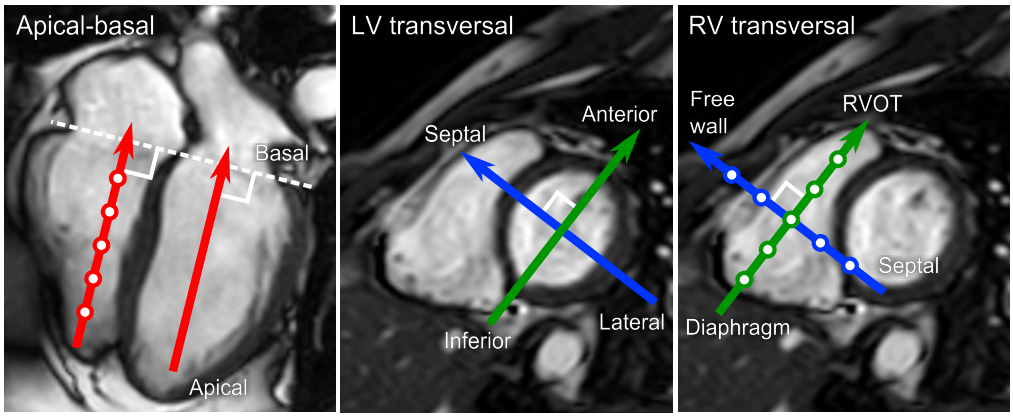

Figure 3.3: Spatial coordinate system used for three-dimensional hemodynamic forces. The AV plane was defined from intersection points placed in the three long-axis views. A three-dimensional plane was automatically fitted to these points by minimizing the residuals. The apical-basal direction was defined as being orthogonal to the AV plane. The septal-lateral direction was orthogonal to the apical-basal direction and transected the center of the LV and the left ventricular outflow tract, i.e. aligned with the three-chamber view. The inferior-anterior direction was orthogonal to the two other axes. The RV system used the same spatial definitions as for the LV, but with different nomenclature.

alignment, the ratio between transversal and longitudinal forces was computed for systole and diastole separately. The method was adopted from the one previously used by Eriksson et al. [112], with two modifications: 1) instead of using peak values, the root mean square value was used as this was deemed more robust, and 2) the ratio was computed for the entire transversal plane rather than limited to the anteroseptal-to-inferolateral axis. The reason for this approach was to make full use of the three-dimensional nature of the data. It was also assumed that while healthy hearts exhibit most of their force along the anteroseptal-inferolateral axis (as this axis intersects the mitral and aortic valves; the principal path of flow through the LV), significant divergences from this optimal force pattern could be present in dyssynchronus hearts. Root mean square (RMS) force in each orthogonal direction was calculated for systole and diastole in each ventricle,

$$\text{RMS} = \sqrt{\frac{1}{N}\Sigma_{n=1}^{N} f_n^2}. \tag{3.4}$$

For Paper III, the ratio between longitudinal and transversal forces was calculated,

$$\text{Ratio} = \frac{RMS_{apex-base}}{\sqrt{RMS_{inf-ant}^2 + RMS_{lat-sep}^2}}. \tag{3.5}$$

After further consideration, it was deemed more sound to put the transversal component in the numerator, as it is expected to assume small values in healthy hearts. This approach

was used in Paper IV as well as for the results presented in the present thesis:

$$\text{Ratio} = \frac{\sqrt{RMS_{inf-ant}^2 + RMS_{lat-sep}^2}}{RMS_{apex-base}}. \tag{3.6}$$

Early diastolic filling impulse

The area under the force curve is by definition a measure of the impulse,

$$\text{Impulse} = \bar{F}\Delta t. \tag{3.7}$$

The impulse inscribed by the apically directed force during the beginning of the E-wave could therefore be a measure of the diastolic suction performance of the ventricle. This **filling impulse** was quantified from aortic valve closure to minimize the confounding factor of decelerating outflowing blood. Therefore, the resulting measure is to be considered a lower limit on the actual force involved in aspirating blood in the ventricle.

Quantification of ventricular dyssynchrony

The global effect of dyssynchrony on ventricular function was assessed as the time between peak forward flow in the pulmonary trunk ($\hat{Q}p$) and peak forward flow in the aorta ($\hat{Q}s$). The QRS duration was also measured from the standard 12-lead electrocardiogram.

3.2.6 Visualization of results

The intraventricular pressure field was calculated for visualization purposes, using a previously published multigrid solver to compute the pressure Poisson equation (*antigradient2.c*, available from `http://github.com/GunnarFarneback/spatial_domain_toolbox`) [159, 160].

Kinetic energy was visualized using the freely available open-source software FourFlow (`http://fourflow.heiberg.se/`) and Segment (Medviso, Lund, Sweden) [154]. Figures were prepared using GNU Image Manipulation Program 2 (`http://www.gimp.org/`) and Inkscape 0.48.5 (The Inkscape Project, `http://inkscape.org/`).

3.2.7 Statistical methods

Due to the relatively small sample sizes used in the studies, nonparametric tests were generally preferred as they do not assume normal distributions. The reader is kindly directed to the individual papers for specific details on the tests used.

Chapter 4

Results and interpretation

Whatever you see – any good results – are all from the pressure.

Ziyi Zhang

4.1 Atrial kinetic energy

Atrial kinetic energy contained three peaks in all 15 subjects, as shown in Fig. 4.1. The first peak was seen during ventricular systole, the second during early filling, and the third peak was seen in conjunction with atrial contraction. Fig. 4.2 shows a visualization of the three KE peaks in a representative subject. During systole, LA KE was highest near the pulmonary vein inlets, and RA KE was seen in a toroidal pattern which was 'fed' from the caval veins. In early diastole, LA KE increased rapidly and was seen in a contiguous streak from the middle of the atrium into the central part of the LV. Right atrial KE increased less sharply during early diastole, and the toroidal pattern assumed a more tube-like shape as the RA blood transited the AV plane through the tricuspid valve. Late diastolic KE was seen in the regions surrounding the mitral and tricuspid valves, in the atrial appendages, and in the caval and pulmonary vein inlets.

4.1.1 Left atrial KE

Left atrial KE averaged 1.1 ± 0.1 mJ over the cardiac cycle and showed a correlation with left atrial size (r^2 = 0.38, $p < 0.05$). This correlation was expected, given the dependence of kinetic energy on the mass of the blood. Systolic average KE was correlated with the average AV plane velocity ($r^2 = 0.26$) and atrial peak volume ($r^2 = 0.55$). Combined, these factors explained the majority of systolic KE (Fig. 4.3). During early rapid filling, left atrial KE increased on average by 3.2 ± 0.27 mJ compared to the KE decay model, and reached peaks of 3.5 ± 0.25 mJ. The increase correlated with LV myocardial mass ($r^2 = 0.28, p < 0.05$) but not with atrial size. The early diastolic peak was larger than the

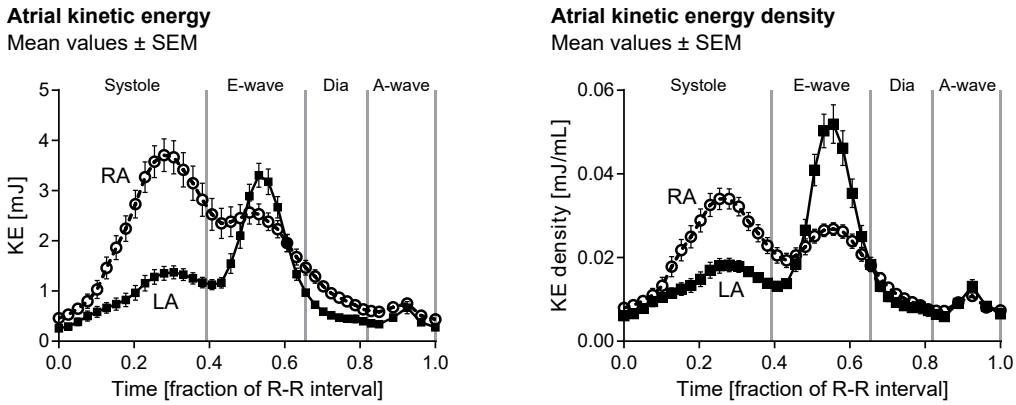

Figure 4.1: Atrial kinetic energy displayed three peaks in both atria; one during systole, one during the early rapid filling (E-wave), and one during atrial contraction (A-wave). The KE density was higher in the RA during systole and higher in the LV during the E-wave. Mean values ± SEM.

systolic ($p < 0.001$) and late diastolic peak ($p < 0.001$).

4.1.2 Right atrial KE

Similar to the LA, right atrial KE contained three peaks; however, the systolic peak was significantly higher ($p < 0.001$) and the early diastolic peak was slightly lower ($p < 0.05$) than in the LA. Right atrial KE averaged 1.7 ± mJ and correlated with mean RA volume ($r^2 = 0.53, p < 0.01$). Similar to the LA, average systolic RA KE was correlated with both AV plane velocity ($r^2 = 0.41$) and peak atrial volume ($r^2 = 0.49, p < 0.01$). Together, the AV plane velocity and peak atrial volume explained 64% of the variation in KE (Fig. 4.3. The KE increase during early rapid filling was not correlated to right ventricular mass ($p = 0.55$) or atrial size.

4.1.3 Rotational KE

Rotational KE constituted on average 46% in both atria. The ratio between rotational KE and total KE was not correlated to heart rate ($p = 0.08$ for both atria) or to average total KE ($p = 0.22$ for both atria). Fig. 4.4 shows the relationship between rotational KE (RKE) and non-rotational KE (NRKE) for both atria. The decay rate of RKE was slower compared to NRKE, indicating that rotational flow preserves kinetic energy to a greater extent than non-rotational flow does. During peak E-wave, the angle between the atrial rotational axis and the average flow direction was 39° ± 23° (mean ± SD) in the right atrium. This indicates blood motion along the rotational axis, which translates into a helical motion. Conversely, the angle was 85° ± 23° for the left atrium, indicating tumbling rather than helical flow.

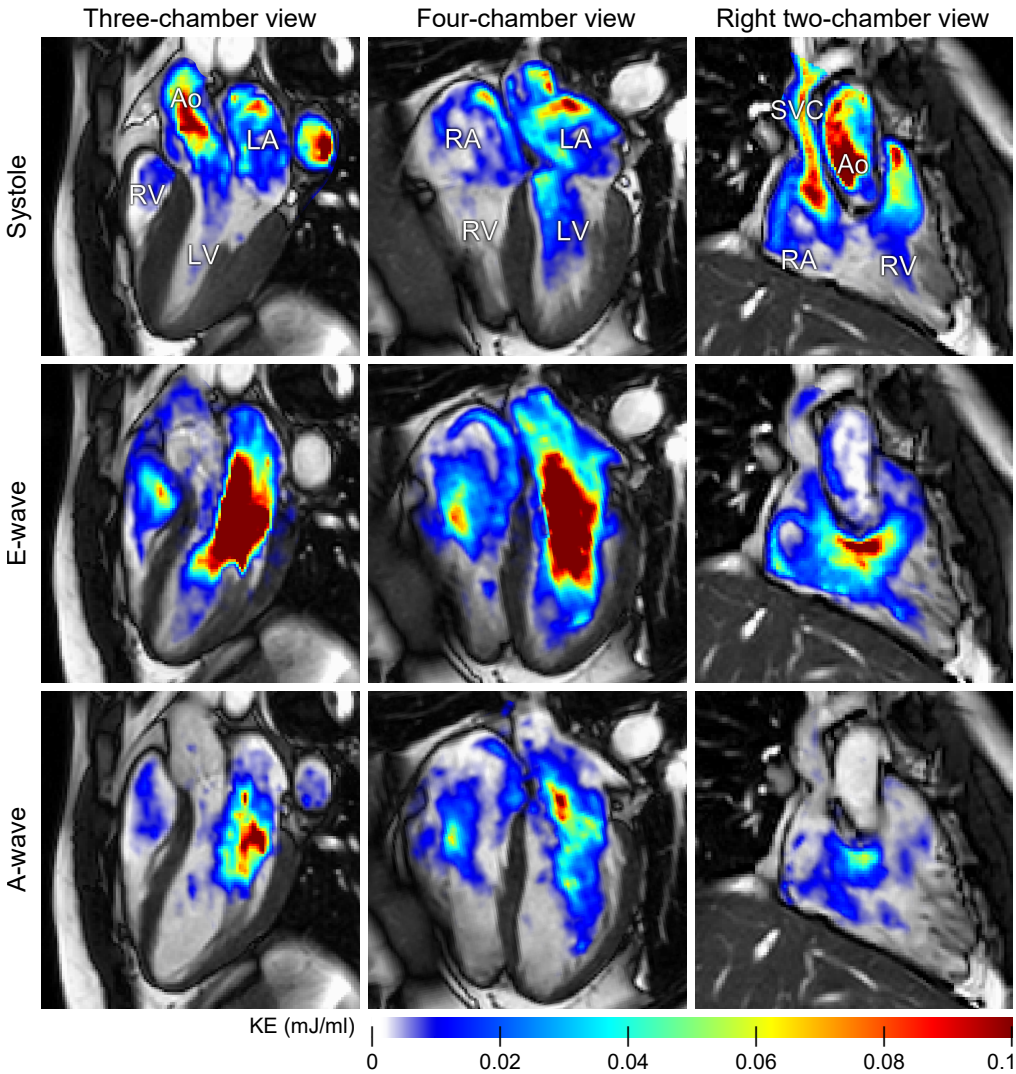

Figure 4.2: Visualization of intracardiac kinetic energy in three long-axis views during systole, E-wave and A-wave. Note the rotational flow pattern in the right atrium, which is fed by inflowing blood from the superior vena cava (SVC), best viewed in the top right panel.

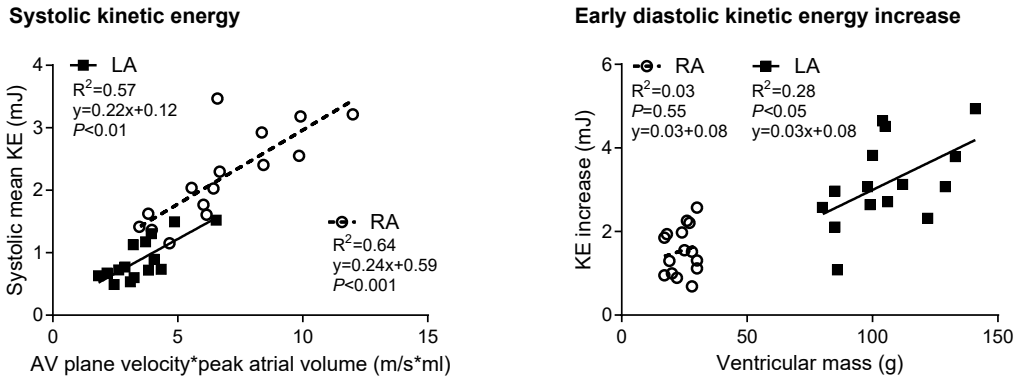

Figure 4.3: Systolic kinetic energy was partially explained by the product of average AV plane velocity and the peak atrial volume. Early diastolic KE increase was related to LV mass in the left atrium, but no correlation was seen between RV mass and RA KE increase.

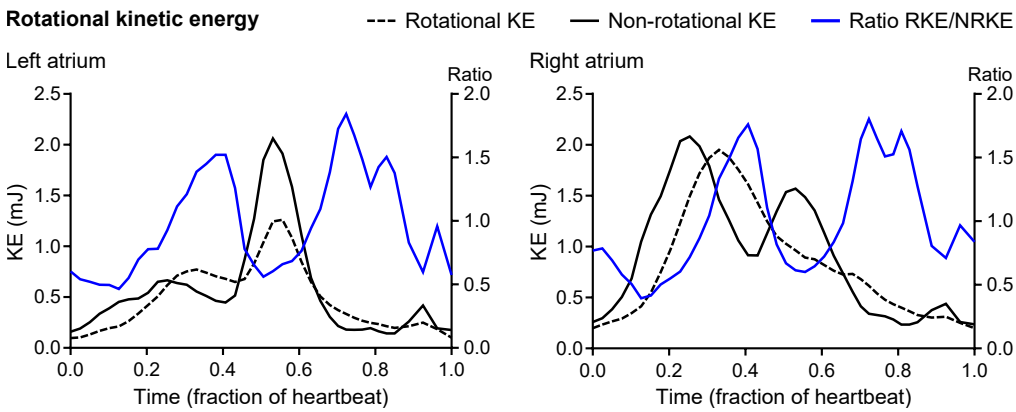

Figure 4.4: Rotational and non-rotational kinetic energy in the left and right atrium (mean values). The ratio increased after non-rotational KE peaks, indicating that rotational flow conserves KE to a larger extent compared to non-rotational KE. The time delay from NRKE to RKE peaks suggests that rotational flow is driven by straight flow.

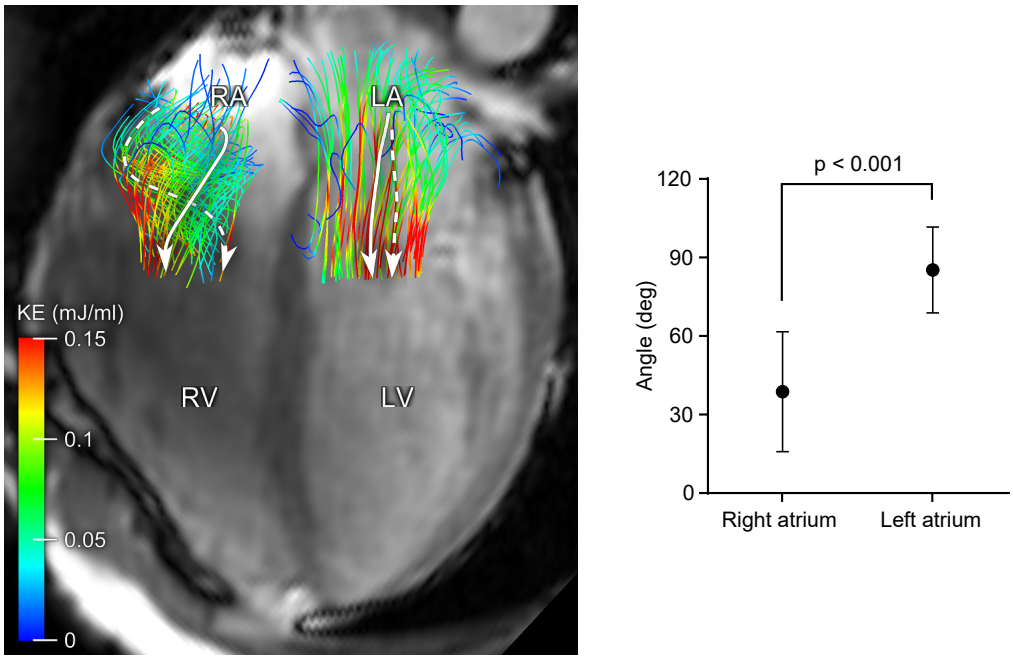

Figure 4.5: Helical flow across the AV plane during early rapid filling. Left: Streamlines emitted from planes situated at the AV plane visualize the instantaneous flow field and show the presence of helical flow from the RA into the RV. Conversely, flow from the LA into the LV is more straight. Solid white arrows indicate the flow direction closest to the reader, dashed arrows demarcate flow further away. Right: the angle between the net flow direction and axis of rotation in both atria during peak E-wave (mean $\pm$SD). Values close to 0° or 180° indicate helical flow; values close to 90° indicate non-helical flow.

4.1.4 Interpretation

Perhaps the most striking finding in atrial KE is the difference in energy gain during the early rapid filling phase, where LA KE increased much more abruptly than RA KE. The observed correlation between LA KE increase and LV mass provides no proof of causality, but fits well with the established theory of ventricular suction. Since KE is a measure of the amount of energy invested in accelerating the blood, an increase must be secondary to some external work being performed on the blood pool in the form of pressure gradients. Such a gradient could theoretically originate from the preatrial vasculature (*vis a tergo* – 'a force from behind'), the atrium itself (release of elastic energy from the atrial wall [161]), or from ventricular suction (*vis a fronte* – 'a force from the front') [24, 29]. The *vis a tergo* model of cardiac filling has been largely abandoned as knowledge on cardiac filling dynamics has increased, and the theory of atrial elasticity does not hold water as it is incompatible with the previously described conduit volume [43, 45].

The relatively small KE gain in the right atrium may be attributed to the weaker suction force generated by the RV compared to the LV [103, 162–165]. Since the tricuspid valve is larger than the mitral valve, and the right atrium combines a high KE density (Fig. 4.1) with anatomy that promotes swirling of the blood, RV filling can be augmented by redirection of rotational flow with minimum effort. The longer AV plane displacement of the right heart [46] also combines well with the larger AV valve, since it minimizes the amount of work necessary to transport blood from the atrium into the ventricle [150]. These factors together may help optimize the right heart for energy-efficient forward flow. Even though atrial KE represents a small fraction of the total energy expenditures of the heart, it may become increasingly important during exercise as the momentum transfer increases. A biological system of such central importance as the heart would benefit from optimizing its function from several different perspectives, to provide some redundancy for critical situations [166]. It is therefore reasonable to assume that high-intensity exercise is supported by several different adaptations that come into play simultaneously, where KE conservation might be one.

4.2 Relationship between vortex ring and endocardium

Sixteen controls and 23 heart failure patients with left ventricular dyssynchrony were studied. *In vivo* measurements were compared with symmetrical vortex rings generated in the water tank, shown in Fig. 4.6.

4.2.1 Measurements of *in vivo* vortex ring formation

Figure 4.7 shows a visualization of vortex ring formation in three representative subjects: one healthy control, one patient with ischemic heart disease, and one patient with dilated cardiomyopathy. Numerical results of the experiments are summarized in Fig. 4.8. In healthy controls, vortex rings appeared soon after commencement of the early filling phase.

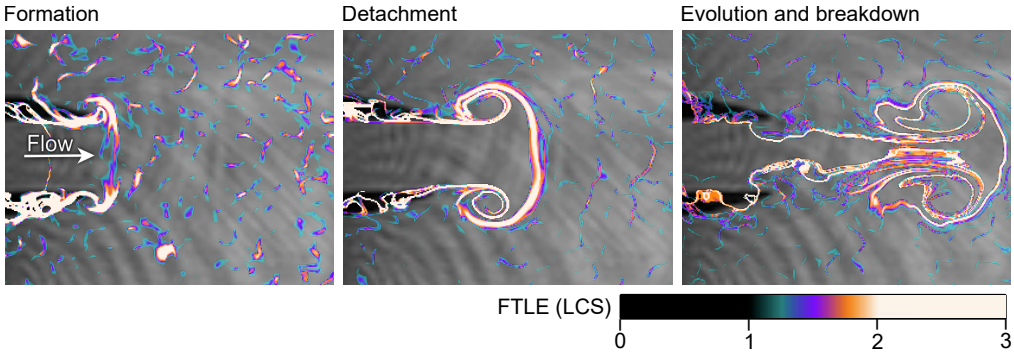

Figure 4.6: Symmetrical vortex ring formation visualized using Lagrangian coherent structures (LCS). As the vortex ring forms due to water injection through the nozzle on the left, the finite-time Lyapunov exponent (FTLE) field reveals the appearance of LCS. The outermost LCS defines the outer boundary of the vortex ring. After forming, the vortex ring detaches and then begins its gradual evolution and breakdown into smaller-scale vortices.

The vortex ring grew gradually until termination of the early filling phase, after which the growth rate slowed down. At end-diastole, vortex rings in controls occupied on average 53% of the total ventricular volume (95% confidence interval: 49-58%), and the average distance between the vortex boundary and endocardial wall was consistently around 7 mm (range: 4.4-9.1). There was a strong correlation between LV end-diastolic volume and vortex ring volume ($R^2 = 0.83, p < 0.0001$). The vortex ring volume was not affected by the inflow peak velocity ($p = 0.17$). This indicates that healthy ventricles are adapted to accommodate vortex ring formation regardless of size. As expected, the vortex ring volume was also correlated to the stroke volume ($R^2 = 0.76, p < 0.0001$).

In patients, a marked disconnection between the vortex ring boundary and endocardial border was seen. The vortex boundary formed at a greater distance from the myocardial wall and developed continuously throughout diastole, until it constituted on average 35% of the ventricular volume (95% CI: 30-41%). The average distance at end diastole was 13 mm (range 5.4-26.9) and there was no correlation between vortex ring volume and ventricular end-diastolic volume. These findings were taken to indicate that failing, dilated ventricles have lost the physiological coupling between the endocardium and vortex ring boundary.

4.2.2 Comparison with symmetrical vortex rings

Comparing intracardiac vortex formation with symmetrical vortex rings in the tank revealed several discrepancies. Most importantly, the healthy ventricles all demonstrated elongated vortex rings which were visibly affected by their interactions with the surrounding myocardium. This phenomenon is visible both in the adaptation to papillary muscles (Fig. 3.2) and in the asymmetry of the vortex ring as seen in the three-chamber view

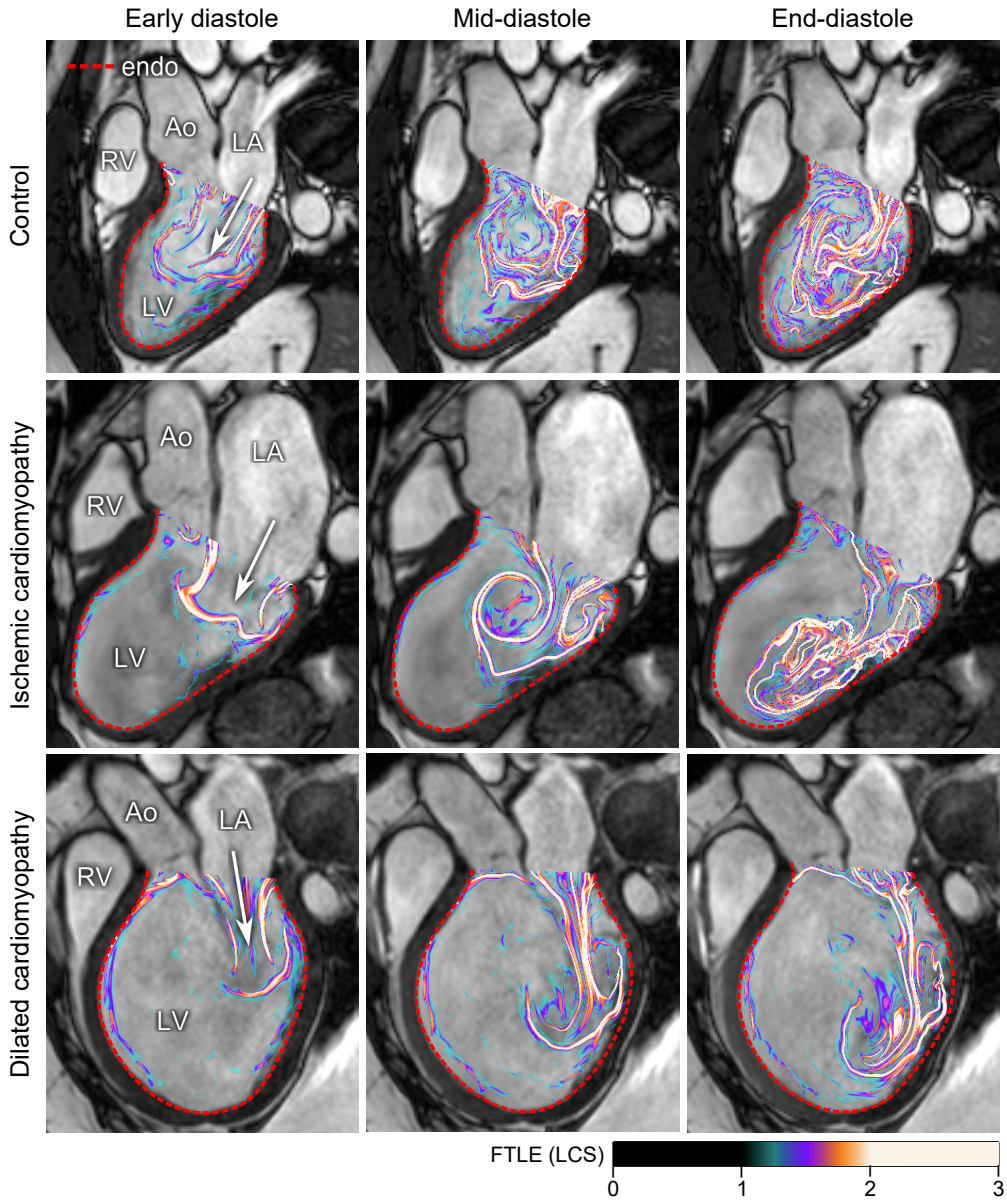

Figure 4.7: Vortex ring formation in three representative subjects, as seen in the three-chamber view.

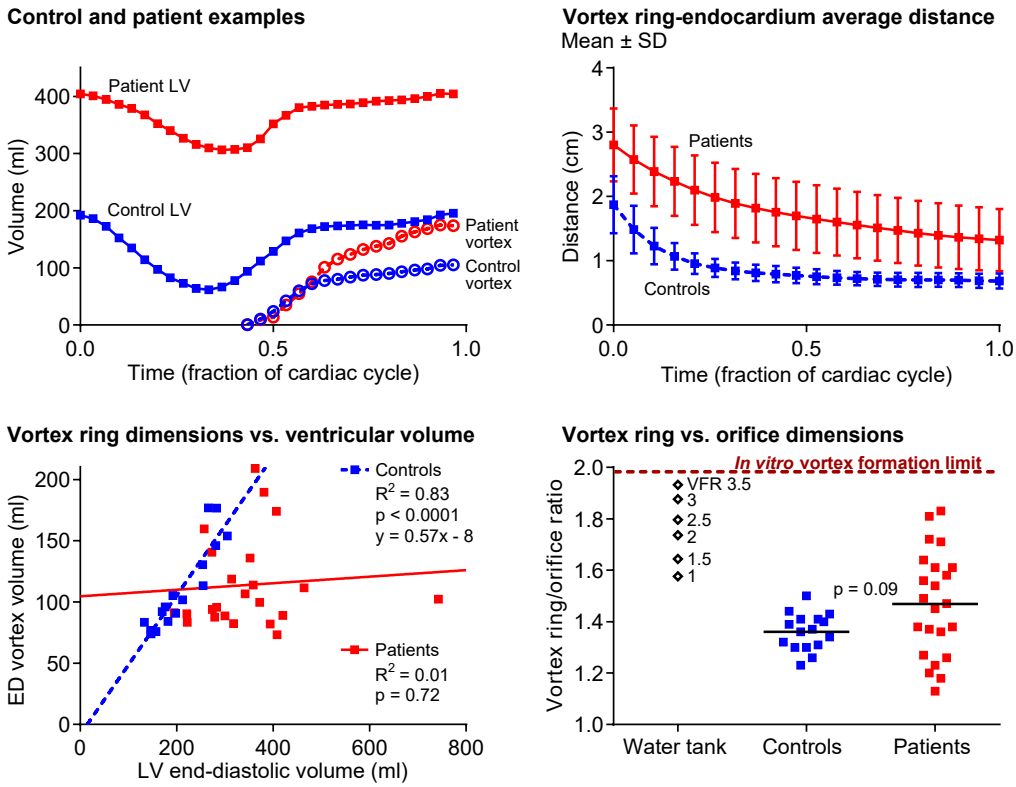

Figure 4.8: Quantitative analysis of the vortex ring boundary in controls and patients. Top left: Vortex ring and ventricular volume over time in two representative subjects. Note that the vortex ring continues to grow throughout diastole in the patient. Top right: Distance between vortex boundary and endocardium in all subjects. Bottom left: Correlation between left ventricular end-diastolic volume and vortex ring volume. Bottom right: the ratio between vortex ring and orifice diamter in water tank experiments, controls, and patients. Some patients had a ratio near the theoretical maximum, suggesting that vortex formation may limit their ventricular filling performance.

(Fig. 4.7), where the posterior vortex core was smaller than the anterior core. As previously stated, the maximal volume incorporated in a freely developing vortex ring is chiefly determined by the vortex formation ratio. Further growth after exceeding VFR ≥ 4 is solely due to entrainment of ambient fluid which is made possible by providing a counterflow; in the absence of a counterflow, the vortex ring does not grow after pinch-off [157]. As a consequence, the outer diameter of the vortex ring is also mainly limited by VFR. In the water tank, the ratio between the vortex ring diameter and the orifice increased in a linear fashion from ratio ≈ 1.6 at VFR = 1 to ratio ≈ 1.95 at VFR = 3.5 (the experimental setup did not allow VFR ≥ 4 conditions). The ratio in controls was found clustered around 1.4, however, while patients spanned a larger range from 1.1 to 1.8. This was interpreted to represent a reserve capacity for vortex ring formation in controls; by altering the ventricular geometry, as is the case during exercise [42, 58], larger vortex rings can be created. Such a mechanism would enable the ventricle to remain small and hence conserve energy during rest, and to dynamically optimize its filling function when the preload increases and ventricular volumes rise during exercise.

4.2.3 Interpretation

It appears that the spatiotemporal behavior of the healthy left ventricle is optimized to (barely) accommodate vortex ring formation during rest. Previous studies of cardiac volumes during exercise have demonstrated increased diastolic volumes [42, 167–172], which suggests that vortex formation conditions may improve during physical exertion. The effective area and motion of the mitral valve has been shown to change over time [57, 173] and with varying loading conditions [174], which is also likely to affect vortex ring formation.

Myocardial remodeling is influenced by reactivation of several different genetic programs [123] which may be moderated by flow-sensitive cilia on the endocardial surface [175]. In light of the regulatory effect of blood flow on endothelial function and remodeling [13], the strong dimensional coupling between vortex ring and endocardium therefore suggests that the vortex ring might constitute the fluid-dynamic 'blueprint' to which the growing heart can adapt. Pathologically induced alterations to the epigenetic regulation of shear-sensitive cardiac growth programs may cause loss of vortex-wall coupling; conversely, a primary disturbance in vortex formation may impair normal ventricular development. This theory is further supported by the observation that LV hypoplasia is a relatively common complication in congenital mitral stenosis [176].

The matching of myocardial dimensions to the vortex ring conveys several other possible advantages, including optimal mixing of ventricular blood [96, 97], maintenance of low filling pressures [93], prevention of thrombus formation [177], and efficient transition from filling to ejection [91]. Furthermore, it has recently been shown that the kinetic energy within the vortex ring may be altered in heart failure [132], indicating the potential utility of LCS vortex ring analysis to elucidate other aspects of flow.

4.3 Hemodynamic forces in health and heart failure

Twenty-five controls and 14 elite endurance athletes were included. Athletes were younger, had lower resting heart rate, higher LV mass, and larger right ventricular volumes compared with controls, in line with previous studies [178]. Imaging and quantification of hemodynamic forces was possible in both ventricles for all subjects. Fig. 4.9 shows relative pressure maps and hemodynamic forces in both ventricles of a representative subject. As expected, force patterns were significantly different between ventricles.

4.3.1 Hemodynamic forces in normals and athletes

Left ventricular forces displayed a large systolic peak towards the base and septum, indicating acceleration of blood towards the aorta. This was followed by a smaller, apically directed peak corresponding to the deceleration of the outflowing blood. Early diastole contained an apically directed peak, accelerating blood into the ventricle, which was followed by a significantly larger basally directed peak, decelerating the inflowing blood. This pattern repeated itself in conjunction with the A-wave, but with smaller magnitudes since the volumes and velocities involved were lower. Lateral-septal and inferior-anterior forces were generally small during diastole. This pattern was repeated in all subjects, as shown in Fig. 4.10.

In the right ventricle, systole contained an early, large peak aimed towards the right ventricular outflow tract (RVOT), corresponding to acceleration of ejecting blood, as well as a smaller basal component. There was also a mid-systolic force acting towards the septum. This is the centripetal force needed to 'sling' the blood around the septal curvature. The apical-basal component was similar to that of the LV, but with smaller magnitude suring the early rapid filling, and no distinct separation of the apically oriented late systolic and early diastolic forces. Right ventricular forces in all subjects are shown in Fig. 4.11. Force patterns were strikingly similar between subjects, with variations occurring mainly in the amplitude, not timing of forces.

The ratio between transversal (in-plane) and longitudinal RMS forces was significantly different between the ventricles, and also between cardiac phases (Fig. 4.12). Left ventricular filling and emptying is associated with forces mainly in the longitudinal axis, indicated by a low ratio. Conversely, a larger fraction of RV forces are spent accelerating blood in the transversal plane, both in systole and diastole.

No differences were seen between controls and athletes in terms of early diastolic filling impulse.

4.3.2 Hemodynamic forces in left ventricular dyssynchrony

Thirty-one patients with LV dyssynchrony were analyzed. One typical case is shown next to a control in Fig. 4.13. While the lateral-septal force was higher in the patient during

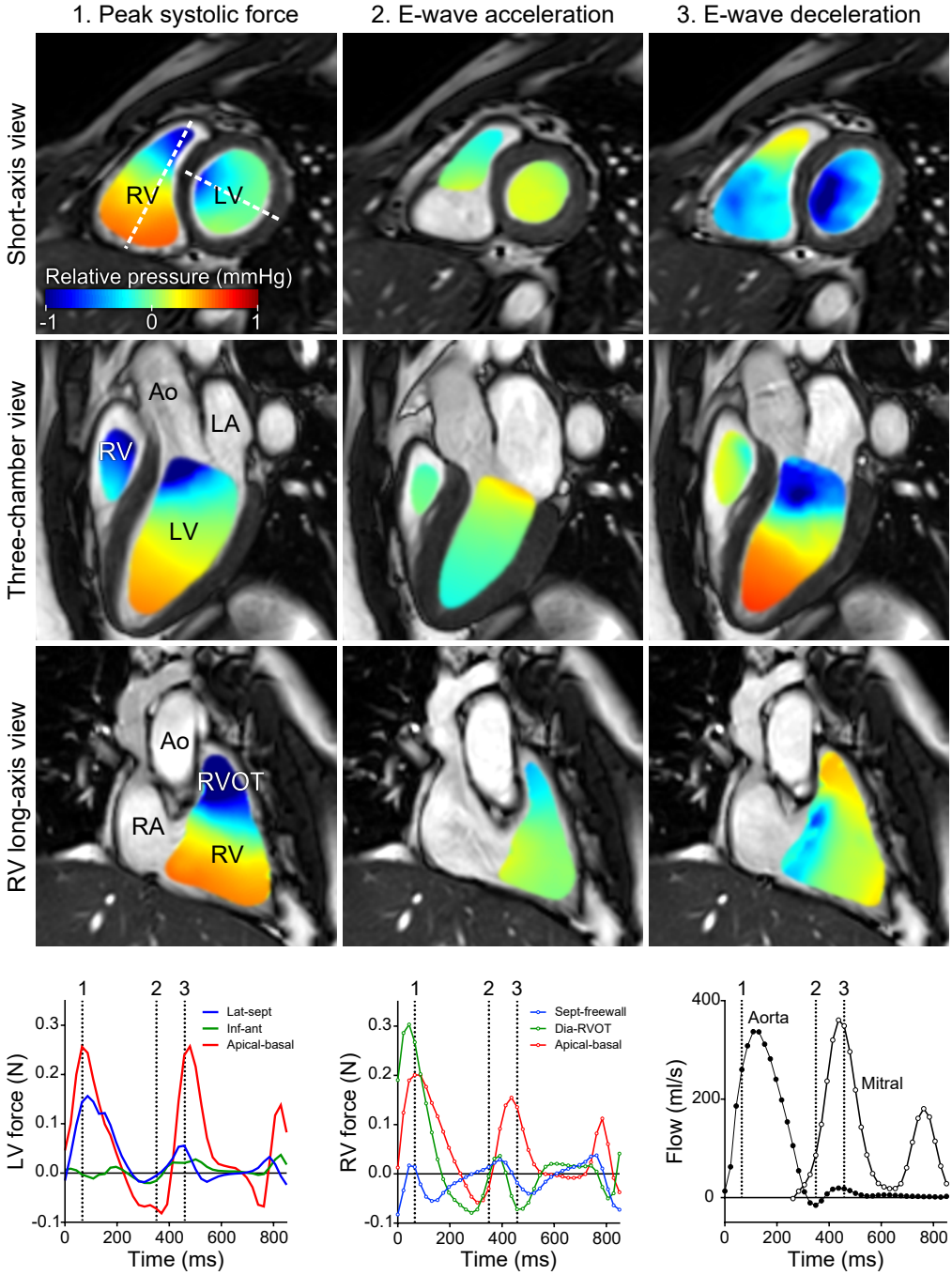

Figure 4.9: Visualization of hemodynamic forces in one representative healthy volunteer. Top: Local forces visualized as relative pressure maps. Bottom row: Global hemodynamic force in the left ventricle (left panel) and right ventricle (center panel). Aortic and transmitral flow curves are shown for reference (right panel).

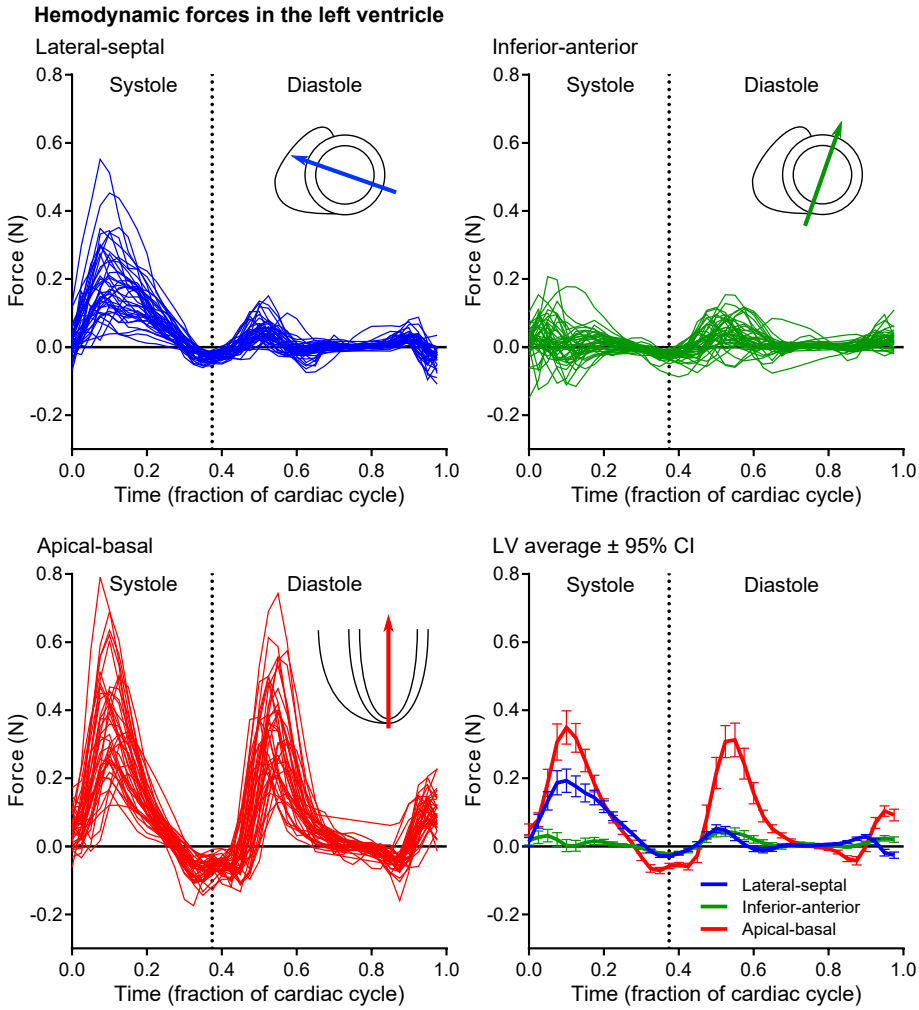

Figure 4.10: Left ventricular hemodynamic forces in 39 subjects. Note the similarities between subjects in the lateral-septal and apical-basal directions, and less homogenous patterns in the inferior-anterior direction. During systole, forces were mainly seen in the apical-basal and lateral-septal directions, reflecting the acceleration of blood towards the aorta. During the E-wave, apical-basal forces dominated. Atrial contraction was reflected in the smaller, late diastolic peaks seen in all three directions. Bottom right: average values ± 95% confidence interval.

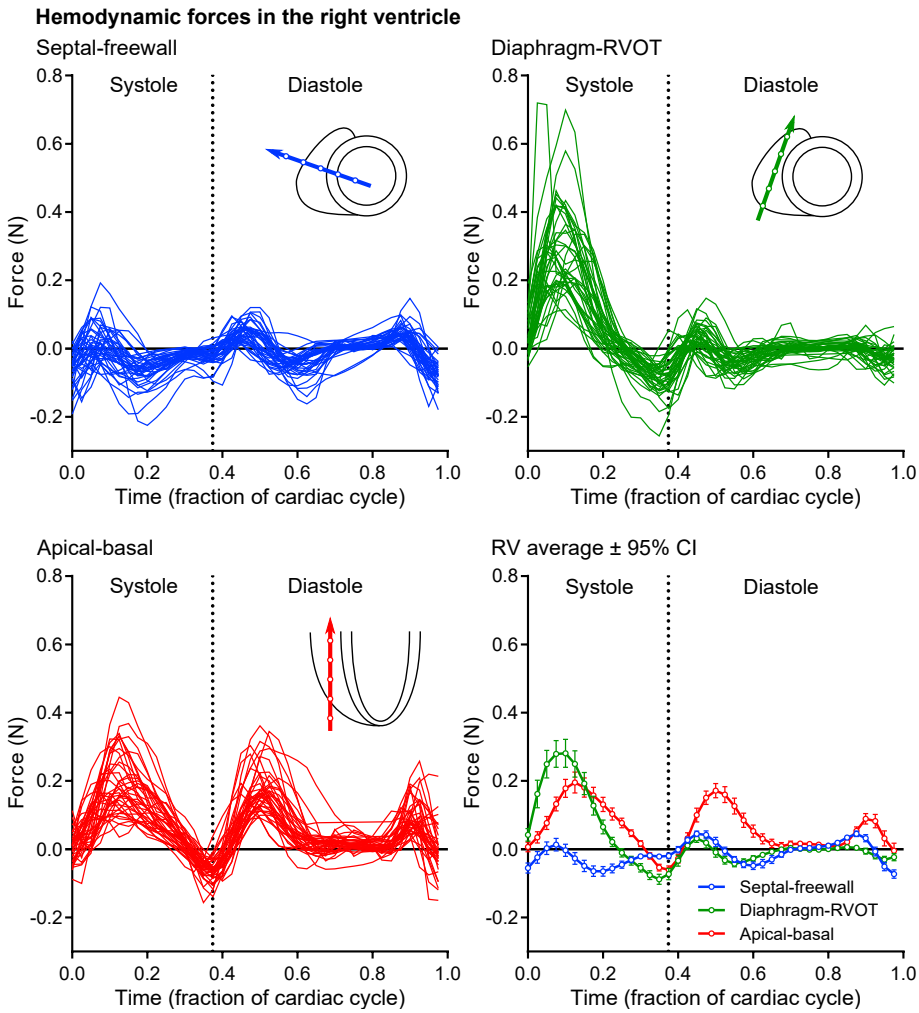

Figure 4.11: Right ventricular hemodynamic forces in 39 healthy subjects. The largest systolic forces were seen in the diaphragm-RVOT direction, indicating that the largest acceleration of blood in the RV occurs in the transversal plane. Smaller peaks were seen in the apical-basal direction. The septal-freewall direction contained a mid-systolic peak aimed towards the septum, reflecting the centripetal acceleration required to sustain motion of blood around the septum.

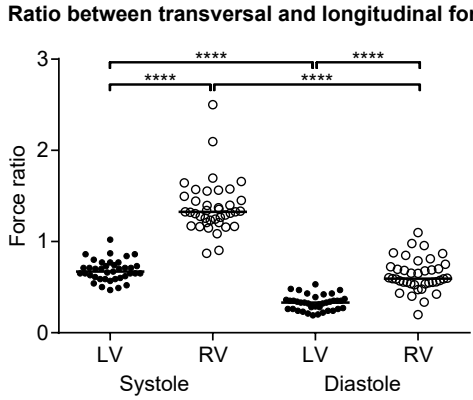

Figure 4.12: The ratio between transversal (in-plane) and longitudinal forces. ****, $p < 0.0001$.

systole, the largest difference was seen in diastole, where transversal forces eclipsed the longitudinally oriented ones. In contrast with normal subjects, patients displayed a variety of force patterns (Fig. 4.14). The differences were especially pronounced during diastole, and resulted in difficulty comparing the average values between controls and patients. An attempt at grouping the patients by visual appearance was therefore made, which resulted in three distinct force patterns (Fig. 4.15). The resulting grouping showed some consistency with the type of inflow pattern over the mitral valve. The largest group, Pattern 2, demonstrated seemingly normal hemodynamic forces during systole, but diminished forces in the apical-basal direction during the E-wave.

The ratio between transversal and longitudinal forces was significantly altered in patients compared to controls and athletes (Fig. 4.16) but was not related to Qp-Qs flow peak separation or QRS duration (Fig. 4.17).

4.3.3 Interpretation

Hemodynamic forces were found qualitatively similar in all healthy subjects independent of cardiac dimensions, with variation mainly in amplitude, indicating their central role in normal cardiac function. From this, it follows that hemodynamic force expenditures are tuned to accelerate blood similarly in small and large healthy hearts. While hemodynamic forces do not distinguish between athletes and controls, i.e. super-normal vs. normal, they do separate healthy from diseased by illuminating fundamental aspects of myocardial function.

The longitudinal alignment of forces is lost in heart failure with LV dyssynchrony. Previous studies have suggested that loss of longitudinal force alignment within the three-chamber view may be sufficient to aggravate ventricular remodeling [114]. Here it has been shown that the healthy LV exhibits non-negligible transversal forces during systole, including small but detectable inferior-anterior forces. Pathologically increased forces in

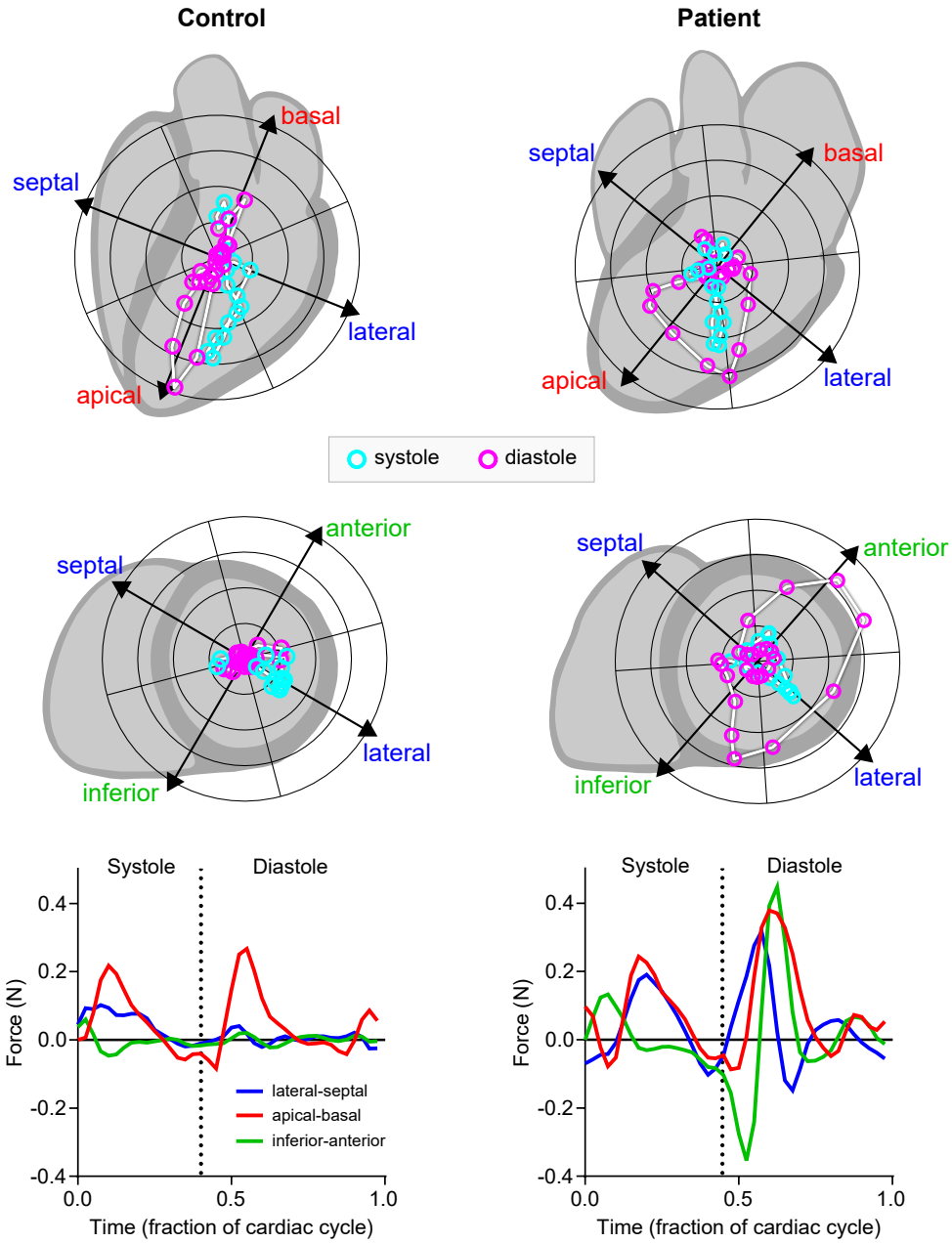

Figure 4.13: Hemodynamic forces in a control and a patient with ischemic cardiomyopathy and LV dyssynchrony. Top, middle rows: Polar plots showing the momentary direction and magnitude of the hemodynamic force over the cardiac cycle. Note the large diastolic force 'loop' in the patient, indicating that blood is being accelerated in various directions in the transversal plane. Bottom: The patient exhibited a marked discrepancy from the control when comparing lateral-septal and inferior-anterior forces during diastole.

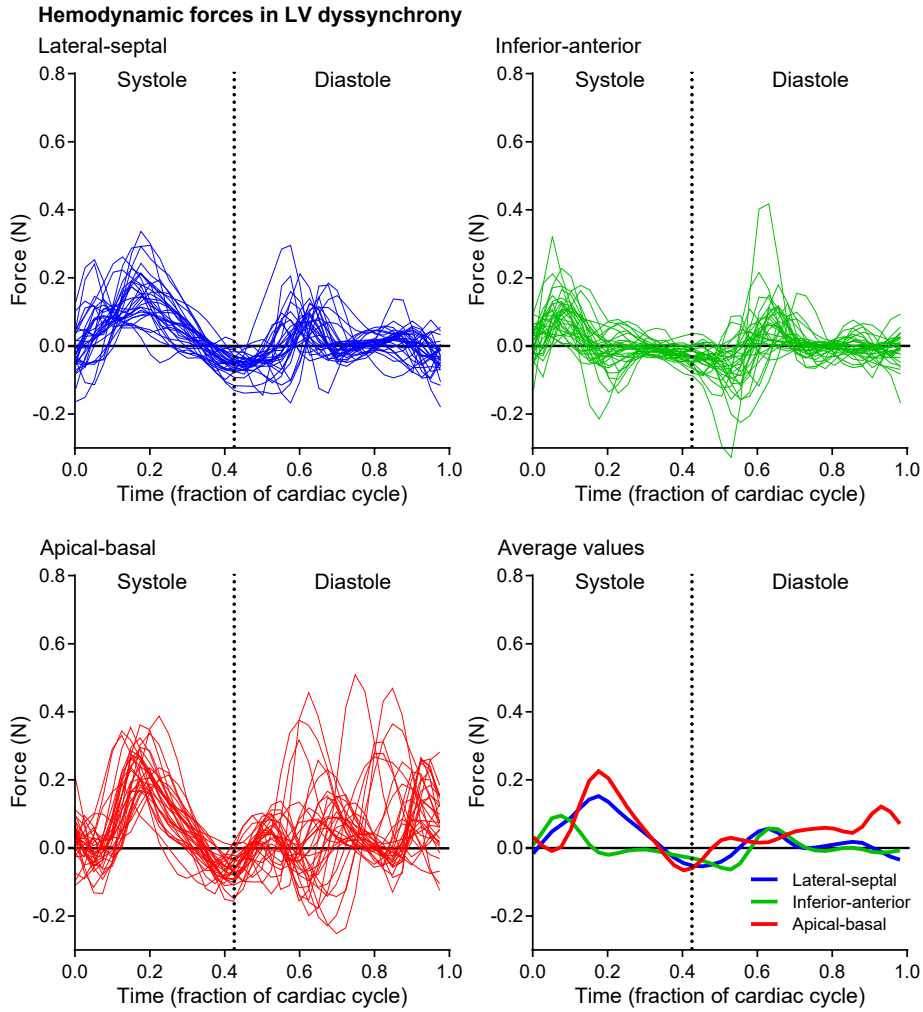

Figure 4.14: Hemodynamic forces in 31 heart failure patients. Note that while the systolic force peaks are somewhat adequately represented in the average results (bottom right), the diastolic forces are not well represented, especially in the apical-basal direction.

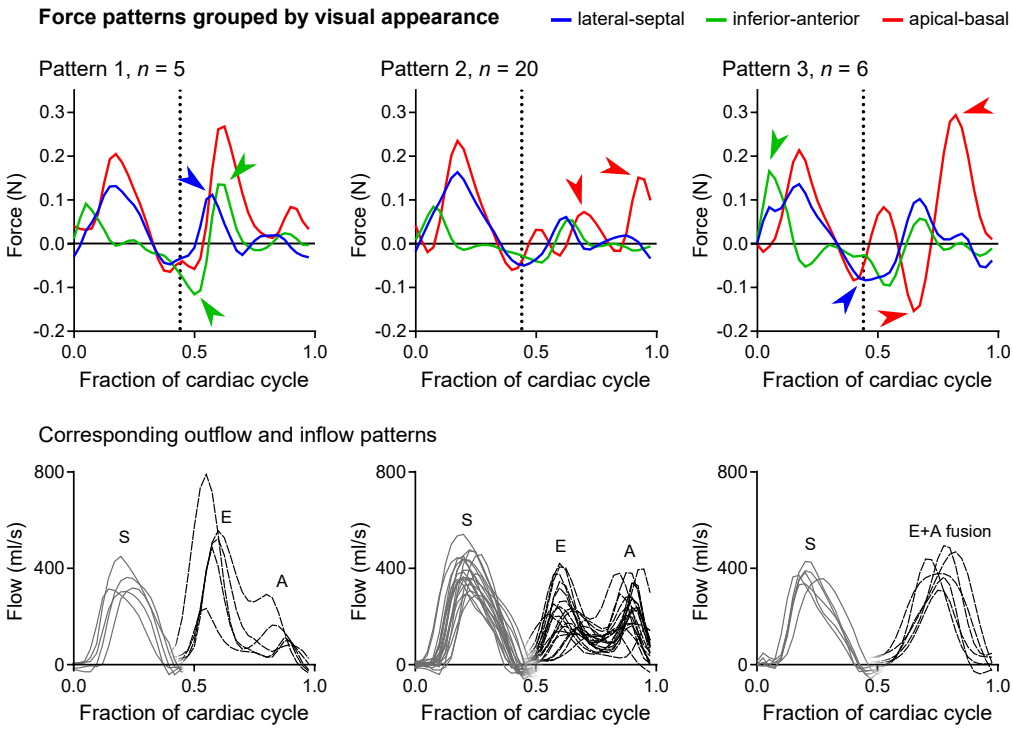

Figure 4.15: Classification of the visual appearance of the hemodynamic force patterns resulted in three patient groups (top row, mean values). Pattern 1 was distinguished by increased lateral-septal and inferior-anterior forces during the E-wave. All patients in this group had an E/A ratio >1 (bottom row). Pattern 2 showed diminished forces in the apical-basal direction during the E-wave, and increased apical-basal forces during the A-wave. Pattern 3 presented with aberrations in all three directions, including a large early systolic peak in the inferior-anterior direction, and large late diastolic peaks in the apical-basal direction. Transmitral flow patterns all revealed E-A fusion in this group.

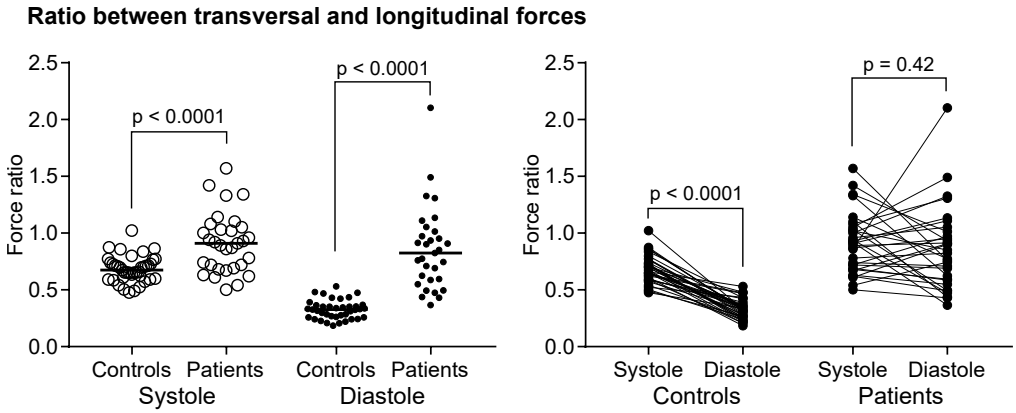

Figure 4.16: The ratio between transversal and longitudinal forces was significantly altered in patients compared to controls, both in systole and diastole. The diastolic ratio was lower than the systolic ratio in all controls (right panel); this was not true for patients.

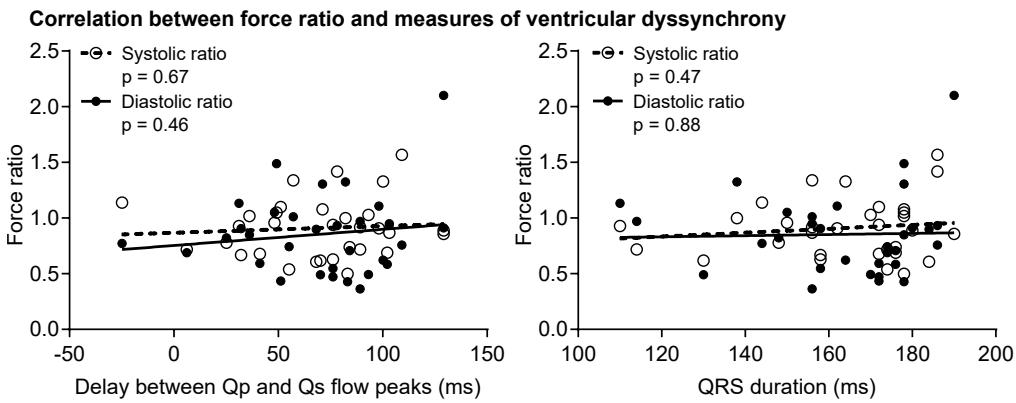

Figure 4.17: The ratio between transversal and longitudinal forces was not related to the delay between aortic and pulmonary flow peaks or the QRS duration.

the inferior-anterior direction (Fig. 4.13) have not been described before and can equal or overshadow those seen in the lateral-septal direction. This finding underscores the added value of three-dimensional analysis; aberrant forces may present in only one direction which is more likely to be detected by a 3D method.

The aim of CRT device implantation is to optimize the synchronicity of the myocardium; pre-implant evaluation has been hampered by the difficulty of securing reliable wall motion measures. Wall motion measures such as SD-TTS (standard deviation of time to peak transverse strain) have shown limited utility to predict treatment response [118], which may be due to the unspecific nature of an increased standard deviation. A standard deviation can be increased for several reasons, including randomly disordered contraction, delayed but simultaneously contracting lateral wall, or a harmoniously delayed contractile sequence. Since hemodynamic forces reflect the effects of wall motion on the flow, they may provide additional value for therapy guidance; the mere existence of significant transversal forces indicates non-physiological flow (not meaningful in terms of fluid transport) and hence potential benefit from resynchronization. This notion is further supported by the existence of several distinct force patterns, possibly reflecting different stages of myocardial dysfunction. In cases where wall motion is entirely absent in large sections of the ventricle, such as in post-infarct aneurysms, force analysis should be interpreted with caution.

The absence of differences between athletes and controls was unexpected, since athletes have been associated with augmented diastolic function [179–181]. The supine position with associated increase in preload, combined with the narrow range of heart rates and lack of inotropic modulation likely contributes to the lack of difference [111, 182].

Under normal conditions, the septum moves towards the LV during systole, contributing to LV ejection [33]. In doing so, it also exerts a 'pull' on the RV blood which, as seen in Fig. 4.11, is accelerated around the septum along a curved path towards the pulmonary valve. Hemodynamic forces therefore demonstrate a physiological role of what could otherwise be seen as a negative action of the septum on RV function.

The finding that RV apical-basal forces in early diastole are smaller than their LV counterpart resonates well with previous findings by Courtois et al. [103], who demonstrated lower early diastolic filling pressure gradient in the RV compared with the LV. The weaker filling gradient was attributed to larger tricuspid valve area compared to mitral valve area and subsequent differences in filling velocity. Another study explained the lower gradient by the slower relaxation rate of the RV compared to the LV [165]. The present three-dimensional method reveals that the magnitude of RV forces is not correctly represented unless the transversal component is taken into account, since it represents a larger force than the apical-basal component (Fig. 4.11). Adding together the apical-basal and main transversal forces (septal-lateral for LV, diaphragm-RVOT for RV) revealed that the magnitude of the early filling force was indeed larger in the LV (see Fig. 9F in Paper III [183]). Since the RV and LV pump equal amounts of blood, this means that the RV achieves its filling by means of smaller hemodynamic forces, possibly compensated by the previously discussed effects of energy conservation and redirection of right atrial blood flow [184].

Chapter 5

Conclusions and future directions

O most lame and impotent conclusion!

William Shakespeare, *Othello*

The following points have been demonstrated and discussed:

- Atrial kinetic energy reflects both the systolic and, to some extent, the diastolic properties of the ventricles. (**Paper I**)
- Rotational blood flow patterns within the atria contribute to energy conservation; in the right heart, this energy is redirected into a helical flow pattern that may help RV filling. (**Paper I**)
- The inflowing atrial blood curls up into a vortex ring whose dimensions are matched to those of the ventricle; the lack of coupling in failing hearts implies that the healthy ventricle adapts to the vortex and not vice versa. (**Paper II**)
- Hemodynamic forces reflect the biventricular performance of the heart and demonstrate significant aberrations in LV dyssynchrony. (**Papers III & IV**)
- Finally, differences between LV and RV hemodynamic forces may be balanced by differences in atrial kinetic energy to effectively utilize the atrioventricular coupling. (**Synthesis of results**)

Every single measure quantified in this thesis seems to beg the question: what happens during exercise? For the aforementioned measures to fully fit into the theory of the 'morphodynamic' heart, i.e. a gradual progression from an optimized resting state to another, equally optimized exercise state, they will have to be investigated during physical stress. This is not a trivial undertaking; as we have seen, echocardiographic measures are unable to

resolve some of the important aspects of the intracardiac flow field [32], and MRI acquisition is sensitive to motion artifacts [42]. Realtime MR imaging is possibly fast enough to address some of the outstanding questions [167], and other methods could also be of use, for example Functional Imaging [93, 95] or numerical simulation methods. In order for computational models to contribute to the investigation of exercise physiology, they must be physically sound (not violate any conservation laws) and be validated against the known physiology at rest, including a correct representation of the fluid motion that results from asymmetric cardiac anatomy and AV plane pumping.

Since this thesis project was initiated, significant work has been done in some of the areas mentioned above. Several studies have found different degrees of disturbed three-dimensional flow patterns during atrial fibrillation [185–187]. Kinetic energy analysis has been extended to encompass elite athletes and several patient groups [132, 143, 151, 188–190]. Right atrial rotational flow has been revisited and its role for energy conservation affirmed [191]. The energy loss of the vortex ring has been investigated after mitral valve surgery [192]. Numerical models incorporating geometry and flow have become increasingly sophisticated and now allow for simulation of inflow patterns, including vortex ring formation [193], the development of thrombus formation under different hemodynamic conditions [194], and dyssynchrony [195, 196]. Flow simulations are making their way into surgical planning [197]. Lower-dimensional models are an attractive option since they are computationally simple and enable online, realtime interaction and modeling of dynamic phenomena [198–200].

The continuation of this work could therefore progress along several lines. It would be interesting to investigate to what extent atrial and ventricular kinetic energy changes during exercise, and how that energy increase contributes to cardiac function. Another possible application is to investigate whether atrial kinetic energy patterns can predict the risk for future thromboembolic events, and thereby provides added value when considering anticoagulation treatment. Furthermore, can the vortex ring dimensions be used as a therapeutic target or measure of cardiac health, e.g. when designing synthetic cardiac valves or considering LV volume reduction surgery? And finally, can hemodynamic forces be used to prospectively single out patients most likely to respond to cardiac resynchronization therapy or to guide the implantation of CRT devices?

Quod scripsi, scripsi.

Pontius Pilatus

References

[1] Shoja M. M., Agutter P. S., Loukas M., Benninger B., Shokouhi G., Namdar H., Ghabili K., Khalili M., and Tubbs R. S. Leonardo da Vinci's studies of the heart. *International Journal of Cardiology*, 167(4):1126–1133, 2013.

[2] Wandt B. Long-axis contraction of the ventricles: a modern approach, but described already by Leonardo da Vinci. *Journal of the American Society of Echocardiography*, 13(7):699–706, 2000.

[3] Carlsson M. *Aspects on Cardiac Pumping*. PhD thesis, Lund University, 2007.

[4] Bellhouse B. J. and Bellhouse F. H. Mechanism of Closure of the Aortic Valve. *Nature*, 217:86–87, 1968.

[5] Coghlan C. and Hoffman J. Leonardo da Vinci's flights of the mind must continue: cardiac architecture and the fundamental relation of form and function revisited. *European Journal of Cardio-thoracic Surgery*, 29:S4–S17, 2006.

[6] Pasipoularides A. Greek underpinnings to his methodology in unraveling de Motu Cordis and what Harvey has to teach us still today. *International Journal of Cardiology*, 168(4):3173–3182, 2013.

[7] Fye B. W. Profiles in Cardiology: Richard Lower. *Clinical Cardiology*, 16:757–758, 1993.

[8] Pettigrew J. On the arrangement of the muscular fibres in the ventricles of the vertebrate heart, with physiological remarks. *Philosophical Transactions of the Royal Society of London*, 154(1864):445–500, 1864.

[9] Sallin E. A. Fiber orientation and ejection fraction in the human left ventricle. *Biophysical journal*, 9(7):954–964, 1969.

[10] Wolf G. Friedrich Miescher - The man who discovered DNA. *Chemical Heritage*, 21(2), 2003.

[11] Shapiro J. *Evolution: A view from the 21st century*. FT Press Science, New Jersey, 1 edition, 2011.

[12] Berger S. L., Kouzarides T., Shiekhattar R., and Shilatifard A. An operational definition of epigenetics. *Genes & Development*, 23:781–783, 2009.

[13] Hove J. R., Köster R. W., Forouhar A. S., Acevedo-Bolton G., Fraser S. E., and Gharib M. Intracardiac fluid forces are an essential epigenetic factor for embryonic cardiogenesis. *Nature*, 421:172–177, 2003.

[14] Allender S., Scarborough P., O'Flaherty M., and Capewell S. Patterns of coronary heart disease mortality over the 20th century in England and Wales: Possible plateaus in the rate of decline. *BMC Public Health*, 8(148):1–12, 2008.

[15] Ponikowski P., Voors A. A., Anker S. D., Bueno H., Cleland J. G. F., Coats A. J. S., Falk V., González-Juanatey J. R., Harjola V.-P., Jankowska E. A., Jessup M., Linde C., Nihoyannopoulos P., Parissis J. T., Pieske B., Riley J. P., Rosano G. M. C., Ruilope L. M., Ruschitzka F., Rutten F. H., and van der Meer P. 2016 ESC Guidelines for the diagnosis and treatment of acute and chronic heart failure. *European Journal of Heart Failure*, 18:891–975, 2016.

[16] Yancy C. W., Jessup M., Bozkurt B., Butler J., Casey D. E., Drazner M. H., Fonarow G. C., Geraci S. A., Horwich T., Januzzi J. L., Johnson M. R., Kasper E. K., Levy W. C., Masoudi F. A., McBride P. E., McMurray J. J. V., Mitchell J. E., Peterson P. N., Riegel B., Sam F., Stevenson L. W., Tang W. H. W., Tsai E. J., and Wilkoff B. L. 2013 ACCF/AHA guideline for the management of heart failure: a report of the American College of Cardiology Foundation/American Heart Association Task Force on practice guidelines. *Circulation*, 128(16):240–327, 2013.

[17] McMurray J. J. V. and Pfeffer M. A. Heart failure. *Lancet*, 365(9474):1877–1889, 2005.

[18] McMurray J. J., Packer M., Desai A. S., Gong J., Lefkowitz M. P., Rizkala A. R., Rouleau J. L., Shi V. C., Solomon S. D., Swedberg K., and Zile M. R. Angiotensin–Neprilysin Inhibition versus Enalapril in Heart Failure. *New England Journal of Medicine*, 371(11):993–1004, 2014.

[19] The SOLVD Investigators. Effect of enalapril on survival in patients with reduced left ventricular ejection fractions and congestive heart failure. *New England Journal of Medicine*, 325(5):293–302, 1991.

[20] The CONSENSUS Trial Study Group. Effects of enalapril on mortality in severe congestive heart failure: Results of the Cooperative North Scandinavian Enalapril Survival Study (CONSENSUS). *New England Journal of Medicine*, 316(23):1429–35, 1987.

[21] Carlsson M., Rosengren A., Ugander M., Ekelund U., Cain P. A., and Arheden H. Center of volume and total heart volume variation in healthy subjects and patients before and after coronary bypass surgery. *Clinical Physiology and Functional Imaging*, 25(4):226–233, 2005.

[22] Noble M. I. M. The contribution of blood momentum to left ventricular ejection in the dog. *Circulation Research*, 23:663–670, 1968.

[23] Courtois M., Kovács S. J., and Ludbrook P. A. Transmitral pressure-flow velocity relation. Importance of regional pressure gradients in the left ventricle during diastole. *Circulation*, 78(3):661–671, 1988.

[24] Katz L. N. The role played by the ventricular relaxation process in filling the ventricle. *American Journal of Physiology*, 95(3):542–553, 1930.

[25] Bowman A. W. and Kovács S. J. Left atrial conduit volume is generated by deviation from the constant-volume state of the left heart: a combined MRI-echocardiographic study. *American Journal of Physiology: Heart and Circulatory Physiology*, 286(6):2416–24, 2004.

[26] Shmuylovich L., Chung C. S., and Kovács S. J. Point: Left ventricular volume during diastasis is the physiological in vivo equilibrium volume and is related to diastolic suction. *Journal of Applied Physiology*, 109(2):606–611, 2010.

[27] Brecher G. A. and Kissen A. T. Ventricular Diastolic Suction at Normal Arterial Pressures. *Circulation Research*, 6(1):100–106, 1958.

[28] Brecher G. A. Critical review of recent work on ventricular diastolic suction. *Circulation Research*, 6(5):554–566, 1958.

[29] Brecher G. A. Experimental evidence of ventricular diastolic suction. *Circulation Research*, 4(5):513–518, 1956.

[30] Zhang W., Chung C. S., Shmuylovich L., and Kovács S. J. Is left ventricular volume during diastasis the real equilibrium volume, and what is its relationship to diastolic suction? *Journal of Applied Physiology*, 105(3):1012–1014, 2008.

[31] Chung C. S., Karamanoglu M., and Kovács S. J. Duration of diastole and its phases as a function of heart rate during supine bicycle exercise. *American Journal of Physiology: Heart and Circulatory Physiology*, 287(5):H2003–H2008, 2004.

[32] Kilner P. J., Henein M. Y., and Gibson D. G. Our tortuous heart in dynamic mode–an echocardiographic study of mitral flow and movement in exercising subjects. *Heart and Vessels*, 12(3):103–110, 1997.

[33] Stephensen S., Steding-Ehrenborg K., Munkhammar P., Heiberg E., Arheden H., and Carlsson M. The relationship between longitudinal, lateral, and septal contribution to stroke volume in patients with pulmonary regurgitation and healthy volunteers. *American Journal of Physiology: Heart and Circulatory Physiology*, 306 (6):895–903, 2014.

[34] Smiseth O. A., Thompson C. R., Lohavanichbutr K., Ling H., Abel J. G., Miyagishima R. T., Lichtenstein S. V., and Bowering J. The pulmonary venous systolic flow pulse - Its origin and relationship to left atrial pressure. *Journal of the American College of Cardiology*, 34(3):802–809, 1999.

[35] Lundbäck S. *Cardiac pumping and function of the ventricular septum*. PhD thesis, 1986.

[36] Carlsson M., Ugander M., Mosen H., Buhre T., and Arheden H. Atrioventricular plane displacement is the major contributor to left ventricular pumping in healthy adults, athletes, and patients with dilated cardiomyopathy. *American Journal of Physiology: Heart and Circulatory Physiology*, 292(3):1452–1459, 2007.

[37] Hamilton W. and Rompf J. Movements of the base of the ventricle and the relative constancy of the cardiac volume. *American Journal of Physiology*, 102:559–565, 1932.

[38] Hoffman E. A. and Ritman E. L. Invariant total heart volume in the intact thorax. *American Journal of Physiology*, 249(4 Pt 2):883–90, 1985.

[39] Bowman A. W. and Kovács S. J. Assessment and consequences of the constant-volume attribute of the four-chambered heart. *American Journal of Physiology: Heart and Circulatory Physiology*, 285(5):2027–2033, 2003.

[40] Carlsson M., Cain P., Holmqvist C., Ståhlberg F., Lundbäck S., and Arheden H. Total heart volume variation throughout the cardiac cycle in humans. *American Journal of Physiology: Heart and Circulatory Physiology*, 287(1):243–250, 2004.

[41] Riordan M. M. and Kovács S. J. Relationship of pulmonary vein flow to left ventricular short-axis epicardial displacement in diastole: model-based prediction with in vivo validation. *American Journal of Physiology: Heart and Circulatory Physiology*, 291(3):1210–5, 2006.

[42] Steding-Ehrenborg K., Jablonowski R., Arvidsson P. M., Carlsson M., Saltin B., and Arheden H. Moderate intensity supine exercise causes decreased cardiac volumes and increased outer volume variations: a cardiovascular magnetic resonance study. *Journal of Cardiovascular Magnetic Resonance*, 15(1):96, 2013.

[43] Waters E. A., Bowman A. W., and Kovács S. J. MRI-determined left ventricular "crescent effect": a consequence of the slight deviation of contents of the pericardial sack from the constant-volume state. *American Journal of Physiology: Heart and Circulatory Physiology*, 288(2):H848–H853, 2005.

[44] Järvinen V. M., Kupari M. M., Hekali P. E., and Poutanen V.-P. Right atrial MR imaging studies of cadaveric atrial casts and comparison with right and left atrial volumes and function in healthy subjects. *Cardiac Radiology*, 191(1):137–142, 1994.

[45] Järvinen V. M., Kupari M. M., Hekali P. E., and Poutanen V.-P. Assessment of left atrial volumes and phasic function using cine magnetic resonance imaging in normal subjects. *The American Journal of Cardiology*, 73(15):1135–8, 1994.

[46] Carlsson M., Ugander M., Heiberg E., and Arheden H. The quantitative relationship between longitudinal and radial function in left, right, and total heart pumping in humans. *American Journal of Physiology: Heart and Circulatory Physiology*, 293 (1):H636–H644, 2007.

[47] Steding-Ehrenborg K., Carlsson M., Stephensen S., and Arheden H. Atrial aspiration from pulmonary and caval veins is caused by ventricular contraction and secures 70% of the total stroke volume independent of resting heart rate and heart size. *Clinical Physiology and Functional Imaging*, 33(3):233–40, 2013.

[48] Huxley A. F. and Niedergerke R. Structural changes in muscle during contraction; interference microscopy of living muscle fibres. *Nature*, 173(4412):971–973, 1954.

[49] Huxley H. and Hanson J. Changes in the cross-striations of muscle during contraction and stretch and their structural interpretation. *Nature*, 173(4412):973–976, 1954.

[50] Maruyama K., Matsubara S., Natori R., Nonomura Y., Kimura S., Ohashi K., Murakami F., Handa S., and Eguchi G. Connectin, an elastic protein of muscle. *Journal of Biochemistry*, 82(2):317–337, 1977.

[51] Wang K., McClure J., and Tu A. Titin: major myofibrillar components of striated muscle. *Proceedings of the National Academy of Sciences*, 76(8):3698–3702, 1979.

[52] Granzier H. L. and Irving T. C. Passive tension in cardiac muscle: contribution of collagen, titin, microtubules, and intermediate filaments. *Biophysical Journal*, 68(3): 1027–1044, 1995.

[53] Lee E.-J., Peng J., Radke M., Gotthardt M., and Granzier H. L. Calcium sensitivity and the Frank-Starling mechanism of the heart are increased in titin N2B region deficient mice. *Journal of Molecular and Cellular Cardiology*, 49(3):449–458, 2010.

[54] Suga H. Total mechanical energy of a ventricle model and cardiac oxygen consumption. *American Journal of Physiology: Heart and Circulatory Physiology*, 236(3): 498–505, 1979.

[55] Suga H. Ventricular Energetics. *Physiological Reviews*, 70(2):247–277, 1990.

[56] Boudoulas H., Geleris P., Lewis R. P., and Rittgers S. E. Linear relationship between electrical systole, mechanical systole, and heart rate. *Chest*, 80(5):613–617, 1981.

[57] Bowman A. W., Frihauf P. A., and Kovács S. J. Time-varying effective mitral valve area: prediction and validation using cardiac MRI and Doppler echocardiography in normal subjects. *American Journal of Physiology: Heart and Circulatory Physiology*, 287(4):H1650–H1657, 2004.

[58] Henriksen E., Sundstedt M., and Hedberg P. Left ventricular end-diastolic geometrical adjustments during exercise in endurance athletes. *Clinical Physiology and Functional Imaging*, 28:76–80, 2008.

[59] Zhou B., Conlee R. K., Jensen R., Fellingham G. W., George J. D., and Fisher A. G. Stroke volume does not plateau during graded exercise in elite male distance runners. *Medicine and Science in Sports and Exercise*, 33(11):1849–1854, 2001.

[60] Biesiadecki B. J., Davis J. P., Ziolo M. T., and Janssen P. M. L. Tri-modal regulation of cardiac muscle relaxation; intracellular calcium decline, thin filament deactivation, and cross-bridge cycling kinetics. *Biophysical Reviews*, 1(6):273–289, 2014.

[61] Chung C. S., Shmuylovich L., and Kovács S. J. What global diastolic function is, what it is not, and how to measure it. *American Journal of Physiology: Heart and Circulatory Physiology*, 309:H1392–H1406, 2015.

[62] Helmes M., Trombitás K., and Granzier H. L. Titin develops restoring force in rat cardiac myocytes. *Circulation Research*, 79(3):619–626, 1996.

[63] Preetha N., Yiming W., Helmes M., Norio F., Siegfried L., and Granzier H. Restoring force development by titin/connectin and assessment of Ig domain unfolding. *Journal of Muscle Research and Cell Motility*, 26(6-8):307–317, 2006.

[64] Courtois M., Kovács S. J., and Ludbrook P. A. Physiological early diastolic intraventricular pressure gradient is lost during acute myocardial ischemia. *Circulation*, 81(5):1688–1696, 1990.

[65] Yoshida T., Ohte N., Narita H., Sakata S., Wakami K., Asada K., Miyabe H., Saeki T., and Kimura G. Lack of inertia force of late systolic aortic flow is a cause of left ventricular isolated diastolic dysfunction in patients with coronary artery disease. *Journal of the American College of Cardiology*, 48(5):983–991, 2006.

[66] Kovács S. J., Barzilai B., and Perez J. E. Evaluation of diastolic function with Doppler echocardiography: the PDF formalism. *American Journal of Physiology: Heart and Circulatory Physiology*, 252(1):H178–H187, 1987.

[67] Ohtani T., Mohammed S. F., Yamamoto K., Dunlay S. M., Weston S. A., Sakata Y., Rodeheffer R. J., Roger V. L., and Redfield M. M. Diastolic stiffness as assessed by diastolic wall strain is associated with adverse remodelling and poor outcomes in heart failure with preserved ejection fraction. *European Heart Journal*, 33(14): 1742–9, 2012.

[68] Zile M. R. Heart failure with preserved ejection fraction: is this diastolic heart failure? *Journal of the American College of Cardiology*, 41(9):1519–1522, 2003.

[69] Smith G. L., Masoudi F. A., Vaccarino V., Radford M. J., and Krumholz H. M. Outcomes in heart failure patients with preserved ejection fraction: Mortality, readmission, and functional decline. *Journal of the American College of Cardiology*, 41 (9):1510–1518, 2003.

[70] Kovács S. J. Diastolic function in heart failure. *Clinical Medicine Insights: Cardiology*, 9:49–55, 2015.

[71] Braunwald E. The war against heart failure: the Lancet lecture. *The Lancet*, 6736 (14):1–13, 2014.

[72] Nagueh S. F., Appleton C. P., Gillebert T. C., Marino P. N., Oh J. K., Smiseth O. A., Waggoner A. D., Flachskampf F. A., Pellikka P. A., and Evangelisa A. Recommendations for the evaluation of left ventricular diastolic function by echocardiography. *European Journal of Echocardiography*, 10(2):165–93, 2009.

[73] Flachskampf F. a., Biering-Sørensen T., Solomon S. D., Duvernoy O., Bjerner T., and Smiseth O. A. Cardiac imaging to evaluate left ventricular diastolic function. *JACC: Cardiovascular Imaging*, 8(9):1071–1093, 2015.

[74] Kilner P. J., Yang G. Z., Wilkes A. J., Mohiaddin R. H., Firmin D. N., and Yacoub M. H. Asymmetric redirection of flow through the heart. *Nature*, 404:759–61, 2000.

[75] Bettex D. A., Prêtre R., and Chassot P.-G. Is our heart a well-designed pump? The heart along animal evolution. *European Heart Journal*, 35:2322–2332, 2014.

[76] Taber L. A., Voronov D. A., and Ramasubramanian A. The role of mechanical forces in the torsional component of cardiac looping. *Annals of the New York Academy of Sciences*, (1188):103–110, 2010.

[77] Sedmera D., Pexieder T., Rychterova V., Hu N., and Clark E. B. Remodeling of chick embryonic ventricular myoarchitecture under experimentally changed loading conditions. *The Anatomical Record*, 254(2):238–52, 1999.

[78] Taber L. A. Mechanical aspects of cardiac development. *Progress in Biophysics and Molecular Biology*, 69(2-3):237–255, 1998.

[79] Icardo J. M. Developmental biology of the vertebrate heart. *The Journal of experimental zoology*, 275(2-3):144–161, 1996.

[80] Fyrenius A., Wigström L., and Ebbers T. Three dimensional flow in the human left atrium. *Heart*, 86(4):448–455, 2001.

[81] Kilner P. J., Yang G.-Z., and Firmin D. N. Morphodynamics of flow through sinuous curvatures of the heart. *Biorheology*, 39(3-4):409–17, 2002.

[82] Prec O., Katz L. N., Sennett L., Rosenman R., Fishman A., and Hwang W. Determination of kinetic energy of the heart in man. *American Journal of Physiology*, 159 (3):483–491, 1949.

[83] Carlsson M., Heiberg E., Töger J., and Arheden H. Quantification of left and right ventricular kinetic energy using four-dimensional intracardiac magnetic resonance imaging flow measurements. *American Journal of Physiology: Heart and Circulatory Physiology*, 302(4):893–900, 2012.

[84] Stefanadis C., Dernellis J., Lambrou S., and Toutouzas P. Left atrial energy in normal subjects, in patients with symptomatic mitral stenosis, and in patients with advanced heart failure. *The American Journal of Cardiology*, 82:1220–3, 1998.

[85] Didden N. Untersuchung laminarer, instabiler Ringwirbel mittels Laser-Doppler-Anemometrie. Technical report, Göttingen, 1977.

[86] Liess C. Experimentelle Untersuchung des Lebenslaufes von Ringwirbeln. Technical report, Göttingen, 1978.

[87] Shadden S. C., Dabiri J. O., and Marsden J. E. Lagrangian analysis of fluid transport in empirical vortex ring flows. *Physics of Fluids*, 18(4):047105, 2006.

[88] Bellhouse B. J. Fluid mechanics of a model mitral valve and left ventricle. *Cardiovascular Research*, 6:199–210, 1972.

[89] Heiberg E., Ebbers T., Wigström L., and Karlsson M. Three-dimensional flow characterization using vector pattern matching. *IEEE Transactions on Visualization and Computer Graphics*, 9(3):313–319, 2003.

[90] Kim W. Y., Walker P. G., Pedersen E. M., Poulsen J. K., Oyre S., Houlind K., and Yoganathan A. Left ventricular blood flow patterns in normal subjects: a quantitative analysis by three-dimensional magnetic resonance velocity mapping. *Journal of the American College of Cardiology*, 26(1):224–38, 1995.

[91] Pedrizzetti G. and Domenichini F. Nature optimizes the swirling flow in the human left ventricle. *Physical Review Letters*, 95(10):108101, 2005.

[92] Charonko J. J., Kumar R., Stewart K., Little W. C., and Vlachos P. P. Vortices formed on the mitral valve tips aid normal left ventricular filling. *Annals of Biomedical Engineering*, 41(5):1049–1061, 2013.

[93] Pasipoularides A., Shu M., Shah A., Womack M. S., and Glower D. D. Diastolic right ventricular filling vortex in normal and volume overload states. *American Journal of Physiology: Heart and Circulatory Physiology*, 284:H1064–H1072, 2003.

[94] Gharib M., Rambod E., and Shariff K. A universal time scale for vortex ring formation. *Journal of Fluid Mechanics*, 360:121–140, 1998.

[95] Pasipoularides A. *Heart's Vortex: Intracardiac Blood Flow Phenomena*. People's Medical Publishing House, Shelton, Connecticut, 2010.

[96] Irisawa H., Wilson M. F., and Rushmer R. F. Left ventricle as a mixing chamber. *Circulation Research*, 8:183–187, 1960.

[97] Töger J., Kanski M., Arvidsson P. M., Carlsson M., Kovács S. J., Borgquist R., Revstedt J., Söderlind G., Arheden H., and Heiberg E. Vortex-ring mixing as a measure of diastolic function of the human heart: Phantom validation and initial observations in healthy volunteers and patients with heart failure. *Journal of Magnetic Resonance Imaging*, 43(6):1386–1397, 2015.

[98] Olcay A. B. and Krueger P. S. Measurement of ambient fluid entrainment during laminar vortex ring formation. *Experiments in Fluids*, 44(2):235–247, 2008.

[99] Töger J., Kanski M., Carlsson M., Kovács S. J., Söderlind G., Arheden H., and Heiberg E. Vortex ring formation in the left ventricle of the heart: analysis by 4D flow MRI and Lagrangian coherent structures. *Annals of Biomedical Engineering*, 40 (12):2652–2662, 2012.

[100] Töger J. *Measurement and analysis of intracardiac blood flow and vortex ring formation*. PhD thesis, 2014.

[101] Töger J., Arvidsson P. M., Kanski M., Steding-Ehrenborg K., Pedrizzetti G., Carlsson M., Arheden H., and Heiberg E. Intracardiac hemodynamic forces using 4D flow: A new reproducible method applied to healthy controls, elite athletes and

heart failure patients. *Journal of Cardiovascular Magnetic Resonance*, 18(Suppl 1): 1–3, 2016.

[102] Gharib M., Rambod E., Kheradvar A., Sahn D. J., and Dabiri J. O. Optimal vortex formation as an index of cardiac health. *Proceedings of the National Academy of Sciences of the United States of America*, 103(16):6305–8, 2006.

[103] Courtois M., Barzilai B., Gutierrez F., and Ludbrook P. A. Characterization of regional diastolic pressure gradients in the right ventricle. *Circulation*, 82(4):1413–1423, 1990.

[104] Ling D., Rankin J. S., Edwards C. H., McHale P. A., and Anderson R. W. Regional diastolic mechanics of the left ventricle in the conscious dog. *The American Journal of Physiology*, 236(12):H323–H330, 1979.

[105] Song S. M. and Leahy R. M. Computation of 3-D velocity fields from 3-D cine CT images of a human heart. *IEEE Transactions on Medical Imaging*, 10(3):295–306, 1991.

[106] Song S. M., Leahy R. M., Boyd D. P., Brundage B. H., and Napel S. Determining cardiac velocity fields and intraventricular pressure distribution from a sequence of ultrafast CT cardiac images. *IEEE Transactions on Medical Imaging*, 13(2):386–397, 1994.

[107] Tyszka J. M., Laidlaw D. H., Asa J. W., and Silverman J. M. Three-dimensional, time-resolved (4D) relative pressure mapping using magnetic resonance imaging. *Journal of Magnetic Resonance Imaging*, 12(2):321–329, 2000.

[108] Yang G. Z., Kilner P. J., Wood N. B., Underwood S. R., and Firmin D. N. Computation of flow pressure fields from magnetic resonance velocity mapping. *Magnetic Resonance in Medicine*, 36(4):520–526, 1996.

[109] Ebbers T., Wigström L., Bolger a. F., Wranne B., and Karlsson M. Noninvasive measurement of time-varying three-dimensional relative pressure fields within the human heart. *Journal of Biomechanical Engineering*, 124(3):288, 2002.

[110] Eriksson J., Bolger A. F., Carlhäll C.-J., and Ebbers T. Spatial heterogeneity of four-dimensional relative pressure fields in the human left ventricle. *Magnetic Resonance in Medicine*, 74:1716–1725, 2015.

[111] Yotti R., Bermejo J., Antoranz J. C., Desco M. M., Cortina C., Rojo-Álvarez J. L., Allué C., Martín L., Moreno M., Serrano J. A., Muñoz R., and García-Fernández M. A. A noninvasive method for assessing impaired diastolic suction in patients with dilated cardiomyopathy. *Circulation*, 112:2921–2929, 2005.

[112] Eriksson J., Bolger A. F., Ebbers T., and Carlhäll C.-J. Assessment of left ventricular hemodynamic forces in healthy subjects and patients with dilated cardiomyopathy using 4D flow MRI. *Physiological Reports*, 4(3):e12685, 2016.

[113] Kalogirou S., Malissovas N., Moro E., Argenton F., Stainier D. Y. R., and Beis D. Intracardiac flow dynamics regulate atrioventricular valve morphogenesis. *Cardiovascular Research*, (104):49–60, 2014.

[114] Pedrizzetti G., Martiniello A. R., Bianchi V., D'Onofrio A., Caso P., and Tonti G. Cardiac fluid dynamics anticipates heart adaptation. *Journal of Biomechanics*, 48(2): 388–391, 2015.

[115] Pedrizzetti G., Martiniello A. R., Bianchi V., D'Onofrio A., Caso P., and Tonti G. Changes in electrical activation modify the orientation of left ventricular flow momentum: novel observations using echocardiographic particle image velocimetry. *European Heart Journal - Cardiovascular Imaging*, 17(2):203–209, 2016.

[116] Abraham W. T., Fisher W. G., Smith A. L., Delurgio D. B., Leon A. R., Loh E., Kocovic D. Z., Packer M., Clavell A. L., Hayes D. L., Ellestad M., and Messenger J. Cardiac resynchronization in chronic heart failure. *New England Journal of Medicine*, 346(24):493–501, 2002.

[117] Moss A. J., Hall J., Cannom D. S., Klein H., Brown M. W., Daubert J. P., Estes III N. A. M., Foster E., Greenberg H., Higgins S. L., Pfeffer M. A., Solomon S. D., Wilber D., and Zareba W. Cardiac-Resynchronization Therapy for the Prevention of Heart-Failure Events. *New England Journal of Medicine*, 361(14):1329–1338, 2009.

[118] Knappe D., Pouleur A.-C., Shah A. M., Cheng S., Uno H., Hall W. J., Bourgoun M., Foster E., Zareba W., Goldenberg I., McNitt S., Pfeffer M. a., Moss A. J., and Solomon S. D. Dyssynchrony, contractile function, and response to cardiac resynchronization therapy. *Circulation Heart failure*, 4(4):433–440, 2011.

[119] Pouleur A.-C., Knappe D., Shah A. M., Uno H., Bourgoun M., Foster E., McNitt S., Hall W. J., Zareba W., Goldenberg I., Moss A. J., Pfeffer M. A., and Solomon S. D. Relationship between improvement in left ventricular dyssynchrony and contractile function and clinical outcome with cardiac resynchronization therapy: the MADIT-CRT trial. *European Heart Journal*, 32(14):1720–1729, 2011.

[120] Hsu J. C., Solomon S. D., Bourgoun M., McNitt S., Goldenberg I., Klein H., Moss A. J., and Foster E. Predictors of super-response to cardiac resynchronization therapy and associated improvement in clinical outcome: The MADIT-CRT (Multicenter Automatic Defibrillator Implantation Trial with Cardiac Resynchronization

Therapy) study. *Journal of the American College of Cardiology*, 59(25):2366–2373, 2012.

[121] Strauss D. G., Selvester R. H., and Wagner G. S. Defining left bundle branch block in the era of cardiac resynchronization therapy. *The American Journal of Cardiology*, 107(6):927–934, 2011.

[122] Solomon S. D., Foster E., Bourgoun M., Shah A., Viloria E., Brown M. W., Hall W. J., Pfeffer M. A., and Moss A. J. Effect of cardiac resynchronization therapy on reverse remodeling and relation to outcome: Multicenter automatic defibrillator implantation trial: Cardiac resynchronization therapy. *Circulation*, 122(10):985–992, 2010.

[123] Chaturvedi P. and Tyagi S. C. Epigenetic mechanisms underlying cardiac degeneration and regeneration. *International Journal of Cardiology*, 173(1):1–11, 2014.

[124] Pasipoularides A. Diastolic filling vortex forces and cardiac adaptations: Probing the epigenetic nexus. *Hellenic Journal of Cardiology*, 53:458–469, 2012.

[125] Rabi I. I., Zacharias J. R., Millman S., and Kusch P. A new method of measuring nuclear magnetic moment. *Physical Review*, 53(February):318, 1938.

[126] Bloch F. Nuclear induction. *Physical Review*, 70(7-8):460–474, 1946.

[127] Purcell E. M., Torrey H. C., and Pound R. V. Resonance absorption by nuclear magnetic moments in a solid. *Physical Review*, 69(1-2):37–38, 1946.

[128] Lauterbur P. C. Image formation by induced local interactions: examples employing nuclear magnetic resonance. *Nature*, 242:190–191, 1973.

[129] Lanzer P., Botvinick E. H., Schiller N. B., Crooks L. E., Arakawa M., Kaufman L., Davis P. L., Herfkens R. J., Lipton M. J., and Higgins C. B. Cardiac imaging using gated magnetic resonance. *Radiology*, 1(150):121–7, 1984.

[130] Ehman R., McNamara M. T., Pallack M., Hricak H., and Higgins C. B. Magnetic resonance imaging with respiratory gating: techniques and advantages. *American Journal of Roentgenology*, 143:1175–1182, 1984.

[131] Sigfridsson A., Kvitting J.-P. E., Knutsson H., and Wigström L. Five-dimensional MRI incorporating simultaneous resolution of cardiac and respiratory phases for volumetric imaging. *Journal of Magnetic Resonance Imaging*, 25(1):113–121, 2007.

[132] Kanski M., Arvidsson P. M., Töger J., Borgquist R., Heiberg E., and Carlsson M. Left ventricular fluid kinetic energy time curves in heart failure from cardiovascular magnetic resonance 4D flow data. *Journal of Cardiovascular Magnetic Resonance*, 2015.

[133] Dyverfeldt P. and Ebbers T. Comparison of respiratory motion suppression techniques for 4D flow MRI. *Magnetic Resonance in Medicine*, (October 2016):1–6, 2017.

[134] Hahn E. L. Detection of sea-water motion by nuclear precession. *Journal of Geophysical Research*, 65(2):776–777, 1960.

[135] Moran P. R. A flow velocity zeugmatographic interlace for NMR imaging in humans. *Magnetic Resonance Imaging*, 1:197–203, 1982.

[136] Nayler G. L., Firmin D. N., and Longmore D. B. Blood flow imaging by cine magnetic resonance, 1986.

[137] Ståhlberg F., Thomsen C., Söndergaard L., and Henriksen O. Pulse sequence design for MR velocity mapping of complex flow: Notes on the necessity of low echo times. *Magnetic Resonance Imaging*, 12(8):1255–1262, 1994.

[138] Pelc N. J., Bernstein M. A., Shimakawa A., and Glover G. H. Encoding strategies for three-direction phase-contrast MR imaging of flow. *Journal of Magnetic Resonance Imaging*, 1(4):405–413, 1991.

[139] Wigström L., Sjöqvist L., and Wranne B. Temporally resolved 3D phase-contrast imaging. *Magnetic Resonance in Medicine*, 36:800–803, 1996.

[140] Carlhäll C. J. and Bolger A. Passing strange: flow in the failing ventricle. *Circulation Heart Failure*, 3(2):326–31, 2010.

[141] Fredriksson A. G., Zajac J., Eriksson J., Dyverfeldt P., Bolger A. F., Ebbers T., and Carlhäll C.-J. 4-D blood flow in the human right ventricle. *American Journal of Physiology: Heart and Circulatory Physiology*, 301(6):2344–50, 2011.

[142] Eriksson J., Carlhäll C. J., Dyverfeldt P., Engvall J., Bolger A. F., and Ebbers T. Semi-automatic quantification of 4D left ventricular blood flow. *Journal of Cardiovascular Magnetic Resonance*, 12:9, 2010.

[143] Svalbring E., Fredriksson A., Eriksson J., Dyverfeldt P., Ebbers T., Bolger A. F., Engvall J., and Carlhäll C. J. Altered diastolic flow patterns and kinetic energy in subtle left ventricular remodeling and dysfunction detected by 4D flow MRI. *PLoS ONE*, 11(8):e0161391, 2016.

[144] François C. J., Srinivasan S., Schiebler M. L., Reeder S. B., Niespodzany E., Landgraf B. R., Wieben O., and Frydrychowicz A. 4D cardiovascular magnetic resonance velocity mapping of alterations of right heart flow patterns and main pulmonary artery hemodynamics in tetralogy of Fallot. *Journal of Cardiovascular Magnetic Resonance*, 14:16, 2012.

[145] Ebbers T., Wigström L., Bolger A. F., Engvall J., and Karlsson M. Estimation of relative cardiovascular pressures using time-resolved three-dimensional phase contrast MRI. *Magnetic Resonance in Medicine*, 45(5):872–879, 2001.

[146] Dyverfeldt P., Sigfridsson A., Kvitting J.-P. E., and Ebbers T. Quantification of intravoxel velocity standard deviation and turbulence intensity by generalizing phase-contrast MRI. *Magnetic Resonance in Medicine*, 56(4):850–858, 2006.

[147] Zajac J., Eriksson J., Dyverfeldt P., Bolger A. F., Ebbers T., and Carlhäll C.-J. Turbulent kinetic energy in normal and myopathic left ventricles. *Journal of Magnetic Resonance Imaging*, 4:1021–1029, 2015.

[148] Steding-Ehrenborg K., Arvidsson P. M., Töger J., Rydberg M., Heiberg E., Carlsson M., and Arheden H. Determinants of kinetic energy of blood flow in the four-chambered heart in athletes and sedentary controls. *American Journal of Physiology: Heart and Circulatory Physiology*, (11):113–122, 2015.

[149] Elbaz M. S. M., Calkoen E. E., Westenberg J. J. M., Lelieveldt B. P. F., Roest A. A. W., and van der Geest R. J. Vortex flow during early and late left ventricular filling in normal subjects: quantitative characterization using retrospectively-gated 4D flow cardiovascular magnetic resonance and three-dimensional vortex core analysis. *Journal of Cardiovascular Magnetic Resonance*, 16(1):78, 2014.

[150] Carlsson M., Töger J., Kanski M., Bloch K. M., Ståhlberg F., Heiberg E., and Arheden H. Quantification and visualization of cardiovascular 4D velocity mapping accelerated with parallel imaging or k-t BLAST: head to head comparison and validation at 1.5 T and 3 T. *Journal of Cardiovascular Magnetic Resonance*, 13:55, 2011.

[151] Steding-Ehrenborg K., Arvidsson P. M., Töger J., Rydberg M., Heiberg E., Carlsson M., and Arheden H. Determinants of kinetic energy of blood flow in the four-chambered heart in athletes and sedentary controls. *American Journal of Physiology: Heart and Circulatory Physiology*, 310:H113–H122, 2016.

[152] Jablonowski R., Nordlund D., Kanski M., Ubachs J., Koul S., Heiberg E., Engblom H., Erlinge D., Arheden H., and Carlsson M. Infarct quantification using 3D inversion recovery and 2D phase sensitive inversion recovery; validation in patients and ex vivo. *BMC Cardiovascular Disorders*, 13(110):1–8, 2013.

[153] Kanski M., Töger J., Steding-Ehrenborg K., Xanthis C., Markenroth Bloch K., Heiberg E., Carlsson M., and Arheden H. Whole-heart four-dimensional flow can be acquired with preserved quality without respiratory gating, facilitating clinical use: a head-to-head comparison. *BMC Medical Imaging*, 15(20):1–13, 2015.

[154] Heiberg E., Sjogren J., Ugander M., Carlsson M., Engblom H., and Arheden H. Design and validation of Segment - freely available software for cardiovascular image analysis. *BMC Medical Imaging*, 10(1):1–13, 2010.

[155] Busch J., Giese D., and Kozerke S. Image-based background phase error correction in 4D flow MRI revisited. *Journal of Magnetic Resonance Imaging*, pages 1–10, 2017.

[156] Trudnowski R. J. and Rico R. C. Specific gravity of blood and plasma at 4 and 37° C. *Clinical Chemistry*, 20(5):615–616, 1974.

[157] Dabiri J. and Gharib M. Fluid entrainment by isolated vortex rings. *Journal of Fluid Mechanics*, 511:311–331, 2004.

[158] Töger J., Bidhult S., Revstedt J., Carlsson M., Arheden H., and Heiberg E. Independent validation of four-dimensional flow MR velocities and vortex ring volume using particle imaging velocimetry and planar laser-induced fluorescence. *Magnetic Resonance in Medicine*, 75(3):1064–1075, 2016.

[159] Farnebäck G., Rydell J., Ebbers T., Andersson M., and Knutsson H. Efficient computation of the inverse gradient on irregular domains. In *Proceedings: 2007 IEEE 11th International Conference on Computer Vision*, 2007.

[160] Ebbers T. and Farnebäck G. Improving computation of cardiovascular relative pressure fields from velocity MRI. *Journal of Magnetic Resonance Imaging*, 30(1):54–61, 2009.

[161] Grant C., Bunnell I. L., and Greene D. G. The reservoir function of the left atrium during ventricular systole: An angiocardiographic study of atrial stroke volume and work. *The American Journal of Medicine*, 37:36–43, 1964.

[162] Sabbah H. N., Anbe D. T., and Stein P. D. Can the human right ventricle create a negative diastolic pressure suggestive of suction? *Catheterization and Cardiovascular Diagnosis*, 1981.

[163] Sabbah H. N. and Stein P. D. Negative diastolic pressure in the intact canine right ventricle. Evidence of diastolic suction. *Circulation Research*, 49(1):108–113, 1981.

[164] Sun Y., Belenkie I., Wang J.-J., and Tyberg J. V. Assessment of right ventricular diastolic suction in dogs with the use of wave intensity analysis. *American Journal of Physiology: Heart and Circulatory Physiology*, 291:H3114–H3121, 2006.

[165] Cortina C., Bermejo J., Yotti R., Desco M. M., Rodríguez-Pérez D., Antoranz J. C., Rojo-Álvarez J. L., Garcia D., García-Fernández M. A., and Fernández-Avilés F. Noninvasive assessment of the right ventricular filling pressure gradient. *Circulation*, 116(9):1015–1023, 2007.

[166] Arvidsson P. M., Carlsson M., Kovács S. J., and Arheden H. Letter to the Editor: Atrio-ventricular plane displacement is not the sole mechanism of atrial and ventricular refill. *American Journal of Physiology: Heart and Circulatory Physiology*, 309: H1094–H1096, 2015.

[167] La Gerche A., Claessen G., Van de Bruaene A., Pattyn N., Van Cleemput J., Gewillig M., Bogaert J., Dymarkowski S., Claus P., and Heidbuchel H. Cardiac MRI: a new gold standard for ventricular volume quantification during high-intensity exercise. *Circulation: Cardiovascular Imaging*, 6(2):329–38, 2013.

[168] Poliner L. R., Dehmer G. J., Lewis S. E., Parkey R. W., Blomqvist C. G., and Willerson J. T. Left ventricular performance in normal subjects: a comparison of the responses to exercise in the upright and supine positions. *Circulation*, 62(3): 528–534, 1980.

[169] Bar-Shlomo B. Z., Druck M. N., Morch J. E., Jablonsky G., Hilton J. D., Feiglin D. H., and McLaughlin P. R. Left ventricular function in trained and untrained healthy subjects. *Circulation*, 65(3):484–488, 1982.

[170] Crawford M. H., White D. H., and Amon K. W. Echocardiographic evaluation of left ventricular size and performance during handgrip and supine and upright bicycle exercise. *Circulation*, 59(6):1188–1196, 1979.

[171] Sundstedt M., Jonason T., Ahrén T., Damm S., Wesslén L., and Henriksen E. Left ventricular volume changes during supine exercise in young endurance athletes. c: 467–472, 2003.

[172] Stein R. A., Michielli D., Fox E. L., and Krasnow N. Continuous ventricular dimensions in man during supine exercise and recovery. An echocardiographic study. *The American Journal of Cardiology*, 41(4):655–660, 1978.

[173] Carlhäll C., Wigström L., Heiberg E., Karlsson M., Bolger A. F., and Nylander E. Contribution of mitral annular excursion and shape dynamics to total left ventricular volume change. *American Journal of Physiology: Heart and Circulatory Physiology*, 287(4):H1836–H1841, 2004.

[174] Carlhäll C., Kindberg K., Wigström L., Daughters G. T., Miller D. C., Karlsson M., and Ingels Jr. N. B. Contribution of mitral annular dynamics to LV diastolic filling with alteration in preload and inotropic state. *American Journal of Physiology: Heart and Circulatory Physiology*, 293(3):1473–9, 2007.

[175] Haack T. and Abdelilah-Seyfried S. The force within: endocardial development, mechanotransduction and signalling during cardiac morphogenesis. *Development*, 143(3):373–386, 2016.

[176] Serraf A., Zoghbi J., Belli E., Lacour-Gayet F., Aznag H., Houyel L., Lambert V., Piot D., and Planché C. Congenital mitral stenosis with or without associated defects: An evolving surgical strategy. *Circulation*, 102(19 Suppl III):III166–III171, 2000.

[177] van Dantzig J. M., Delemarre B. J., Bot H., Koster R. W., and Visser C. A. Doppler left ventricular flow pattern versus conventional predictors of left ventricular thrombus after acute myocardial infarction. *Journal of the American College of Cardiology*, 25(6):1341–1346, 1995.

[178] Steding K. *Exercise physiology and cardiac function*. PhD thesis, Lund University, 2010.

[179] Arbab-Zadeh A., Perhonen M., Howden E., Peshock R. M., Zhang R., Adams-Huet B., Haykowsky M. J., and Levine B. D. Cardiac remodeling in response to 1 year of intensive endurance training. *Circulation*, 130(24):2152–2161, 2014.

[180] Levine B. D., Lane L. D., Buckey J. C., Friedman D. B., and Blomqvist C. G. Left ventricular pressure-volume and Frank-Starling relations in endurance athletes. Implications for orthostatic tolerance and exercise performance. *Circulation*, 84(3): 1016–1023, 1991.

[181] Vinereanu D., Florescu N., Sculthorpe N., Tweddel A. C., Stephens M. R., and Fraser A. G. Left ventricular long-axis diastolic function is augmented in the hearts of endurance-trained compared with strength-trained athletes. *Clinical Science*, 103 (3):249–257, 2002.

[182] González-Alonso J., Mora-Rodríguez R., and Coyle E. F. Supine exercise restores arterial blood pressure and skin blood flow despite dehydration and hyperthermia. *The American Journal of Physiology*, 277(2):H576–H583, 1999.

[183] Arvidsson P. M., Töger J., Carlsson M., Steding-Ehrenborg K., Pedrizzetti G., Heiberg E., and Arheden H. H. Left and right ventricular hemodynamic forces in healthy volunteers and elite athletes assessed with 4D flow magnetic resonance imaging. *American Journal of Physiology: Heart and Circulatory Physiology*, 312: H314–H328, 2016.

[184] Arvidsson P. M., Töger J., Heiberg E., Carlsson M., and Arheden H. Quantification of left and right atrial kinetic energy using four-dimensional intracardiac magnetic resonance imaging flow measurements. *Journal of Applied Physiology*, 114(10):1472–81, 2013.

[185] Fluckiger J. U., Goldberger J. J., Lee D. C., Ng J., Lee R., Goyal A., and Markl M. Left atrial flow velocity distribution and flow coherence using four-dimensional flow

MRI: A pilot study investigating the impact of age and Pre- and Postintervention atrial fibrillation on atrial hemodynamics. *Journal of Magnetic Resonance Imaging*, 38:580–587, 2013.

[186] Lee D. C., Markl M., Ng J., Carr M., Benefield B., Carr J. C., and Goldberger J. J. Three-dimensional left atrial blood flow characteristics in patients with atrial fibrillation assessed by 4D flow CMR. *European Heart Journal - Cardiovascular Imaging*, 17(11):1259–1268, 2015.

[187] Markl M., Schnell S., Wu C., Bollache E., Jarvis K., Barker A., Robinson J., and Rigsby C. Advanced flow MRI: emerging techniques and applications. *Clinical Radiology*, 2016.

[188] Jeong D., Anagnostopoulos P. V., Roldan-Alzate A., Srinivasan S., Schiebler M. L., Wieben O., and Francois C. J. Ventricular kinetic energy may provide a novel noninvasive way to assess ventricular performance in patients with repaired tetralogy of Fallot. *The Journal of Thoracic and Cardiovascular Surgery*, 149(5):1339–1347, 2015.

[189] Sjöberg P., Heiberg E., Wingren P., Ramgren Johansson J., Malm T., Arheden H., Liuba P., and Carlsson M. Decreased diastolic ventricular kinetic energy in young patients with fontan circulation demonstrated by four-dimensional cardiac magnetic resonance imaging. *Pediatric Cardiology*, 38(4):669–680, 2017.

[190] Akiyama K., Maeda S., Matsuyama T., Kainuma A., Ishii M., Naito Y., Kinoshita M., Hamaoka S., Kato H., Nakajima Y., Nakamura N., Itatani K., and Sawa T. Vector flow mapping analysis of left ventricular energetic performance in healthy adult volunteers. *BMC Cardiovascular Disorders*, 17(21):1–10, 2017.

[191] Callaghan F. M., Arnott C., Figtree G. A., Kutty S., Celermajer D. S., and Grieve S. M. Quantifying right atrial filling and emptying: A 4D-flow MRI study. *Journal of Magnetic Resonance Imaging*, 45(4):1046–1054, 2017.

[192] Nakashima K., Itatani K., Kitamura T., Oka N., Horai T., Miyazaki S., Nie M., and Miyaji K. Energy dynamics of the intraventricular vortex after mitral valve surgery. *Heart and Vessels*, doi: 10.10, 2017.

[193] Seo J. H., Vedula V., Abraham T., Lardo A. C., Dawoud F., Luo H., and Mittal R. Effect of the mitral valve on diastolic flow patterns. *Physics of Fluids*, 26(12):121901, 2014.

[194] Seo J. H., Abd T., George R. T., and Mittal R. A coupled chemo-fluidic computational model for thrombogenesis in infarcted left ventricles. *American Journal of Physiology: Heart and Circulatory Physiology*, 310(11):H1567–H1582, 2016.

[195] Panthee N., Okada J.-I., Washio T., Mochizuki Y., Suzuki R., Koyama H., Ono M., Hisada T., and Sugiura S. Tailor-made heart simulation predicts the effect of cardiac resynchronization therapy in a canine model of heart failure. *Medical Image Analysis*, 31:46–62, 2016.

[196] Washio T., Okada J. I., Sugiura S., and Hisada T. Large-scale integrated model is useful for understanding heart mechanisms and developments of medical therapy. In *31st Annual International Conference of the IEEE Engineering in Medicine and Biology Society: Engineering the Future of Biomedicine, EMBC 2009*, pages 2347–2350, 2009.

[197] Haggerty C. M., de Zélicourt D. A., Restrepo M., Rossignac J., Spray T. L., Kanter K. R., Fogel M. A., and Yoganathan A. P. Comparing pre- and post-operative Fontan hemodynamic simulations: implications for the reliability of surgical planning. *Annals of Biomedical Engineering*, 40(12):2639–51, 2012.

[198] Broomé M., Maksuti E., Bjällmark A., Frenckner B., and Janerot-Sjöberg B. Closed-loop real-time simulation model of hemodynamics and oxygen transport in the cardiovascular system. *BioMedical Engineering OnLine*, 12(69):1–20, 2013.

[199] Arts T., Delhaas T., Bovendeerd P., Verbeek X., and Prinzen F. Adaptation to mechanical load determines shape and properties of heart and circulation: the CircAdapt model. *American Journal of Physiology: Heart and Circulatory Physiology*, 288:H1943–H1954, 2005.

[200] Mynard J. P., Davidson M. R., Penny D. J., and Smolich J. J. A simple, versatile valve model for use in lumped parameter and one-dimensional cardiovascular models. *International Journal for Numerical Methods in Biomedical Engineering*, 28:626–641, 2012.

Part II

Research papers

Author contributions

Paper I

I participated in the design of the analysis tools, particularly the time resampling and rotational kinetic energy tools, included study subjects, and participated in data acquisition and interpretation. I also performed data analysis, statistical analysis, and figure preparation, and wrote and revised the manuscript.

Paper II

I participated in study design and analysis methods design, performed data analysis and statistical analysis, interpreted the results, prepared figures, and wrote and revised the manuscript.

Paper III

I participated in study design and data collection, performed data analysis and statistical analysis, interpreted results, prepared figures, and wrote and revised the manuscript.

Paper IV

I participated in study design, performed data analysis and statistical analysis, interpreted results, prepared figures, and wrote the manuscript.

Paper I

Paper II

Paper III

Paper IV